Modeling deposition and physical properties of organic semiconductor thin films

Zur Erlangung des akademischen Grades eines

Doktors der Naturwissenschaften (Dr. rer. nat.)

von der KIT-Fakultät für Physik des
Karlsruher Instituts für Technologie (KIT)
angenommene

Dissertation

von

M. Sc. Carl Friedrich Degitz

Tag der mündlichen Prüfung: 01.07.2022

Referent Prof. Dr. Wolfgang Wenzel
Institut für Nanotechnologie
Karlsruher Institut für Technologie

Korreferent Prof. Dr. Jörg Schmalian
Institut für Theorie der Kondensierten Materie
Karlsruher Institut für Technologie

Abstract

Organic semiconductors are a versatile class of materials. In addition to their use in organic solar cells and organic field-effect transistors, their main application is in organic light-emitting diodes (OLEDs), which are used in modern smartphone displays and high-end televisions. Due to their amorphous structure, many of the already known concepts and models from the field of inorganic semiconductors can not be transferred, motivating the research of new methods, which are specifically aimed at describing organic semiconductors. In particular, a fast, computer-aided prediction of relevant device parameters would be an important success, since the chemical space of possible materials is large and the traditional route via synthesis, deposition and subsequent experimental characterization of new materials is extremely time and cost intensive.

In this work, therefore, two different methods that simulate the process of physical vapor deposition of organic semiconductor materials at the atomistic level are investigated. For this purpose, both pure films and mixtures of different materials known from literature are generated *in silico*. The packing and orientation of the molecules in these film are analyzed and their effect on experimentally accessible parameters is studied. For validation, these results are then compared with data from already published measurements. To conclude the work, an artificial neural network based method for improving the force fields used in the deposition simulation is presented, which is then tested on a realistic material.

Zusammenfassung

Organische Halbleiter sind eine vielseitig einsetzbare Klasse von Materialien. Neben der Verwendung in organischen Solarzellen und organischen Feldeffektransistoren finden sie ihre Hauptverwendung in organischen Leuchtdioden (OLEDs, engl.: organic light-emitting diodes), die in modernen Smartphonedisplays und High-End Fernsehern verbaut sind. Aufgrund ihrer amorphen Struktur können viele bereits bekannte Konzepte und Modelle aus dem Bereich inorganischer Halbleiter nicht übertragen werden, was die Erforschung neuer Methoden speziell zur Beschreibung organischer Halbleiter motiviert. Vor allem eine schnelle, computergestützte Vorhersage von relevanten Geräteparametern wäre ein wichtiger Erfolg, da der chemische Raum möglicher Materialien groß und der traditionelle Weg über Synthese, Deposition und anschließender experimenteller Charakterisierung neuer Materialien äußerst zeit- und kostenintensiv ist.

In dieser Arbeit werden daher zwei unterschiedliche Verfahren, welche den Prozess der physikalischen Gasphasenabscheidung von organischen Halbleitermaterialien auf atomistischer Ebene simulieren, untersucht. Dazu werden sowohl Reinfilme als auch Mischungen verschiedener literaturbekannter Materialien *in silico* erstellt. Die Packung und Orientierung der Moleküle im Film wird analysiert und deren Auswirkung auf experimentell zugängliche Parameter untersucht. Zur Validierung werden diese Ergebnisse anschließend mit publizierten experimentellen Daten verglichen. Zum Abschluss der Arbeit wird weiterhin ein auf künstlichen neuralen Netzen basierendes Verfahren zur Verbesserung der verwendeten Simulationskraftfelder vorgestellt, welches dann an einem realistischen Material getestet wird.

Contents

1 Introduction

1.1 Background

The presentation of the first iPhone in 2007 by Apple Inc. [1] marked a turning point in the mobile phone industry and led to a rapidly growing market of smartphones with touchscreen displays. The trend towards larger screens and higher pixel density in conjunction with thinner phones and thus less room for batteries is increasing the demands on modern display technologies and materials: high energy efficiency, thin layers, bright colors and high contrast.

Organic semiconductors build the basis of organic light emitting diodes (OLEDs) which meet the demands of modern display industry. In 1987, Tang et al. published the first OLED design (see fig. 1.1) [2], building the fundament of technological progress in device design and material selection. Since then, OLED displays have found their way into TVs, smartphones, watches and other wearable devices [3, 4, 5]. Compared with liquid crystal-based displays (LCDs), which were used in all iPhones until 2017 [6], they offer a theoretically perfect contrast ratio and a mechanical flexibility which enables the production of smartphones with a foldable display [7]. This is possible due to the fact that OLED displays consist of thousands of small individually contrallable, self emitting pixels. Each pixel itself is a stack of several thin (in the order of $100\,\mathrm{nm}$) layers of different organic materials between two electrodes. These organic materials are typically referred to as organic semiconductors, which can also be used in other applications such as organic photovoltaics (OPV) [8, 9] or organic field effect transistors (OFET) [10, 11]. The thin films are generally either fabricated by a dry process such as physical vapor deposition (PVD) or by a wet process such as ink-jet printing [12, 13]. As of today the dry process is the industry standard due to the achieved higher device efficiencies and better lifetimes [14]. Understanding the influences of the deposition process on the final film properties is therefore a key ingredient in the developement process of new OLED materials.

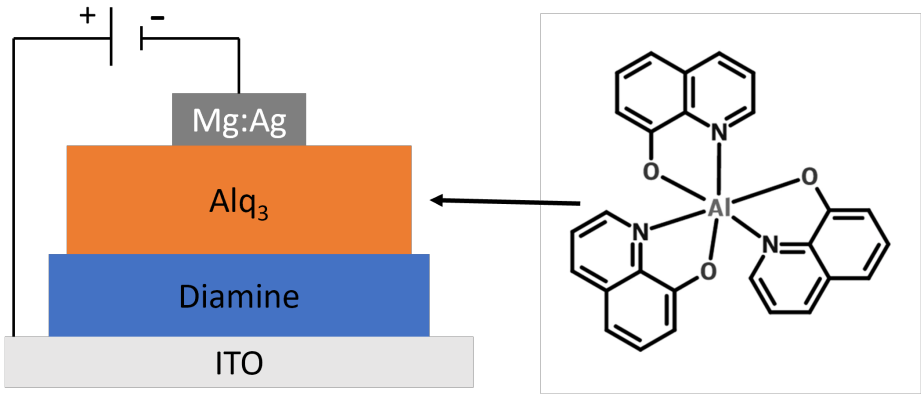

Fig. 1.1.: Schematic view of the OLED as shown in [2]. Indium tin oxide (ITO) serves as the anode, while an alloy of Mg and Ag (10:1 ratio) is used as the cathode. Between both electrodes there are thin layers of an aromatic diamine and the fluorescent material 8-hydroxyquinoline aluminum (Alq3).

Compared with the initially strictly fluorescent OLEDs, vast improvements have been made in increasing the efficiency [15], most notably through the introduction of heavy-metal (e.g. Ir) complexes in the emitter molecule [16]. Due to their enhanced spin-orbit coupling, these emitters allow for radiative transitions from triplet states (phosphorescence), which are forbidden by spin selection rules in normal fluorescent OLED emitters. This leads to a huge improvement in device efficiency since statistically 75% of the activated emitters are in a triplet state, limiting the internal quantum efficiency (IQE) of fluorescent emitters to 25%. However, finding high efficient blue emitters is still an open challenge of high relevance for the design for future OLED stacks [17, 18]. To this end other strategies have been used to overcome the limit for fluorescent emitters, for example by taking advantage of the thermally activated delayed fluorescence (TADF) process [19, 20, 21].

Besides the influences of device fabrication and interplay with other materials in an OLED stack, finding new materials in the vast chemical space of theoretically possible organic semiconductors [22, 23] is time intensive and costly due to the long process of synthesis, deposition and subsequent measurement. To aid and guide this process several computer assisted methods haven been developed during the past decade. These methods cover a wide range of applications: from calculating electronic bulk properties [24, 25] and mobilities [26, 27, 28] starting from ab initio calculations on atomistic structures [29]

towards the simulation of charge transport in whole devices by solving drift diffusion equations [30] parametrized by measurements or empirical data.

1.2 Focus and aim of this thesis

The focus of this thesis lies in the *in silico* generation and subsequent analysis of small structures consisting of realistic organic semiconductor molecules. Two different structure generation methods, both aimed at simulating the physical vapor deposition of small organic molecules, are used to create atomistic structures containing 1000-2000 molecules each. Based on these structures several measurable film properties are calculated and compared with experimental values. The aim of this thesis is to validate and improve existing simulation workflows and develop new ones. This is realized by: (a) implementing and introducing a new deposition approach based on molecular dynamics (MD), (b) comparing it to an existing workflow and (c) presenting a sampling and training procedure for an artificial neural network (ANN) aimed at predicting changes in the total energy and partial charges of a molecule upon a rotation of dihedral fragments, which is subsequently implemented and used in one of the deposition simulation schemes.

1.3 Structure of the thesis

The thesis is divided into six main content chapters. Chapter 2 starts by introducing the theoretical background behind the methods and analysis used throughout this work. The basic concepts of organic semiconductors and how they are used in devices like OLEDs are shown in chapter 3. In chapter 4 all methods used to either simulate the deposition or analyse simulated thin film structures are explained. The methods are then used in chapter 5 to create pure thin film morphologies of four well known organic semiconductors (BCP, BPhen, NPB and CBP). The density of all films is calculated and compared to experiment. Additionally, the anisotropy of the films is analysed by calculating the extra-ordinary and ordinary components of the refractive index. In chapter 6, mixed systems containing an organic host material and different emitter

guest molecules are simulated and the orientation of the emitter molecules is studied by comparing the optical and electrical orientations to experimental data. In chapter 7 an artificial neural network (ANN) forcefield used for the prediction of dihedral energies is extended by a sampling method used to create new training data. The same ANN structure is then also used to predict changes in the partial charges of a molecule. The workflow is tested using NPB as a testcase and the resulting ANNs are implemented and used in one of the deposition approaches.

2 Theoretical Background of Molecular Simulations

This chapter explains the fundamental physical models used for the simulations and calculations performed in this thesis. It starts by introducing the basics of density functional theory in section 2.1, which is used throughout this thesis to study the electronic structure of small organic molecules. Section 2.2 deals with the principles of molecular mechanics which are used in the workflows described in chapter 4 to simulate the deposition process of small organic molecules on an atomistic level. Section 2.3 briefly covers the theory of refraction in dielectric materials.

2.1 Quantum Chemical Calculations

The aim of quantum chemical calculations is to accurately predict the electronic structure of a given set of atoms or molecules, which is fully defined by the time-dependent Schrödinger equation:

$$i\hbar\frac{\partial}{\partial t}\left|\psi(t)\right\rangle = \hat{H}\left|\psi(t)\right\rangle \tag{2.1}$$

where $\hat{H}$ is the Hamilton operator of the specific system and $\psi(t)$ the wave-function describing the systems state. While small systems like the hydrogen atom can be solved analytically, bigger systems become increasingly more difficult to solve. Therefore, several methods and approximations for solving equation 2.1 have been developed. The most prominent one being the Born-Oppenheimer approximation [31], which separates the motion of the atomic nuclei from the electronic motion. This serves as the basis for most electronic structure calculations methods and is introduced in the next section. In the following subsections the principles behind density functional theory (DFT) are explained.

2.1.1 Born-Oppenheimer approximation

The Hamilton operator $\hat{H}$ of a molecular system, consisting of N_C atomic nuclei and N_e electrons, can be written as the sum of the kinetic and Coulomb parts of its constituents:

$$\begin{aligned}
\hat{H} &= \hat{T}_N + \hat{T}_e + \hat{V}_{Ne} + \hat{V}_{ee} + \hat{V}_{NN} \\
\hat{T}_N &= -\frac{\hbar^2}{2}\sum_{j=1}^{N_C}\frac{1}{M_j}\nabla_j \quad \hat{T}_e = -\frac{\hbar^2}{2m_e}\sum_{i=1}^{N_e}\nabla_i \\
\hat{V}_{Ne} &= -\frac{1}{4\pi\epsilon_0}\sum_{j=1}^{N_N}\sum_{i=1}^{N_e}\frac{Z_j e^2}{r_{ij}} \quad \hat{V}_{ee} = \frac{1}{4\pi\epsilon_0}\sum_{j=1}^{N_e}\sum_{i=j}^{N_e}\frac{e^2}{r_{ij}} \\
\hat{V}_{NN} &= \frac{1}{4\pi\epsilon_0}\sum_{j=1}^{N_N}\sum_{i=j}^{N_C}\frac{Z_i Z_j e^2}{R_{ij}}
\end{aligned} \tag{2.2}$$

Solving this equation gets increasingly challenging with growing system size and is effectively impossible for most molecular systems of scientific interest. One way of simplifying equation (2.2) is to separate the electron motion from the nuclear motion. For the electronic part of the equation the kinetic operator of the nuclei is $T_N \approx 0$, which is a reasonable approximation due to the much larger mass of the nuclei. This leaves an electronic equation which only parametrically depends on the nuclear coordinates:

$$\hat{H}^e\psi_i = (\hat{T}_e + \hat{V}_{Ne} + \hat{V}_{ee} + \hat{V}_{NN})\psi_i \tag{2.3}$$

2.1.2 Density functional theory (DFT)

With the growth of available computational power of the last decades, several computational approaches have been developed to solve (2.3), one of the most widely used ones being density functional theory (DFT). DFT, as the name suggests, calculates the electronic structure of a given system by estimating the correct electron density $\rho(\mathbf{r})$ rather than the molecular orbitals ψ_i. The

density itself can be calculated from the molecular orbitals together with their occupation number n_i (which is either 0, 1 or 2):

$$\rho(\mathbf{r}) = \sum_i n_i \left|\psi_i(\mathbf{r})\right|^2 \tag{2.4}$$

The basis of this approach has its origin in the Hohenberg-Kohn theorems (HK) published by Walter Kohn and Pierre Hohenberg in 1964 [32]. The first theorem states that the external electric potential of the nuclei in equation (2.3) uniquely defines the ground state density of the system and *vice versa*. The second theorem states that ground state energy for a given system can be written as a functional of the density which has the exact ground state energy as a lower bound:

$$E\left[\rho\right] \geq E^0 \tag{2.5}$$

In theory, this enables the calculation of the correct ground state energy from the electronic density in a variational approach. In 1965 the Kohn-Sham (KS) formalism was introduced to tackle this problem [33]. In this formalism the real system is replaced by an auxiliary KS system of non-interacting particles in an effective potential V_{eff}. The effective potential is chosen in such a way, that the density of ground state density of the KS system matches the one in the real system. The Schrödinger equation for the auxiliary system (also called Kohn-Sham-equation) is

$$\left[-\frac{\hbar^2}{2m_e}\nabla^2 + V_{\text{eff}}\right]\varphi_i\left(\mathbf{r}\right) = \epsilon_i\varphi_i\left(\mathbf{r}\right) \tag{2.6}$$

with the KS orbitals φ_i. The effective potential can be divided into three contributions:

$$V_{\text{eff}} = V_{\text{ext}}\left(\mathbf{r}\right) + \int \frac{\rho\left(\mathbf{r}\right)}{\left|\mathbf{r}-\mathbf{r}'\right|} + V_{\text{XC}}\left[\rho\left(\mathbf{r}\right)\right] \tag{2.7}$$

The first contribution is the external potential given by the electrostatic potential of the atomic nuclei (same as $\hat{V}_{Ne}$ in equation (2.3)). The second part is the Hartree part, which describes the coulomb repulsion between the electrons. The third part comprises the missing correlation and exchange contributions and is unknown. Therefore, some assumption for $V_{\text{XC}}\left[\rho\left(\mathbf{r}\right)\right]$ has to be made in order to solve a specific problem. (see 2.1.3).

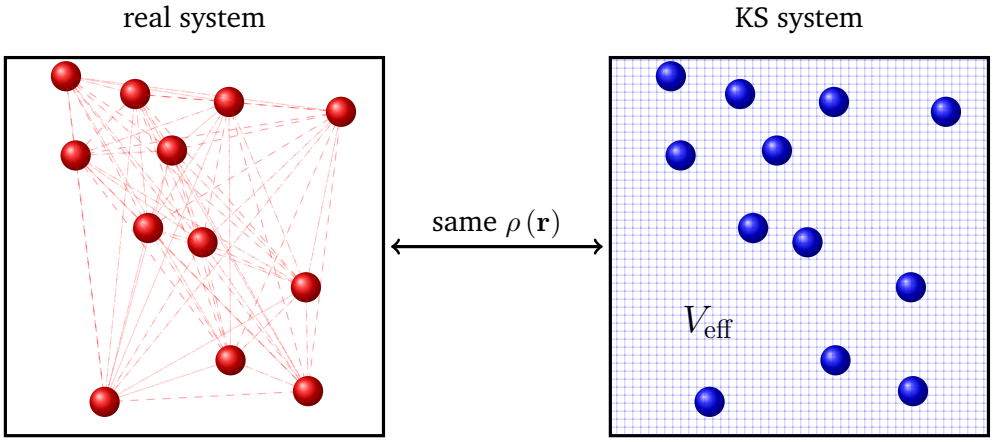

(a) Auxiliary KS system

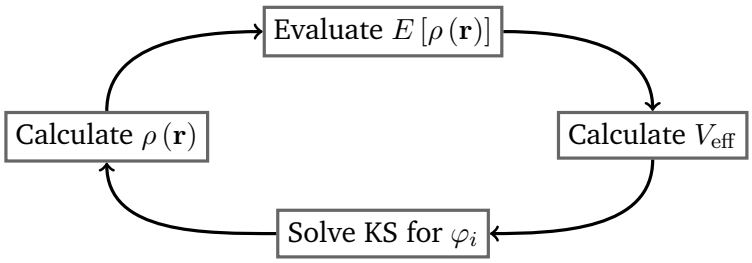

(b) KS workflow

Fig. 2.1.: (a) The real system, consisting of N interacting particles, is substituted by an auxiliary system with N non-interacting particles in an effective potential V_{eff}. The auxiliary system is defined in such a way that the particle density matches the one in the real system.
(b) The KS equations are solved iteratively, starting from a first guess of $\rho(\mathbf{r})$. The procedure stops when the total ground state energy $E[\rho(\mathbf{r})]$ converges.

Since the density depends on the effective potential and the effective potential itself depends on the density. After guessing a starting value for $\rho(\mathbf{r})$, an iterative procedure is used to solve the KS equation (see 2.1).

2.1.3 Exchange correlation functional

The exchange correlation potential $V_{\mathrm{XC}}[\rho(\mathbf{r})]$ is an unknown contribution in the Kohn-Sham formalism and subject of many studies. It is closely related to the exchange correlation energy $E_{\mathrm{XC}}[\rho(\mathbf{r})]$, often referred to as the exchange correlation functional via:

$$V_{\mathrm{XC}}[\rho(\mathbf{r})] = \frac{\delta E_{\mathrm{XC}}[\rho(\mathbf{r})]}{\delta \rho(\mathbf{r})} \tag{2.8}$$

Since the formulation of the Kohn-Sham equations several approaches have been published, often tailored to the specific problem at hand. In the following the local density approximations (LDA), the generalized gradient approximations (GGA) aswell as the hybrid functional B3LYP, which was used throughout this work, are quickly introduced.

In the local density approximation the exchange correlation energy can be written as:

$$E_{\mathrm{XC}}^{\mathrm{LDA}}[\rho(\mathbf{r})] = \int \rho(\mathbf{r}) \left(\epsilon_x(\rho(\mathbf{r})) + \epsilon_c(\rho(\mathbf{r}))\right) \mathrm{d}\mathbf{r} \tag{2.9}$$

where ϵ_x and ϵ_c are the per particle exchange and correlation parts of a homogeneous electron gas, which only depend on the value of the electron density at each point in space. While the exchange part of this is analytically know, only approximations exist for the correlation part resulting in several different types of LDA functionals available. The next more general form also includes a dependency on the gradient of the density at each point in space and is called the generalized gradient approximation (GGA):

$$E_{\mathrm{XC}}^{\mathrm{GGA}}[\rho(\mathbf{r})] = \int \rho(\mathbf{r}) \left(\epsilon_x(\rho(\mathbf{r}), \nabla\rho(\mathbf{r})) + \epsilon_c(\rho(\mathbf{r}), \nabla\rho(\mathbf{r}))\right) \mathrm{d}\mathbf{r} \tag{2.10}$$

While LDA and GGA functionals achieve reasonable results for semiconducting [34] or transition metal crystal structures [35], they are worse for the

prediction of the electronic structure of small organic molecules. Therefore, in this work the *Becke 3-parameter Lee–Yang–Parr* (B3LYP) [36] functional was used which achieves good results for a large set of organic molecules [37]. The B3LYP is a hybrid functional, which means that it mixes parts of the exact exchange energy from a Hartree-Fock calculation with other exchange correlation functionals. The exact mixing parameters are more or less random and often fitted empirically. The B3LYP functional specifically is defined as [38]:

$$E_{\mathrm{XC}}^{\mathrm{B3lYP}} = 0.8E_{\mathrm{X}}^{\mathrm{LSDA}} + 0.2E_{\mathrm{X}}^{\mathrm{HF}} + 0.72\Delta E_{\mathrm{X}}^{\mathrm{B88}} + 0.81E_{\mathrm{C}}^{\mathrm{LYP}} + 0.19E_{\mathrm{C}}^{\mathrm{VWN}} \quad (2.11)$$

where $E_{\mathrm{X}}^{\mathrm{LSDA}}$ is the known exchange part of the local spin density approximation [39], $E_{\mathrm{X}}^{\mathrm{HF}}$ is the exact exchange from a HF calculation, $\Delta E_{\mathrm{X}}^{\mathrm{B88}}$ is the gradient correction for the exchange energy by Becke [40], $E_{\mathrm{C}}^{\mathrm{LYP}}$ is the correlation functional of Lee, Yang and Parr [41] and $E_{\mathrm{C}}^{\mathrm{VWN}}$ is the local correlation functional of Vosko, Wilk and Nusair [42].

2.1.4 Excited state calculations

While technically being a method for explicitly ground state calculations, DFT can also be used to compute excited state and response properties with the ansatz of time-dependent-density-functional-theory (TDDFT). At the core of TDDFT is the *Runge-Gross* theorem [43] which states (similarly to the KS theorem) that the time dependent external potential $V_{\mathrm{ext}}(\mathbf{r}, t)$ is uniquely defined by the time dependent density $\rho(\mathbf{r}, t)$. Together with the *van Leeuwen* theorem [44], which ensures that $\rho(\mathbf{r}, t)$ can be reproduced by a system of non-interacting particles, a time-dependent KS approach can be formulated.

Suppose the system of interest is in its ground-state with a time independent external potential and at $t = t_0$ a time-dependent external potential is introduced:

$$V_{\mathrm{ext}}(\mathbf{r}, t) = V_{\mathrm{ext}}^{0}(\mathbf{r}) + V_{\mathrm{ext}}^{1}(\mathbf{r}, t)\,\Theta(t - t_0) \quad (2.12)$$

with the Heaviside step function Θ. For $t < t_0$ the system can be solved using the standard KS approach presented in section 2.1.2. Starting at $t = t_0$ the system is described by the time-dependent KS system:

$$\left[-\frac{\hbar^2}{2m_e}\nabla^2 + V_{\text{eff}}\left(\mathbf{r},t\right)\right]\varphi_i\left(\mathbf{r},t\right) = i\frac{\partial}{\partial t}\varphi_i\left(\mathbf{r},t\right) \tag{2.13}$$

The effective time dependent potential can again be divided into three contributions:

$$V_{\text{eff}}\left(\mathbf{r},t\right) = V_{\text{ext}}\left(\mathbf{r},t\right) + \int \frac{\rho\left(\mathbf{r},t\right)}{|\mathbf{r}-\mathbf{r}'|} + V_{\text{XC}}\left[\rho\left(\mathbf{r},t\right)\right] \tag{2.14}$$

Where the time-dependent density can be calculated from the time-dependent KS orbitals via:

$$\rho(\mathbf{r},t) = \sum_i n_i \left|\varphi_i(\mathbf{r})\right|^2 \tag{2.15}$$

The solution of these set of equation boils down to the solution of the initial state for $t < t_0$ using the standard KS approach and a subsequent time propagation of the KS orbitals. Again the problem is shifted to the time-dependent exchange correlation functional, for which approximations have to be made.

Many problems of interest for molecular systems, like the calculation of excited state energies and polarizabilities, can be described by a small external potential V^1_{ext} in eq. (2.12). In this case the desired properties can be calculated with a pertubative ansatz which is generally referred to as linear-response theory or linear response TDDFT. A further in detail description of this can be found in [45].

2.1.5 Transition dipole moment

An important property for discussing emission and excitation inside a molecule is the transition dipole moment $\vec{M}_{if}$ between an initial electronic state Ψ_i and a final electronic state Ψ_f of the molecule. It is defined as:

$$\vec{M}_{if} = \langle\Psi_f|\vec{\mu}|\Psi_i\rangle = \int \Psi_f^*\left(\mathbf{r}\right)\vec{\mu}\Psi_i\left(\mathbf{r}\right)\mathrm{d}\mathbf{r} \tag{2.16}$$

with the electric dipole moment $\vec{\mu}$ of the molecule:

$$\vec{\mu} = -e\int \mathbf{r}\rho\left(\mathbf{r}\right)\mathrm{d}\mathbf{r} + e\sum Z_i\mathbf{R}_i \tag{2.17}$$

The connection of this expectation value to light absorption and emission processes was first made by Dirac in 1927 [46]. For a given transition the squared absolute value $\left|\vec{M}_{if}\right|^2$ is directly proportional to the transition probability and the direction of the vector is parallel to the polarization of the light. [47]

2.2 Molecular mechanics

Modeling large molecular systems like polymers or a collection of many individual smaller molecules, quickly outgrows the capabilities of ab initio quantum chemical calculations due to the cubic scaling of the calculation time with respect to the number of basis functions. Even with the strong increase of low-cost computational power combined with parallelized ab initio algorithms, the study of systems with more than $10^5 - 10^6$ atoms seems out of reach for the foreseeable future. For example Seritan et. al. recently reported a total computation time of 10^3 to 10^4 s per energy and gradient evaluation for a system containing less than 1000 atoms on modern GPU architectures [48]. Molecular mechanics approaches circumvent this dilemma by using a classical forcefield in which the atomic nuclei interact, entirely neglecting the individual electronic structure, which often is not the focus of interest anyway. The used molecular mechanical forcefield is typically split into bonded and non-bonded parts, which themselves have different bonded and non-bonded terms. The forcefield is usually parameterized either empirically with the aid of experimental data or by the fitting of specific parameters to ab initio calculations.

In this section I will introduce two different approaches of molecular mechanics, which where used for the structure simulations in this thesis. At first, I will explain the concepts behind molecular dynamics, where the particle trajectories are simulated by direct time-integration of the underlying molecular mechanical forcefield. After that, I will describe the basics behind Monte Carlo based algorithms.

2.2.1 Molecular Dynamics

As mentioned above molecular dynamics (MD) aims to predict the microscopic dynamics of a given molecular system, by direct time integration of the underlying forcefield. There are several integration schemes available, with the Verlet algorithm [49] being the most prominent one among them. A modified form of the Verlet algorithm, published by Swope et. al. in 1982 [50], was used for the molecular dynamic simulations during this work. In this form, the positions $\mathbf{r}_k(t)$ and velocities $\mathbf{v}_k(t)$ of the k-th particle are evaluated as follows:

$$\mathbf{r}_k(t+\Delta t) = \mathbf{r}_k(t) + \mathbf{v}_k(t)\Delta t + \frac{1}{2}\mathbf{a}_k(t)\Delta t^2 \tag{2.18}$$

$$\mathbf{v}_k(t+\Delta t) = \mathbf{v}_k(t) + \frac{\mathbf{a}_k(t+\Delta t) + \mathbf{a}_k(t)}{2}\Delta t \tag{2.19}$$

Here Δt is the timestep used for the simulation and is limited by the highest vibrational frequency of the system. Choosing the right timestep is critical for the simulation: While a too big timestep often leads to nonphysical results or even crashs of the simulation, a too small timestep increases the total computation time drastically, without giving any relevant additional information. For the small organic molecules studied during this work, the fastest vibration is the bond stretching along bonds between hydrogen and another atom, resulting in a timestep of typically 1 fs. The acceleration $\mathbf{a}_k(t)$ links the trajectory to the molecular mechanical forcefield V through Newtons second law:

$$\mathbf{a}_k(t) = \frac{\mathbf{F}_k(t)}{m_k} = -\frac{\nabla_k V(t)}{m_k} \tag{2.20}$$

with the mass m_k of the k-th particle and the force $\mathbf{F}_k(t)$ acting on the k-th particle. The analytic form of V is usually a sum of different bonded and non-bonded terms, which I will describe in the following paragraphs. I'll particularly focus on the analytic form used in the GROMOS 54A7 [51] and OPLS [52] forcefields, which where used for the all-atom simulations during this work.

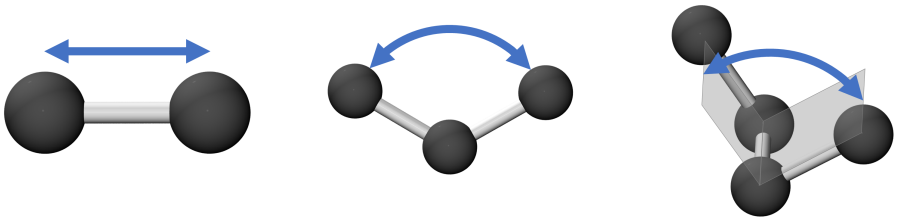

(a) Bond (b) Angle (c) Dihedral

Fig. 2.2.: The three different bonded interaction types in a standard MD forcefield: (a) bondlength variation between two next neighbor atoms, (b) bondangle variation between two neighboring bonds and (c) dihedral angle rotations.

Bonded interactions

The bonded interactions are derived by replacing all covalent bonds by a spring with a specific spring constant. The potential energy of all atom pairs directly connected by a covalent bond is therefore given by a harmonic potential around their equilibrium separation r_0:

$$E_B = \sum_{\text{bonds}} k_B \cdot (r - r_0)^2 \tag{2.21}$$

These type of next-neighbor interactions are also called 1-2 interactions. The interaction with one additional neighbor are called 1-3 interactions and are covered by the angle term:

$$E_A = \sum_{\text{angles}} k_A \cdot (\theta - \theta_0)^2 \tag{2.22}$$

The angle θ is defined as the angle between the vector connecting atom 1 to atom 2 and the vector between atom 2 and atom 3. The last order of bonded interactions are the dihedral interactions, involving 4 different atoms directly connected by covalent bonds. In this term the analytic forms used in the GROMOS and OPLS forcefield differ:

$$E_{DH,\text{GROMOS}} = \sum_{\text{dihedrals}} K\,(1 + d \cdot \cos(n\phi)) \tag{2.23}$$

$$E_{DH,\text{OPLS}} = \sum_{\text{dihedrals}} \sum_{i=1}^{4} \frac{1}{2} K_i \left(1 + (-1)^{i-1} \cos(i\phi)\right) \tag{2.24}$$

where d is either -1 or 1 and $n \in \mathbb{N}_0$. Here ϕ is defined as the angle between the plane normal vectors of the planes depicted in fig. 2.2 (c).

Non-bonded interactions

The first part of the non-boned interactions is a Lennard-Jones (LJ) potential approximating the Pauli repulsion and van der Waals attraction between two different atoms i and j:

$$E_{LJ,ij} = 4\epsilon_{ij}\left[\left(\frac{\sigma_{ij}}{r_{ij}}\right)^{12} - \left(\frac{\sigma_{ij}}{r_{ij}}\right)^{6}\right] \tag{2.25}$$

The LJ Parameters ϵ_{ij} and σ_{ij} are calculated by a geometric mixing of the atom specific parameters:

$$\epsilon_{ij} = \sqrt{\epsilon_i \epsilon_j} \tag{2.26}$$

$$\sigma_{ij} = \sqrt{\sigma_i \sigma_j} \tag{2.27}$$

To reduce the computational effort, all interactions with a separation larger than a specific radius are typically cut off. In this work this cutoff radius was $1.4\,\mathrm{nm}$. The second part of the non-bonded interactions covers the electrostatic interaction between atoms. To this end a partial charge q_i is fitted for every atom. These are either predefined values depending on the element and the way it is bonded in the molecule or fit individually for a given molecule to quantum chemical calculations. The potential energy for particle i is then given via the sum of coulomb interactions with all other particles:

$$E_{C,i} = \sum_{j \neq i} \frac{q_i q_j}{4\pi\epsilon_0 r_{ij}} \tag{2.28}$$

Since the electrostatic interaction falls of with $1/r$, long range effects are completely neglected by simply cutting the interaction at some radius, which is especially important for (partially) periodic systems like the ones discussed in this work. Most periodic simulations therefore approximate the real electrostatic potential with some form of the Ewald summation technique. This technique was initially published by Paul Peter Ewald to calculate the interaction energies in ionic crystal structures [53]. The basic idea behind the Ewald

summation is to split the system in a short range part, where the coulomb interactions are computed explicitly, and a long range part, which is usually solved in the k-space. Since the initial publication in 1921 several different techniques have been published aiming to calculate these k-space contributions [54]. In this work the Particle–Particle–Particle–Mesh (PPPM) algorithm initially developed by Hockney and Eastwood [55] was used. In this algorithm, the charges are mapped onto a mesh grid for which the Poisson equation is solved numerically in reciprocal space. The resulting potential is then transformed back to real space with a Fast-Fourier-transformation. Compared to the initial Ewald summation which scales between $\mathcal{O}(N^2)$ and $\mathcal{O}(N^{\frac{3}{2}})$ [56] this algorithm offers a scaling of $\mathcal{O}(N \log N)$ [57].

Statistical ensembles

In general, a real macroscopic system can be described by a statistical ensemble of all possible individual microstates. Suppose the observable of interest $\mathcal{A}$ is measured T times, then the time-average of this observable is given by:

$$\mathcal{A}_T = \frac{1}{T} \sum_{t=1}^{T} \mathcal{A}(t) \tag{2.29}$$

where $\mathcal{A}(t)$ is the value of the t-th measurement. Increasing the number of measurements T while simultaneously decreasing the interval Δt between each measurements leads to the integral form:

$$\overline{\mathcal{A}(t)} = \frac{1}{T\Delta t} \sum_{t=1}^{T} \mathcal{A}(t)\Delta t = \frac{1}{t} \int_{t_0}^{t_0+t} \mathcal{A}(t')dt' \tag{2.30}$$

with the total measurement interval $t = T\Delta t$. Setting $t_0 = 0$ and looking at the limit for a infinitely long measurement interval t, one reaches the Ergodic hypothesis:

$$\lim_{t\to\infty} \frac{1}{t} \int_0^t \mathcal{A}(t')dt' \stackrel{!}{=} \sum_i p_i A_i = \langle A \rangle \tag{2.31}$$

where $\langle A \rangle$ is the ensemble average of the observable and p_i is the probability of microstate i. This hypothesis states that during a (theoretically) infinitely long time period, the system will reach every possible microstate, which results in the time average of $\mathcal{A}$ being the same as the ensemble average. The prob-

ability of the microstates is directly linked to the underlying thermodynamic ensemble. Choosing the right thermodynamic ensemble depends on the ambient conditions of the individual experiment. A commonly chosen ensemble is the canonical ensemble. In this ensemble the number of particles N, the volume V and the temperature T are kept fixed. Therefore, it is also referred to as the NVT-ensemble. Another commonly realized ensemble is the isothermal–isobaric ensemble or NPT-ensemble, in which instead of the volume the pressure p is kept constant. During a molecular dynamics simulation of a given system in a specific ensemble, the same properties have to be kept constant. In the case of NVT or NPT simulations, this is done by a thermostat or barostat, which adjusts the simulation accordingly. In this work all simulations were performed in the NVT ensemble with the Nosé-Hoover thermostat [58] for simulations at a constant temperature and with the Berendsen thermostat [59] for simulated cooling or heating processes. [60]

2.2.2 Monte Carlo

The right side of eq. (2.31) can also be written in integral form:

$$\langle A \rangle = \iint \rho\left(\mathbf{r}, \mathbf{p}\right) A\left(\mathbf{r}, \mathbf{p}\right) d^{3N}x \; d^{3N}p \tag{2.32}$$

Here $\rho\left(\mathbf{r}, \mathbf{p}\right)$ represents the probability of the system being in the phase space volume $d^{3N}x \; d^{3N}p$, with N the number of particles in the system and $\mathbf{r}$, $\mathbf{p}$ the positions and momenta of all particles respectively. For a system obeying the conditions of a NVT ensemble this probability follows a Boltzmann distribution:

$$\rho\left(\mathbf{r}, \mathbf{p}\right) = \frac{1}{Z} \exp\left(-\frac{E\left(\mathbf{r}, \mathbf{p}\right)}{k_{(B)}T}\right) \tag{2.33}$$

with the canonical partition function:

$$Z = \iint \exp\left(-\frac{E\left(\mathbf{r}, \mathbf{p}\right)}{k_{(B)}T}\right) d^{3N}x \; d^{3N}p \tag{2.34}$$

This means that instead of generating a long trajectory and calculating the time average in eq. (2.30) for some property with a molecular dynamics approach, it is also possible for an ergodic system to sample the phase space and calculate the integral of eq. (2.32). Solving this integral typically has to be done with

a Monte Carlo approach due to its high dimensionality, effectively reducing it to a sum over k random states. A completely random choice of states is extremely inefficient due to the size of the phase space. Therefore, new states a generated in a guided way depending on their contribution to the final sum. This type of sampling is also called importance sampling.

One method of importance sampling often used in a molecular mechanical problem is the Metropolis-Hastings algorithm [61, 62]. In this algorithm, new sampling points of the system a generated along a Markov chain. Inside the Markov chain, the transition to a new state $(\mathbf{r}_n, \mathbf{p}_n)$ only depends on the step immediately before it $(\mathbf{r}_{n-1}, \mathbf{p}_{n-1})$. The transition probability $W\left((\mathbf{r}_i, \mathbf{p}_i) \rightarrow (\mathbf{r}_j, \mathbf{p}_j)\right)$ is chosen in such a way, that for an infinitely long Markov chain the distribution of states follows the Boltzmann distribution of eq. (2.33). Also since the system is assumed to be in thermal equilibrium, obeying the detailed balance criterion:

$$W\left((\mathbf{r}_i, \mathbf{p}_i) \rightarrow (\mathbf{r}_j, \mathbf{p}_j)\right) \rho\left(\mathbf{r}_i, \mathbf{p}_i\right) = W\left((\mathbf{r}_j, \mathbf{p}_j) \rightarrow (\mathbf{r}_i, \mathbf{p}_i)\right) \rho\left(\mathbf{r}_j, \mathbf{p}_j\right) \tag{2.35}$$

Together with eq. (2.33) this leads to the Metropolis acceptance criterion [61]:

$$W\left((\mathbf{r}_i, \mathbf{p}_i) \rightarrow (\mathbf{r}_j, \mathbf{p}_j)\right) = \begin{cases} \exp\left(-\frac{\Delta E}{k_{(B)} T}\right), \Delta E > 0 \\ 1 \qquad\qquad\quad , \Delta E < 0 \end{cases} \tag{2.36}$$

where $\Delta E = E_j - E_i$ with the initial state i and the final state j. This means that a state of lower energy is always accepted. For a state with a higher energy, the new state is accepted by drawing a random number between 0 and 1 and comparing it to the Boltzmann factor of ΔE. If the random number is smaller, the new state is accepted. If it is higher, the new state is rejected. This method is used in the Monte Carlo deposition algorithm originally developed by Neumann *et al.* [29] and furthermore described in section 4.1.2 of this work.

2.3 Refractive Index

Light can be described by an electromagnetic wave consisting of an oscillating electric and magnetic field traveling through space. The electric field can,

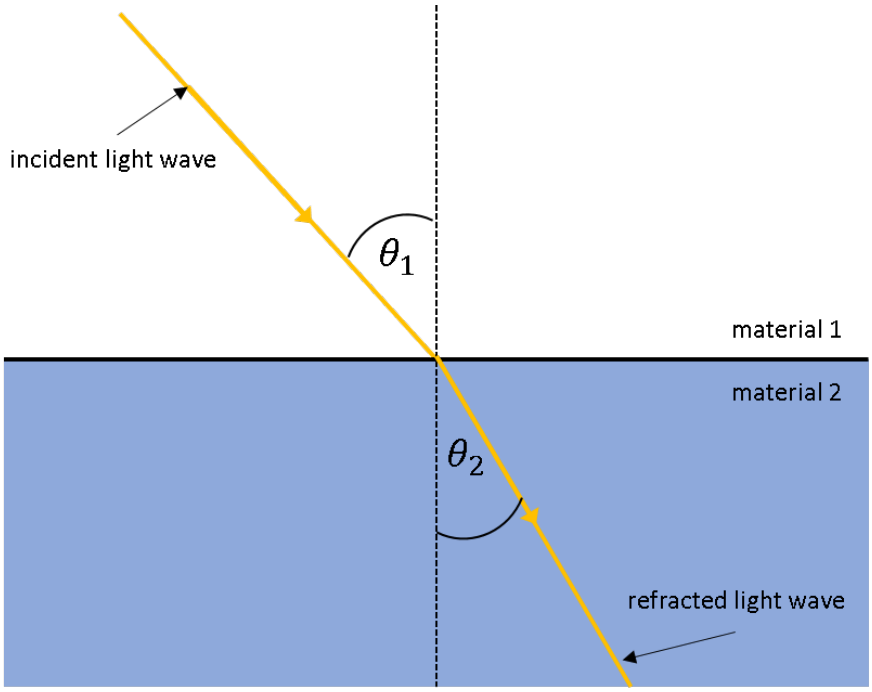

Fig. 2.3.: Refraction of a light wave going from material 1 with a lower refractive index to material 2 with a higher refractive index with the angle of incidence θ_1 and the angle of refraction θ_2.

in the most general case, be described by a simple plane wave with angular frequency ω and wave vector $\mathbf{k}$:

$$\mathbf{E}(\mathbf{r}, t) \sim \exp(-i(\mathbf{k} \cdot \mathbf{r} + \omega t)) \tag{2.37}$$

When traveling through a medium, the wave length λ is influenced by the refractive index of the material:

$$\lambda = \frac{\lambda_0}{n} \tag{2.38}$$

where λ_0 is the wavelength in vacuum. The wave vector is directly connected to the wave length via:

$$k = |\mathbf{k}| = \frac{2\pi}{\lambda} = \frac{2\pi n}{\lambda_0} \tag{2.39}$$

This leads to the phenomenon of refraction at the interface of two materials with different refractive indices (see fig. 2.3). The angle of incidence θ_1 and the angle of refraction θ_2 are connected to the refractive indices n_1 and n_2 by Snell's law:

$$\frac{\sin\theta_2}{\sin\theta_1} = \frac{n_1}{n_2} \tag{2.40}$$

The frequency dependent refractive index n is directly related to the materials relative permittivity ϵ_r and relative permeability μ_r:

$$n^2 = \epsilon_r \mu_r \tag{2.41}$$

For most organic materials μ_r can be approximated to 1, since they are not magnetic at optical frequencies. [63]

2.3.1 Birefringence

While most materials have an isotropic refractive index described by a scalar number n, some materials show a dependence of the direction and polarization of the incoming light. This phenomenon is called birefringence. In the case of an uniaxial material, the refractive index can be visualized by a rotational ellipsoid (spheroid) (see fig. 2.4). In this case the refractive index has an ordinary component n_o for light propagating parallel to the optical axis and an

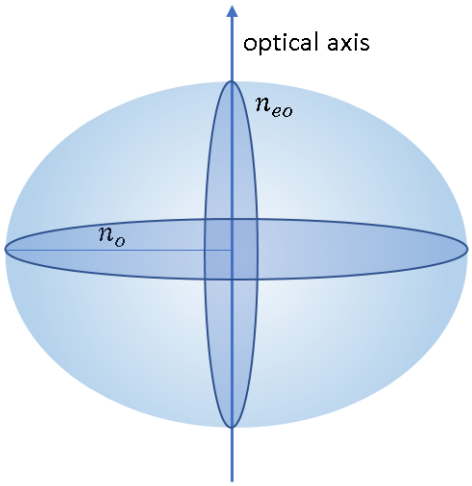

Fig. 2.4.: Index ellipsoid of the refractive index in the case of an uniaxial material with an ordinary component n_o and an extraordinary component n_{eo}.

extraordinary component n_{eo} for light propagating perpendicular to the optical axis.

The origin of birefrigience in amorphous organic thin films fabricated by physical vapor deposition can be attributed to two separate factors: First, an individual molecule normally has an anisotropic molecular polarizability (see section 2.3.2) which is closely related to the refractive index of the material (see section 2.3.3). Second, the deposition process itself introduces an asymmetry between the deposition direction and the film plane due to the vacuum border, which can lead to a preferred ordering of molecules. Since the conditions are isotropic inside of the film plane, the film has to be uniaxial with an optical axis parallel to the deposition direction. [63]

2.3.2 Thole model

When an external electric field $\mathbf{E}^{\text{ext}}$ is applied to a molecule, e.g. a light wave traveling through material, the electron density of the molecule is shifted by a certain amount leading to an induced polarization dipole $\boldsymbol{\mu}^{\text{ind}}$. The amount and direction of this polarization is quantified by the molecular polarizability tensor $\boldsymbol{\alpha}^{\text{mol}}$:

$$\boldsymbol{\mu}^{\text{ind}} = \boldsymbol{\alpha}^{\text{mol}} \cdot \mathbf{E}^{\text{ext}} \tag{2.42}$$

While $\boldsymbol{\alpha}^{\mathrm{mol}}$ can be calculated by quantum mechanical methods like DFT, such *ab-initio* calculations are often time consuming and further limited by the maximal system size that is computationally feasible. A classical, semi-empiric approach to calculate $\boldsymbol{\alpha}^{\mathrm{mol}}$ was published by Thole in 1981 [64]. Based on this initial approach, several further improved and specialized methods have been developed, which are typically still all referred to as Thole models. The basic assumption of all methods is, that every atom i inside a molecule can be viewed as an isotropically polarizable dipole with a scalar polarizability α_i. The induced dipole $\boldsymbol{\mu}_i$ at atom i is then given by

$$\mu_{i,\alpha} = \alpha_{i,\alpha\beta} \left(E_{\beta}^{\mathrm{ext}} + \sum_{j \neq i}^{N} T_{ij,\beta\gamma} \mu_{j,\gamma} \right) \tag{2.43}$$

using the Einstein summation convention. Here, $T_{ij,\beta\gamma}$ is the Thole dipole field tensor or dipole interaction tensor defined as:

$$T_{ij,\beta\gamma} = \frac{3 r_{ij,\beta} r_{ij,\gamma}}{r_{ij}^{5}} - \frac{\delta_{\beta\gamma}}{r_{ij}^{3}} \tag{2.44}$$

with the distance vector $\mathbf{r}_{ij} = \mathbf{r}_j - \mathbf{r}_i$ between two atoms i and j. Under the assumption that the induced molecular dipole is simply a sum of all induced atomic dipoles [65]:

$$\boldsymbol{\mu}^{\mathrm{ind}} = \sum_{i=1}^{N} \boldsymbol{\mu}_i \tag{2.45}$$

equations 2.43 and 2.44 can be solved for $\boldsymbol{\alpha}^{\mathrm{mol}}$:

$$\alpha_{\alpha\beta}^{\mathrm{mol}} = \sum_{i,j=1}^{N} B_{ij,\alpha\beta} \tag{2.46}$$

with the relay matrix

$$\mathbf{B} = \left(\boldsymbol{\alpha}^{-1} - \mathbf{T} \right)^{-1} \tag{2.47}$$

Already for a molecule consisting of two atoms, it can be shown that solving these equations leads to a diverging or possibly even negative molecular polarizability for sufficiently small distances between both atoms. This behaviour is called the "polarizability catastrophe" and can be avoided by a modification of the interaction tensor. In this work the IM-SQRT approximation described in [66] was used.

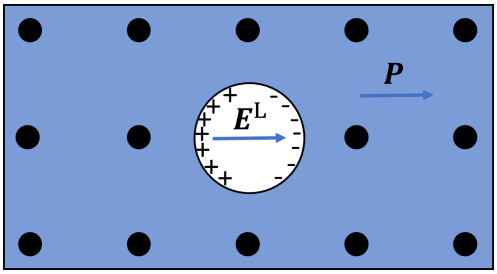

Fig. 2.5.: Electric Lorentz field $\mathbf{E}^{\mathrm{L}}$ in a spherical cavity inside a homogeneously polarized dielectric due to the charge density on the sphere surface.

2.3.3 Clausius-Mossoti equation

As seen in eq. (2.41) the refractive index can be directly related to the relative permittivity of a given material, which itself connects the macroscopic polarization density $\mathbf{P}$ to the electric field $\mathbf{E}$:

$$\mathbf{P} = (\epsilon_r - 1)\,\epsilon_0 \mathbf{E}^{\mathrm{ext}} \tag{2.48}$$

Assuming that the material can be described by an evenly distributed molecule density N of isotropic polarizable molecules, the polarization density is also given by:

$$\mathbf{P} = N\boldsymbol{\mu}^{\mathrm{ind}} = N\alpha\mathbf{E}^{\mathrm{local}} \tag{2.49}$$

where α is the isotropic molecular polarizability and $\mathbf{E}^{\mathrm{local}}$ is the local electric field acting on each molecule. This local field is the sum of the external field $\mathbf{E}^{\mathrm{ext}}$ and the field created by the induced dipoles inside of the material.

$$\mathbf{E}^{\mathrm{local}} = \mathbf{E}^{\mathrm{ext}} + \mathbf{E}^{\mathrm{L}} \tag{2.50}$$

To calculate the missing local contribution $\mathbf{E}^{\mathrm{L}}$ a spherical cavity around one molecule is cut out of the material. The field in this cavity due to the charge density on the sphere surface is called Lorentz field and can be directly related to $\mathbf{P}$ (see fig. 2.5):

$$\mathbf{E}^{\mathrm{L}} = \frac{\mathbf{P}}{3\epsilon_0} \tag{2.51}$$

Combining equations 2.48 to 2.51 leads to:

$$\frac{\epsilon_r - 1}{\epsilon_r - 2} = \frac{N\alpha}{3\epsilon_0} \tag{2.52}$$

Using $N = \frac{N_A \rho}{M_m}$ with the mass density ρ, Avogadro constant N_A and molar mass M_m of the molecule leads to the *Clausius-Mossotti* equation:

$$\frac{\epsilon_r - 1}{\epsilon_r - 2} \frac{M_m}{\rho} = \frac{N_A \alpha}{3\epsilon_0} \tag{2.53}$$

This equation serves as a connection between the microscopic properties (molar mass and polarizability) and the macroscopic properties (relative permittivity and mass density). [63]

3 Fundamentals of Organic Electronics

The field of organic electronics comprises several areas of application where the central functional unit is made up of small organic molecules or polymers. These molecules or polymers are designed in such a way, that they posses properties which are usually reserved for inorganic materials, most notably their electrical conductivity. An important class of materials are the organic semiconductors, which exhibit semiconducting properties upon charge injection. For this reason, they can be used in modern displays or solar cells, offering unique benefits over their inorganic counterparts.

In this chapter the fundamental working principles of organic light emitting diodes (OLEDs) are presented. Section 3.1 introduces the concept of an organic semiconductor, which are the building blocks of organic electronics. The schematic structure of a modern OLED stack is explained in section 3.2. Furthermore properties influencing the efficiency are listed there. Lastly, in section 3.3 two other applications of organic semiconductors are briefly introduced.

3.1 Organic semiconductors

Organic semiconductors are made up of small organic molecules or polymers often forming an amorphous solid. In a traditional inorganic semiconductor the periodic arrangement of atoms inside a crystal lattice leads to the formation of a electronic band structure with a band gap E_g between a filled valence band (VB) and an empty conduction band (CB) at $T = 0\,\mathrm{K}$. With rising temperature, the CB fills with free electrons and the VB with free holes, leading to an intrinsic electrical conductivity of the semiconductor.

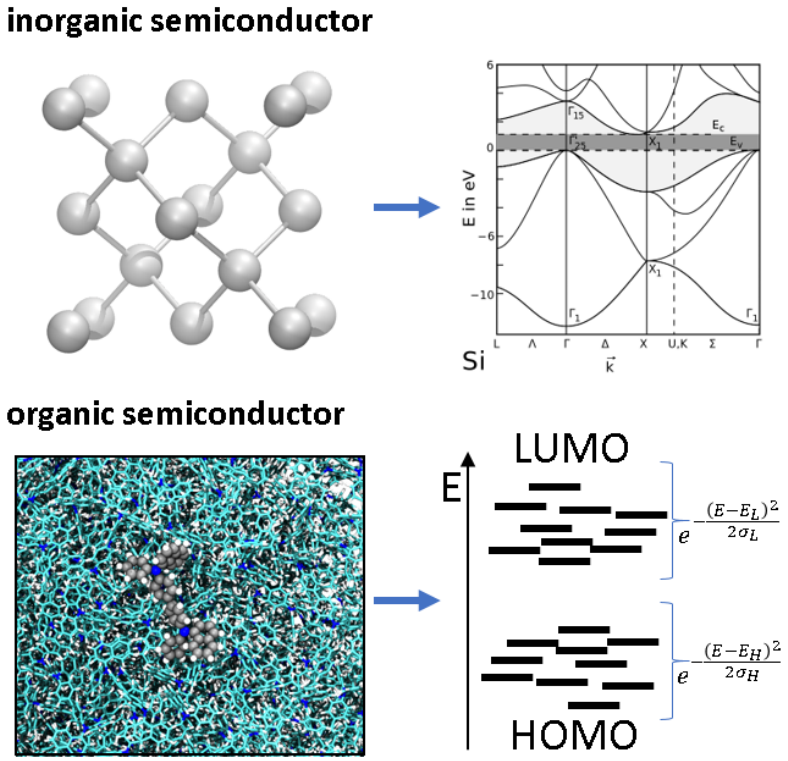

Fig. 3.1.: In an inorganic semiconductor, the covalently bonded atoms usually arrange in a crystal structure. This periodic structure leads to the formation of electronic bands which are typically separated by an energy gap. In an organic semiconductor the individual molecules form a amorphous bulk structure, mostly bonded by van der Waals forces. The individual environment of a molecule shifts its energy levels. Averaged over the whole bulk these shifts can be described by a gaussian distribution.

The similarity to organic semiconductors arises when looking at their electronic structure, which its determined by the molecular orbitals of the organic molecule. The orbitals of main interest for its charge transfer properties are the highest occupied molecular orbital (HOMO) and the lowest unoccupied molecular orbital (LUMO). In an amorphous bulk, the molecules are mostly held together due to their Van-der-Waals attraction and especially do not form covalent bonds between each other. In this lies the first main difference to inorganic semiconductors, where the whole bulk is connected by covalent bonds leading to completely delocalized electronic states. Although influenced by their environment, the molecular states inside the organic semiconductor

bulk are mostly localized on the individual molecules. Due to their amorphous structure the individual environment is different for each molecule, resulting in a gaussian distribution of states for the HOMO and LUMO levels (see fig. 3.1):

$$D(E) \approx e^{-\frac{(E-E_m)^2}{2\sigma_m^2}} \tag{3.1}$$

where E_m and σ_m are the mean value and standard deviation of the respective molecular orbital energies. This also means that the electronic properties of the final device are strongly correlated to the electronic structure of the single molecule, as well as the environment of the molecule which arises from the structure formation process. The influence of the latter being one of the points of study in this thesis.

The core building blocks, which are present in almost all organic semiconductor molecules, are aromatic ring systems. The most basic aromatic system being the benzene ring, consisting of six carbon and six hydrogen atoms. In their ring conformation, each carbon is sp^2 hybridized forming three strong covalent σ-bonds inside the ring plane and one bond between the $2p_z$ orbitals which are perpendicular to the ring plane. The so formed π-orbitals are delocalized over the whole ring. This notion of delocalized π-orbitals persists also for larger aromatic systems leading to a "band-like" charge transport along the π system of a molecule. Between two molecules, charges can be transferred due to overlap of molecular orbitals, leading to a hopping transport between neighboring molecules. With the exception of (poly)crystalline organic films showing overall band like transport [67], the intramolecular charge transport is usually much faster than the intermolecular hopping transport and therefor often neglected in calculations. The modeling of charge transport for organic semiconductors is further explained in section 4.3.4. [68]

3.2 Organic Light Emitting Diodes (OLED)

An OLED works by converting the energy of injected holes and electrons into visible light. This is facilitated through the recombination of a free electron with a free hole on a single (emitter) molecule. This electron hole pair on the molecule represents an excited state referred to as an exciton state, or simply exciton. The exciton ideally decays under the emission of a photon, which

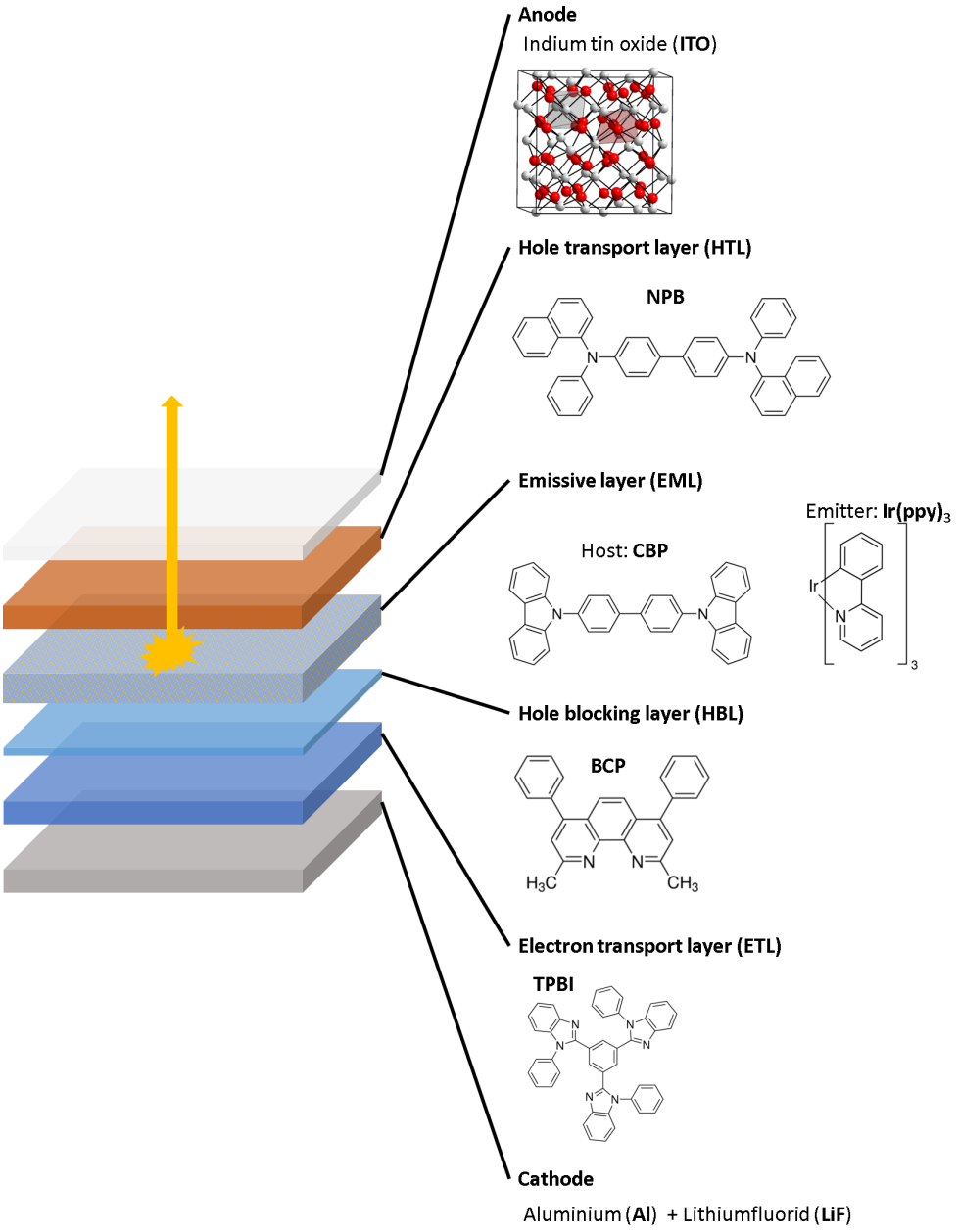

Fig. 3.2.: Schematic view of an OLED device. The device consists of several organic layers between two metallic electrodes. The top electrode is typically made of the transparent Indium tin oxide (ITO), the bottom electrode is typically Aluminium (Al) coated with a thin Lithiumfluorid (LiF) layer. For each organic layer a commonly used and studied material is given as an example. The full names are: N,N'-Di-[(1-naphthyl)-N,N'-diphenyl]-(1,1'-biphenyl)-4,4'-diamin (NPB), 4,4'-Bis-(N-carbazolyl)-1,1'-biphenyl (CBP), Tris-[2-phenylpyridinat-C2,N]-iridium(III) ($Ir(ppy)_3$, Bathocuproin (BCP) and 2,2',2"-(1,3,5-Benzinetriyl)-tris(1-phenyl-1-H-benzimidazole) (TPBI). Picture of ITO taken from `https://commons.wikimedia.org/wiki/File:Kristallstruktur_Lanthanoid-C-Typ.png`

then can leave the OLED device. While this principle of electroluminescence in organic materials is known since 1953 [69], the first real OLED device was published by Ching W. Tang and Steven Van Slyke in 1987 [2]. While they used a two layer system with Tris(8-hydroxyquinolinato)aluminium acting as both an electron transport material and emitter, modern devices consist of many different layers. In fig. 3.2 a schematic view of the most common layer types is presented. Deciding how thick each layer has to be and what material is used in combination with the other layers, is the main challenge of modern OLED device improvement. [68]

3.2.1 Injection and Transport

Since the separation between HOMO and LUMO levels is often several electron volts, the intrinsic free charge density is very low in an organic semiconductor. Therefore, a good charge injection at the metal-organic interface is a key component for device operation. The difference between the work function of the metal and the HOMO/LUMO level of the respective organic material can lead to interface dipoles [70], further hindering charge injection. To minimize this, a good match between work function and HOMO/LUMO level needs to be found, limiting the number of electrode materials. The most common anode material used in almost all OLED devices is Indium tin oxide (ITO), which combines a relatively high work function of 4.4-4.5 eV [71] with the optical transparency needed for light extraction. For the cathode, low work function metals like Ca, Ba and Mg can be used. However, due to their strong reactivity with air and water, the cathode is often made out of a more stable material like Al coated with a thin LiF film serving as an additional electron injection layer.

After the injection of charges into the organic films, transporting them to the emitting molecule is the next step. To this end, transport layers for holes and electrons (HTM and ETM) are put next to their respective electrode. The main parameter defining the charge transport inside these layers, is the hole or electron mobility $\mu_{\mathrm{h/e}}$. The mobility is typically less than $0.001\,\mathrm{cm}^2/\mathrm{Vs}$ and therefor several orders of magnitude lower than in inorganic semiconductors [72] [73]. Due to this organic layers need to be very thin, often in the order

of 10 to at maximum several $100\,\mathrm{nm}$, to minimize ohmic losses of the device. [74]

Besides the transport of charges, the HTM and ETM can also function as an additional blocking layer, preventing the opposite charge carries from entering, additionally reducing ohmic losses of the device. [68]

3.2.2 Emission

The emissive layer of an OLED is normally made up of two materials forming a guest/host system, with the guest being an emitter molecule. Ideally these are designed in such a way that charges get spatially trapped on a emitter molecule, increasing the chance of exciton formation. According to spin statistics, 25% of the formed excitons are in the singlet state and 75% in the triplet state. While the singlet excitations can decay to the ground state via emission of a photon (fluorescence), the optical transition from a triplet state is prohibited by the electronic selection rules. This limits the internal quantum efficiency (IQE) to a maximum of 25% for a standard fluorescent organic emitter. [68]

3.2.3 Outcoupling efficiency

In general, the efficiency of an OLED stack is often quantified by its external quantum efficiency (EQE). The EQE of an OLED is defined as a product of charge balance γ, exciton formation efficiency η_r, quantum yield Φ_p and outcoupling efficiency η_p [75]:

$$\eta_\mathrm{ext} = \gamma \cdot \eta_\mathrm{r} \cdot \Phi_\mathrm{p} \cdot \eta_\mathrm{p} \tag{3.2}$$

The product of the first three factors of this equation is often also referred to as the internal quantum efficiency (IQE), which is limited to 25% for a standard fluorescent emitter as described in section 3.2. Throughout the years, several new materials and mechanisms have been developed to increase the IQE to nearly 1. The most prominent being Ir based emitters, which offer a faster phosphorescent decay from the triplet to the ground state enabled by spin-orbit coupling. [15]

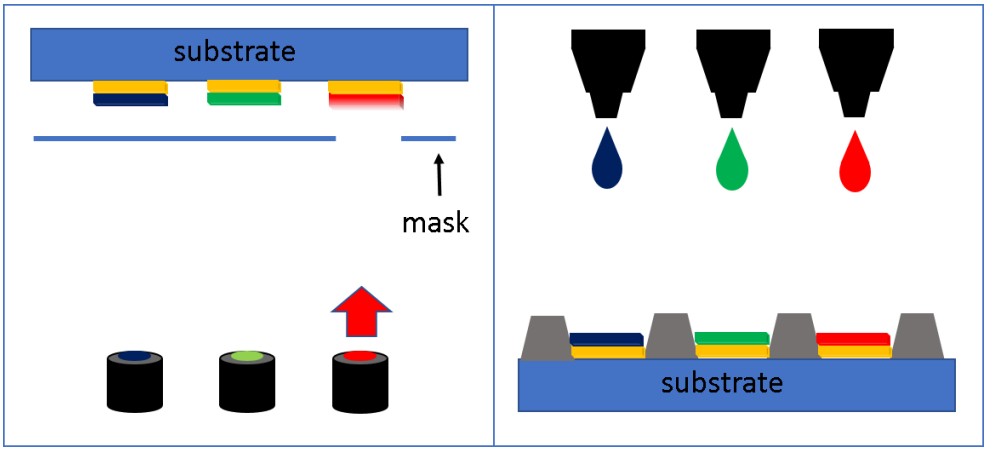

Fig. 3.3.: Schematic view of two OLED fabrication processes. Left side: Physical vapor deposition of organic materials by heating up the material source creating a vapor which condenses on the substrate. The formation of individual pixels is achieved by the use of different masks. Right side: Ink jet printing of diluted organic materials onto a substrate.

With the IQE reaching close to 100%, the last factor of eq. (3.2) comes to great importance. The outcoupling efficiency η_p describes the fraction of generated photons which actually leave the device and contribute to the final device luminosity. Besides the optical parameters of the organic films in the stack, one main contributor to the outcoupling efficiency is the molecular orientation of emitter molecules inside their host matrix. To understand this, a emitter molecule can be thought of as a combination of several dipole antennas emitting an electromagnetic wave. The orientation of these antennas is hereby parallel to the specific transition dipole moment of an allowed optical transition of the excited molecule. Same as for a classical antenna, the intensity of the emitted wave is at its maximum perpendicular to the antenna direction and 0 along the antenna direction. [68]

3.2.4 Device manufacturing

While there are OLEDs used in standard lighting applications the main use case is in modern smartphone and TV displays, where they offer a thinner design, combined with a theoretically infinite contrast ratio and a possibly better power efficiency compared to LCD based displays. A standard OLED pixel consists typically of red, green and blue pixels ordered in a specific grid

structure. Considering the high demand of displays, a low cost and scalable fabrication process is needed. So far this can, for example, be achieved by the subsequent physical vapor deposition of different organic materials using a mask or potentially even by ink jet printing of diluted organic materials (see fig. 3.3). While the latter seems more promising from a production and cost point of view, solution based films often perform worse compared to vapor based films [76]. Furthermore, films fabricated by physical vapor deposition also show a higher thermal stability compared to solution based films [77]. Because of these issues the more complex and expensive physical vapor deposition still remains as the de-facto industry standard for OLED production.

3.2.5 Degradation

When discussing OLED displays and especially TVs the issue of burn in often is mentioned. In general, burn in means the permanent retention of static images on the screen after some time of display usage and is observed for different display types for different reasons. In an OLED, this issue is theoretically possible due to the degradation of the organic material after time or heavy use. The total degradation is a combination of externally induced factors like instabilities of the electrode materials or fabrication errors leading to oxygen and moisture infiltration [78] and internal degradation processes during device operation. These internal processes are mostly linked to non-radiative recombination processes, which are also referred to as quenching. This is especially important for blue emitters, where no stable Ir based emitters with a high IQE have been found yet. Therefore in modern displays often a combination of high efficiency phosphorescent red and green pixels is combined with a low efficiency fluorescent blue emitter [79].

3.3 Other applications

Besides OLEDs there are also other fields of application for organic semiconductors. As an example, the principles of organic photovoltaics (OPV) and organic field effect transistors are very briefly explained in this section.

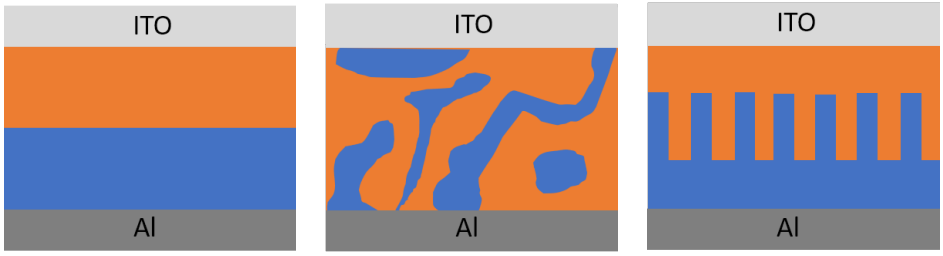

(a) Neat double layer **(b)** Dispersed heterojunction **(c)** Idealistic heterojunction

Fig. 3.4.: Three qualitatively different forms of a two material based OPV cell: (a) A neat double layer morphology similar to a OLED device. (b) A dispersed bulk heterojunction of the two organic materials with domains which are disconnected from their respective electrode. (c) An idealistic bulk heterojunction.

3.3.1 Organic photovoltaics (OPV)

Similar to traditional silicon based photovoltaic devices, an OPV cell aims to generate electrical power through the absorption of sun light. On a molecular level the processes are sort of reversed when compared to an OLED: First a photon is absorbed on a specific site, creating an exciton. This exciton then may diffuse in the material and eventually either decays or separates into a free electron and hole. Then the free charges can travel to opposite electrodes generating a current.

Besides the already mentioned challenges in organic semiconductor design, the film morphology of an OPV plays a crucial role for overall device performance. This can be understood when looking at the three different blends of acceptor and donor materials in fig. 3.4. Due to the smaller ϵ value of organic semiconductors compared to inorganic semiconductors ($\epsilon = 4.4$ for C_{60} and $\epsilon = 11.9$ for Si [80]), the attractive force between electrons and holes is larger hindering exciton dissociation. The thermal energy available at ambient conditions is too small for excitons to separate into free holes and electrons. In an OPV device, this separation mainly occurs at the acceptor-donor boundary. Since the exciton can only diffuse several nanometers before decaying again, the effective absorption region for photocurrent generation is limited to a small region close to these acceptor-donor boundaries. Because of this, neat double layer structures like in an OLED are very inefficient. Therefore, a blend of both materials called "bulk heterojunction" has risen in popularity, maximizing the

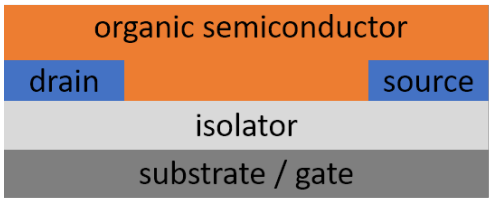

Fig. 3.5.: Schematic view of a bottom gated organic field effect transistor (OFET).

boundary surface. One drawback of these heterojunctions is the formation of material isles which are separated from their respective electrodes, possibly leading to the trapping of charges. The desired ideal heterojunction morphology would be a structure of intertwined pillars as depicted in fig. 3.4 (c), which would maximize the boundary surface and at the same time minimize charge trapping. [81]

3.3.2 Organic field-effect transistor (OFET)

Organic field-effect transistors (OFETs) are another form of application for organic semiconductor materials with the potential to offer a cheaper, more sustainable, lighter and more flexible alternative to their inorganic counterparts. Like in a conventional FET, the current between drain and source is controlled by a gate voltage (see fig. 3.5).

While most OFETs still use inorganic materials as electrode or substrate materials, all-organic OFETs are possible. Recently an all-organic OFET printed on a paper substrate was reported by Casula *et al.* [82]. Their device combined desirable mechanical properties with a low-cost and highly scalable fabrication technique.

4 Methods

For the simulations and subsequent analysis steps performed in this work, several different workflows have been used. The methods to generate atomistic thin film structures are explained in section 4.1. In section 4.2 the analysis methods to characterize the packing and arrangement of molecules in the film morphology is presented. Finally, section 4.3 describes the analysis of electronical film properties.

4.1 Modelling of physical vapor deposition

As already mentioned in section 3.2, the main method of fabricating thin organic films is by physical vapor deposition of the organic molecules onto a substrate or a previously deposited film. This process introduces a spatial asymmetry between the substrate plane and the layer growth direction. For most molecules and use cases of the simulated structures, it is therefor not possible to perform simulations of molecules in a 3-D periodic system. In this section, two different simulation approaches aimed at generating atomistic thin film structures are presented: First, section 4.1.1 an all atom molecular dynamics approach is introduced. Second, a Monte Carlo based algorithm is explained in section 4.1.2.

4.1.1 Molecular Dynamics approach

In the following the parametrization and deposition process for the MD approach are introduced. The described deposition workflow is loosely based on a previously published approach by Dalal *et al.* [83], where the temperature dependent film formation of the common organic semiconductor N,N'-Bis-(3-methylphenyl)-N,N'-diphenylbenzidin (TPD) is simulated using a coarse-grained Lennard-Jones model. In contrast to this, the approach in

this work uses the all atom GROMOS 54A7 forcefield [51] combined with a particle-particle particle-mesh (PPPM) solver [84]. Since the system of interest is only periodic in the plane (xy), perpendicular to the deposition axis and non-periodic in the deposition direction (z-axis), the summation method for slab like systems described by Yeh *et al.* [85] is used for the PPPM solver. All MD simulations were performed with the Large-scale Atomic/-Molecular Massively Parallel Simulator (LAMMPS), which is freely available on `http://lammps.sandia.gov` [86].

Parametrization

As I explained in section 2.2.1, the molecular mechanical forcefield is at the core of every molecular dynamics simulation. Since the focus of this work lies on the comparison of different simulation approaches and not on the performance of the individual force field, the openly available parameters from the GROMOS 54A7 forcefield [87] [88] [89] were used. To parameterize the force field parameters of a given molecule, the chemical structure was manually created with the MarvinSketch software[1]. With this, a first guess of the 3D structure was generated and saved in the Protein Data Bank (.pdb) file format. This file was then uploaded to the Automated Topology Builder (ATB)[2] [90] [91]. After uploading, ATB automatically optimizes the molecular structure and parameterizes the molecule using the GROMOS 54A7 force field parameters. It also creates input files compatible with many molecular dynamics packages (e.g. LAMMPS and GROMACS). If not mentioned otherwise, all materials used in MD simulations were parameterized according to this procedure.

Deposition

For the deposition a simulation box with a length of $10\,\mathrm{nm}$ in x- and y-direction aswell as $21\,\mathrm{nm}$ in z-direction with 2 dimensional periodic boundary conditions in the xy-plane was used. To prevent atoms from leaving the simulation box

[1] available on `https://www.chemaxon.com`
[2] available under `https://atb.uq.edu.au/`

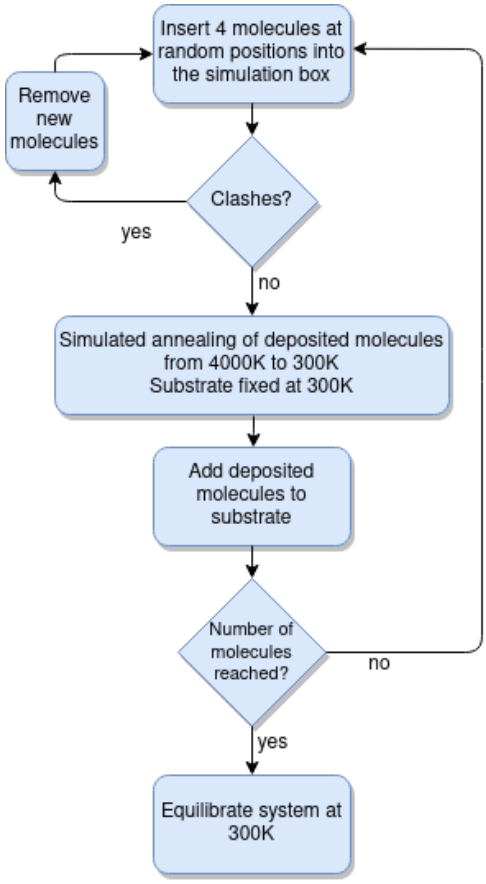

Fig. 4.1.: Workflow diagram for the deposition process simulated with Molecular Dynamics.

along the z-direction, harmonic wall potentials were introduced at the top and bottom edge of the simulation box:

$$E_{\text{wall}} = \epsilon \left(r - r_c\right)^2 \qquad r < r_c \tag{4.1}$$

Here r is the distance of an atom to the respective harmonic wall (i.e. the top and bottom edges of the simulation box), $\epsilon = 0.2\,\text{kcal mol}^{-1}$ is the strength of the wall and $r_c = 1\,\text{nm}$ is the cutoff distance after which the harmonic potential is turned off. Before the deposition simulations start, first a starting substrate film was generated inside this simulation box. The sole purpose of this substrate film is to generate a reference point where new molecules can attach to. To minimize the influence of the used substrate material, the well known organic molecule buckminsterfullerene (C_{60}) was used, which due to its symmetry has no partial charges and therefor effectively acts as a nearly perfect Lennard-Jones surface. To prepare the substrate 180 C_{60} molecules were put on an evenly spaced grid inside of the simulation box. Then a constant force of $0.2\,\text{kcal mol}^{-1}\text{Å}^{-1}$ towards the negative z-direction was applied to every carbon atom. The so initialized system was then equilibrated at T =300 K for $250\,\text{ps}$ with a timestep of $\Delta t = 2\,\text{fs}$. This produced a flat and almost two monolayers thick film of C_{60}.

The deposition itself (see workflow diagram in fig. 4.1) was then simulated by iteratively introducing four new, randomly oriented molecules approximately 1 nm above the substrate film. The xy-coordinates where also chosen at random. After that a overlap check was performed by calculating the minimal atom-atom distances between every newly inserted molecule and all other molecules inside the simulation box. If this minimal atom-atom distance is below 3 Å the newly introduced molecule is rejected and a new one is inserted. This is repeated until four non-overlapping molecules are found. The starting velocities of the inserted molecules were initialized with $0.005\,\text{Å/fs}$ towards the surface. Then, a molecular dynamics simulation is performed for a previously defined fixed amount of steps. During these steps, the newly introduced molecules undergo a simulated annealing procedure in which their temperature T_n gets adjusted from a high starting value $T_\text{high} = 4000\,\text{K}$ to the final value $T_\text{low} = 300\,\text{K}$:

$$T_\text{n} = T_\text{high} \cdot \left(\frac{T_\text{low}}{T_\text{high}}\right)^{\frac{n}{N}} \tag{4.2}$$

This is done to increase the molecules energy to overcome potential energy barriers in the high dimensional phase space, which otherwise would only be reached by an increase of the simulation time. Also this achieves more consistency when comparing results with the Monte Carlo procedure described in section 4.1.2, which uses the same temperature scaling. During the deposition process, the substrate and all previously deposited molecules are kept fixed at $300\,\mathrm{K}$. For both the substrate and the newly inserted molecule a NVT ensemble with a Nosé-Hoover thermostat for the fixed $300\,\mathrm{K}$ region and a Berendsen thermostat for the simulated annealing region is used. After the last molecules are deposited, the whole system is equilibrated at $300\,\mathrm{K}$ with a Nosé-Hoover thermostat. To enable a timestep of $2\,\mathrm{fs}$, the Hydrogen bonds, which contribute to the fastest vibrations in the investigated systems, are constrained via a shake algorithm [92]. After this final equilibration the system is cooled down to $0.1\,\mathrm{K}$ during $400\,\mathrm{ps}$. Through this final cooling, most of the bond lengths and bond angles in the structure reach their equilibrium values, allowing the structure to be analyzed with the QuantumPatch approach (see section 4.3.3) were DFT calculations need to be performed on the individual molecular geometries in the film. The density of the film and overall orientation of the molecules remain largely unaffected by this short cooling process, due to a manual fixing of the center of mass of each molecule during the cooling process.

4.1.2 Monte Carlo approach

The Monte Carlo procedure used in this work is based on the work by Tobias Neumann [29] and obtainable in the Deposit software package[3]. In this section, I will briefly summarize how the molecules are parameterized and how the deposition process is simulated in Deposit.

Parametrization

For the parametrization a set of Lennard-Jones parameters and partial charges has to be assigned to every atom of a given molecule. Additionally, a forcefield for dihedral rotations of molecular fragments (see fig. 4.2) can be defined. In principle, the partial charges and dihedral forcefields can be calculated by ab

[3] commercially available at `https://www.nanomatch.com/`

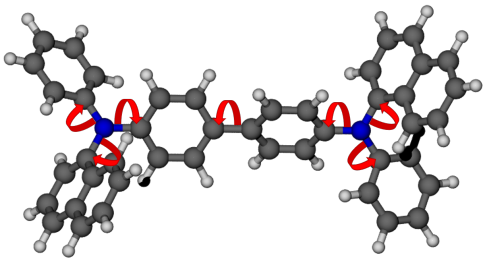

Fig. 4.2.: The seven possible dihedral rotational degrees of freedom of a NPB molecule during the deposition process in Deposit.

initio methods. For a better comparison to the results obtained by molecular dynamics, the Lennard-Jones parameters, charges and dihedral forcefields were extracted from the files generated by the ATB mentioned in section 4.1.1, if not explicitly stated otherwise.

Deposition

Like in the MD deposition process, a simulation box with periodic boundary conditions in the xy plane is used in Deposit. Figure 4.3 shows a workflow diagram of the deposition simulation. During the simulation, new molecules are inserted one at a time. The position and configuration of the new molecule is then altered by a random move, which could either by a translation, rotation or dihedral fragment rotation. In contrast to the MD deposition, bond lengths and bond angles are explicitly not changed during the simulation. Each random move is then either accepted or rejected based on the Metropolis Monte Carlo criterion (see eq. (2.36) in section 2.2.2). The energy difference ΔE is calculated by the energy E_i before and energy E_f after the random move. The total energy E_{tot} of a given state of the molecule is defined by:

$$E_{\text{tot}} = E_{\text{LJ}} + E_{\text{C}} + E_{\text{DH}} \tag{4.3}$$

where E_{LJ} and E_{C} are the intermolecular Lennard-Jones and Coulumb interaction energies and E_{DH} is the intramolecular contribution due to the dihedral rotations. Since previously deposited molecules are kept fixed and are thereby

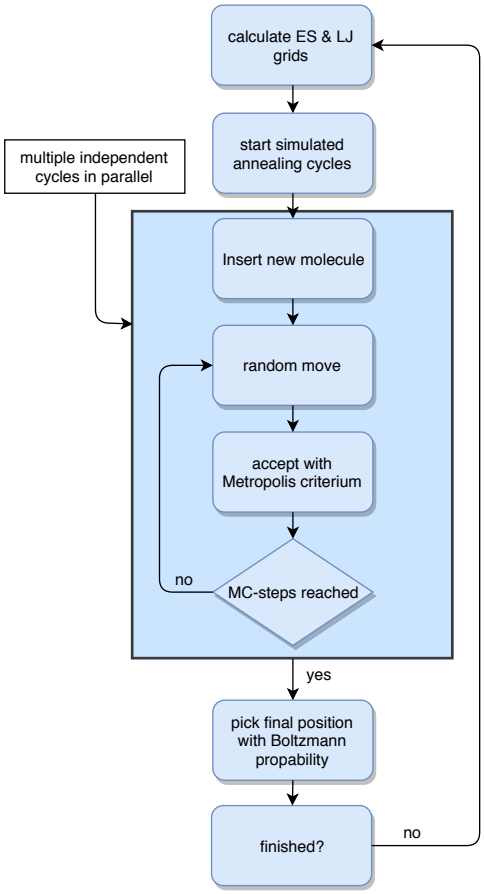

Fig. 4.3.: Workflow diagram for the deposition process simulated with Monte Carlo.

effectively frozen, the intermolecular energy evaluation can be reduced to a computationally efficient lookup by using previously calculated Lennard-Jones and electrostatic grids. The electrostatic grid at a given grid position is the sum over the Coulomb potentials generated by the partial charges of previously deposited atoms. For the Lennard-Jones part, a separate grid for every existing Lennard-Jones parameter combination in the current simulation is generated.

The deposition itself consists of several simulated annealing (SA) cycles, which run in parallel. In each cycle, the molecule starts at a different random starting position and reaches its final position after a set amount of Monte-Carlo moves. From these final positions, one position is chosen with a Boltzmann probability at a defined acceptance temperature T_{acc}. After that, all grid values are updated by adding the contributions of the newly deposited molecule and the deposition of the next molecule can start. This process is repeated until the specified number of deposited molecules is reached or the simulation box is full.

4.2 Structural Analysis

In this section the structural analysis methods used to calculate the mass density (section 4.2.1), radial distribution function (section 4.2.2) and orientation parameter of molecular fragments (section 4.2.3) are explained.

4.2.1 Density

To calculate the mass density of a given simulated structure, the total mass $m(h)$ of atoms contained in a box of height h is calculated. The base area of the box is $A = L_x \cdot L_y$, where L_x and L_y are the sizes of the simulation box in x and y direction. The density of this box is then given by

$$\rho(h) = \frac{m(h)}{h \cdot L_x \cdot L_y} \tag{4.4}$$

The center of the box is placed at the center of mass of the whole structure (see fig. 4.5). After increasing the box height, the density begins to converge at some plateau value and decreases again at higher heights due to the surface

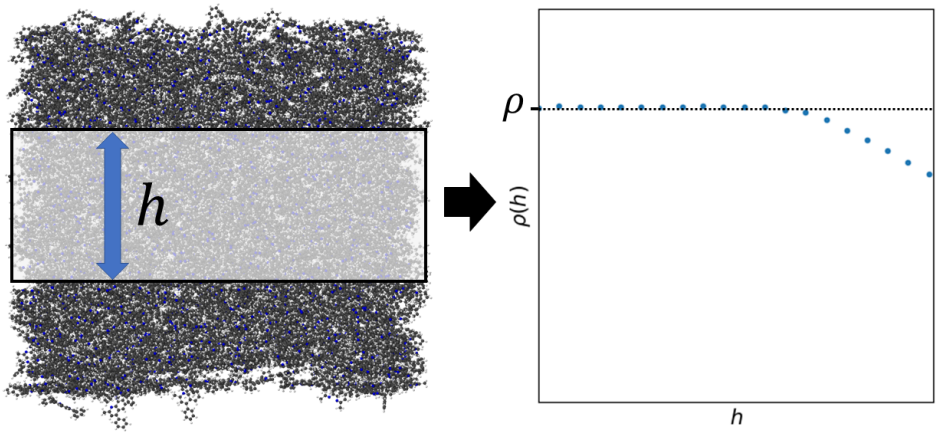

Fig. 4.4.: Calculation process of the simulated film density.

roughness at the film edges in z-direction. The final density ρ of the film is then determined by a least squares fit of the densities in the plateau region.

4.2.2 Radial distribution function

The radial distribution function $g(r)$ of a set of particles can be interpreted as a measure of their local packing. It is defined as the frequency of finding another particle at distance r from an initial particle and can be calculated by

$$g\left(r\right) = \frac{H\left(r\right)}{N \cdot V\left(r\right) \cdot \rho_0} \tag{4.5}$$

for a set of discrete positions. Here N is the number of histogram samples, $H\left(r\right)$ the histogram entry at distance r, $V\left(r\right)$ the volume of a distance bin in the histogram and ρ_0 the number density of particles in the film. For the 2D periodic structures in this work, an accurate choice for the histogram sampling is crucial. For example, if the pairwise distances between all molecular center of masses are counted, errors due to the edges of the simulation box in the z direction are introduced. Therefore, the center of mass pairs are chosen in a two step process (see fig. 5.5). At first all molecules inside a slab with height h are selected as samples for the histogram. Then around each molecule in

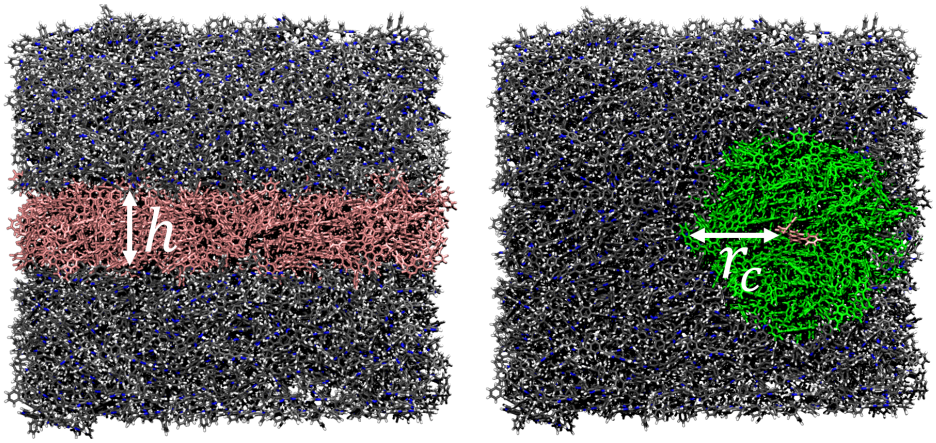

Fig. 4.5.: Selection process for the molecule pairs entering the radial distribution function calculation. Left side: Selection of all molecules (colored red) in a slab with height h around the center of geometry of the morphology. Right: Selection of all molecules (colored in green) inside a sphere with radius r_{cutoff} around each molecule determined in the previous step.

this inner group, all molecular pair distances are counted up until a cutoff radius r_{cutoff}. To ensure that no edge effects occur, $h/2 + r_{\text{cutoff}}$ needs to be smaller than half of the thinnest part of the morphology. With this restriction h and r_{cutoff} are chosen so that: (a) h is maximized to have a bigger sample size and therefor better statistics and (b) r_{cutoff} covers the range of interest in $g(r)$, which converges to 1 at large distances for amorphous systems.

4.2.3 Fragment orientation

To analyze the orientation of molecules in the final film, orientation parameters are calculated for the dihedral fragments which can rotate in both simulations approaches (e.g. for a NPB molecule the seven fragments can be obtained by splitting the molecule at every rotating bond in fig. 4.2). The orientation parameter is then defined as:

$$\left\langle \cos^2 \theta_z \right\rangle = \frac{1}{N_{\text{f}}} \sum_{i \in N_{\text{f}}} \left(\mathbf{n}^i \cdot \mathbf{e_z} \right)^2 \tag{4.6}$$

where N_{f} is the number of fragments, $\mathbf{e_z}$ the unit vector in z-direction and $\mathbf{n}^i$ the unit vector perpendicular to the fragment plane. The fragment plane itself

is determined by minimizing the squared distances to all fragment atoms. For a given set of fragment coordinates $\mathbf{c}_j^i$ the plane can be obtained by minimizing

$$\sum_j^N \left(\left(\mathbf{c}_j^i - \mathbf{p}^i \right) \mathbf{n}^i \right)^2 \tag{4.7}$$

where $\mathbf{p}^i$ is a point on the plane. In [93] it is shown that the minimal distance plane contains the center of geometry of the coordinates, therefore it is possible to take

$$\mathbf{p}^i = \bar{\mathbf{c}}^i = \frac{1}{N} \sum_j^N \mathbf{c}_j^i \tag{4.8}$$

With this, the problem can be solved by performing a singular value decomposition (SVD) of the matrix A^i constructed by the fragment coordinates with respect to their center of geometry $\tilde{\mathbf{c}}^i = \mathbf{c}_j^i - \bar{\mathbf{c}}^i$:

$$A^i = \begin{pmatrix} \tilde{\mathbf{c}}_{1x}^i & \cdots & \tilde{\mathbf{c}}_{Nx}^i \\ \tilde{\mathbf{c}}_{1y}^i & \cdots & \tilde{\mathbf{c}}_{Ny}^i \\ \tilde{\mathbf{c}}_{1z}^i & \cdots & \tilde{\mathbf{c}}_{Nz}^i \end{pmatrix} \tag{4.9}$$

After the SVD of A^i, three new matrices are obtained

$$A^i = USV^T \tag{4.10}$$

and $\mathbf{n}^i$ can be extracted as the third column of U. [94][93]

4.3 Analysis of electronic properties

In this section, the methods for calculating the electronic properties of the simulated thin films are presented.

4.3.1 Refractive index

As shown in eq. (2.53), the refractive index of a material can be directly related to the molecular polarizability. However in the derivation of eq. (2.53), the approximation of isotropically polarizable molecules is made. This approximation

does not hold up for most OLED materials and more importantly does not allow for birefrigience, which is a phenomena often found in thin organic layers due to a preferred molecular orientation during film formation [95] [96]. It has been shown, that a similar type of equation can be used for anisotropic systems if, instead of taking the polarizability of a single molecule, the polarizability of a spherical cutout of the film is taken. This cutout should be "sufficiently large, so that the material contained in it may be considered from a macroscopic point of view" (cited from [97]):

$$\frac{\epsilon^{(u)} - 1}{\epsilon^{(u)} + 2} = \frac{\alpha^{(u)}}{a^3} \tag{4.11}$$

In this equation u denotes the principal axes of the dielectric tensor $\epsilon^{(u)}$. Furthermore, a is the radius and $\alpha^{(u)}$ the principal value of the polarizability tensor of the spherical cutout. Due to the symmetry of the investigated structures, the material has to be uniaxial and the optical axis (which is a principal axis of $\epsilon^{(u)}$) coincides with the deposition direction z. Therefore the extra ordinary and ordinary refractive indices can be calculated by:

$$n_{eo} = \sqrt{\epsilon_{zz}} \tag{4.12}$$

$$n_o = \sqrt{\frac{\epsilon_{xx} + \epsilon_{yy}}{2}} \tag{4.13}$$

where the components of ϵ are calculated using eq. (4.11) with the respective components of α.

4.3.2 Giant surface potential

The giant surface potential (GSP) arises from the orientation of molecular dipole moments during the deposition process [98]. While the overall dipole of the film cancels out in the xy plane due its symmetry, a net dipole moment might remain in the z direction. With growing film thickness, this net dipole moment can lead to a potential difference between the bottom and top of the layer (see fig. 4.6). In general, the potential created by a set of dipoles is given by:

$$\Phi(\mathbf{r}) = \sum_i^N \frac{1}{4\pi\epsilon_0\epsilon} \frac{\mathbf{p}_i \cdot (\mathbf{r} - \mathbf{R}_i)}{|\mathbf{r} - \mathbf{R}_i|^3} \tag{4.14}$$

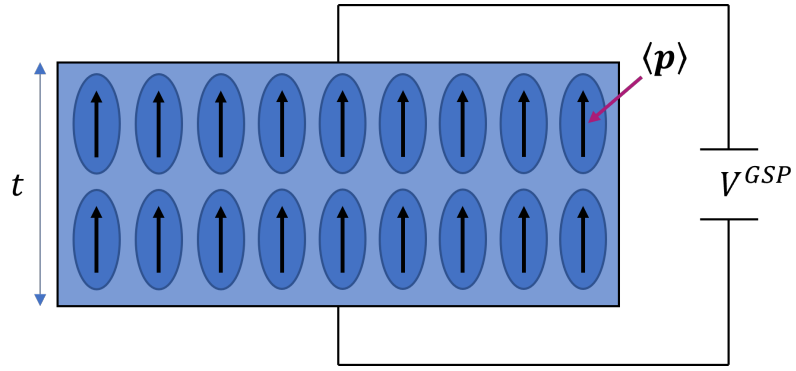

Fig. 4.6.: Buildup of the giant surface potential V^{GSP} for a thin layer of thickness t, due to a net average dipole moment $\langle \mathbf{p} \rangle$ along the deposition direction.

where $\mathbf{R}_i$ is the position of each dipole moment $\mathbf{p}_i$. Under the assumptions that each dipole moment has only a z-component ($\mathbf{p}_i = p_i \mathbf{e}_z$) and that the distribution of dipole moments can be described by a constant dipole density $\frac{\langle p \rangle}{V} = \text{const.}$, the total GSP can be calculated (derivation in appendix A of the appendix):

$$V^{\mathrm{GSP}} = \Phi\left(z = t\right) - \Phi\left(z = 0\right) = \frac{\langle p \rangle \, t}{V \epsilon_0 \epsilon} \tag{4.15}$$

Typically the giant surface potential is measured at several film thicknesses during the deposition process and quantified by the slope $\alpha = \frac{\langle p \rangle}{V \epsilon_0 \epsilon}$. This slope can be extracted from the simulated structures by calculating the dipole moment of each individual molecule in the film. To include the polarization of the surrounding environment in this calculation, the QuantumPatch method is used. [99, 100]

4.3.3 QuantumPatch

The QuantumPatch method is a algorithm to perform quantum chemical calculations including environmental effects by only performing calculations for one molecule at a time. The method was initially published by Friederich *et al.* [24] and is currently further developed by Nanomatch[4]. QuantumPatch was used throughout this work to calculate the dipole moments, energy level distributions and dimer couplings used for the GSP and mobility analysis in this work. To explain the underlying principle, a system consisting of four

[4] `https://www.nanomatch.com/`

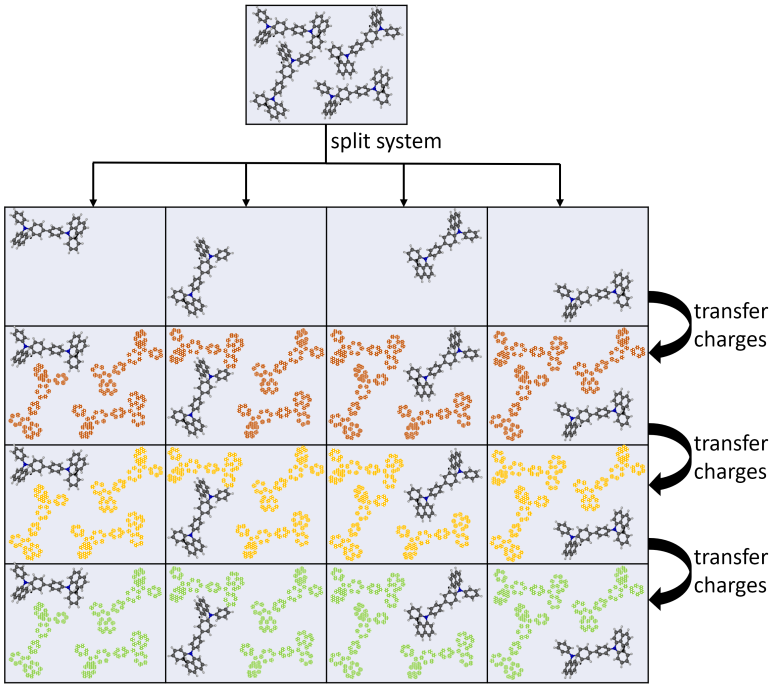

Fig. 4.7.: Workflow diagram of the QuantumPatch algorithm. A system consisting of four molecules is split into four boxes, each containing one molecule. For every box a DFT calculation is performed and partial charges are fit. The partial charges are then transferred to the next iteration of calculations, where they enter as an external electrostatic potential. This process is repeated until self convergence is reached. (Figure is adapted based on figure 1 of [24])

molecules is considered (see fig. 4.7). In the first iteration, a vacuum calculation is performed for each of the four molecules. Afterwards, partial charges are fitted to match the electrostatic potential of the molecule (see for example [101]). In the second iteration, the partial charges calculated in the previous calculation are used to model the environment. This procedure is then repeated until self-convergence is reached, which typically takes around seven iterations.

4.3.4 Modelling charge transport properties

As already mentioned in section 3.2, the charge transport in organic semiconductor materials can often be described by a hopping mechanism. A common model used to describe the hopping rate between two molecules in a bulk film is the Marcus rate equation [102] [103]:

$$k = \frac{2\pi}{\hbar} |J|^2 \frac{1}{\sqrt{4\pi\lambda k_\mathrm{B} T}} \exp\left(-\frac{(\lambda + \Delta E)^2}{4\lambda k_\mathrm{B} T}\right) \tag{4.16}$$

Besides the temperature T, the rate is completely determined by the electronic coupling J, the reorganization energy λ and the energy difference ΔE. For a electron transfer from an initially charged molecule A to an uncharged molecule B inside a generated atomistic structure, these parameters can be calculated with the aforementioned QuantumPatch method. The energy difference $\Delta E = E_B - E_A$ is given by the HOMO energies (hole transport) or LUMO energies (electron transport) of molecules A and B, including polarization energy contributions due to their environment. Both are estimated by the energy eigenvalue of the highest occupied or lowest unoccupied Kohn-Sham orbital obtained by the DFT calculation of molecule A or B. The reorganization energy λ is calculated by the approach described by Stehr *et al.* [104]:

$$\lambda = (E_c^* - E_c) + (E_0^* - E_0) \tag{4.17}$$

where E_0 and E_c are the energies of the neutral and charged molecules in their lowest energy geometry, E_0^* is the energy of a neutral molecule in the lowest energy geometry of the charged state and E_c^* is the energy of a charged molecule in the lowest energy geometry of the neutral state. This is done by calculating all four energies for a given molecule in vacuum. Since in this

thesis all relevant structures consist only of one type of molecule, λ is the same for each dimer pair AB inside one structure. For the electronic coupling the calculation method described in [104] (based on [105]) was used:

$$J_{ij} = \frac{H_{ij} - 0.5\,(H_{ii} + H_{jj})\,S_{ij}}{1 - S_{ij}^2} \tag{4.18}$$

with

$$H_{ij} = \left\langle \varphi_i \middle| \hat{H}_{\text{KS}} \middle| \varphi_j \right\rangle$$
$$S_{ij} = \langle \varphi_i | \varphi_j \rangle$$

where φ_i and φ_j are the HOMO (or LUMO) orbitals of the two monomers in the dimer pair and $\hat{H}_{\text{KS}}$ is the Kohn-Sham Hamiltonian of the dimer system. S_{ij} is the overlap between the HOMO (or LUMO) orbitals and H_{ii} and H_{jj} are the monomer site energies. After calculating all these properties for a given film, they are used as input parameters to perform a kinetic Monte-Carlo (kMC) simulation of the hopping transport in a organic thin film. All kMC calculations referred to in this work, were performed by my colleague Simon Kaiser using LightForge[5] .

[5]LightForge is developed and distributed by Nanomatch (`https://www.nanomatch.com/`). A more detailed description of the workflow can be found under `http://docs.nanomatch.de/nanomatch-modules/LightForge/LightForge.html` (accessed on the 20.12.2021)

5 Structure simulation of pure films

In this chapter, the aforementioned algorithms to simulate physical vapor deposition of small molecules (see section 4.1), are evaluated using four commonly studied organic semiconductors: 2,9-Dimethyl-4,7-diphenyl-1,10-phenanthroline (BCP) and 4,7-Diphenyl-1,10-phenanthroline (BPhen), which are typically used in the electron transport or hole blocking layer of an OLED as well as N,N'-Di(1-naphthyl)-N,N'-diphenyl-(1,1'-biphenyl)-4,4'-diamine (NPB) and 4,4'-Bis(N-carbazolyl)-1,1'-biphenyl (CBP), which mostly serve as hole transport and host material respectively. Furthermore, roughly two monolayers of Buckminsterfullerene (C_{60}) were used as a substrate in all simulations. The chemical structures of all five molecules are depicted in fig. 5.1. In section 5.1 the influence of the number of steps per deposition is used to find a set of simulation parameters which produces sensible structures. The described methods are then used to create pure thin films of the aforementioned organic semiconductor materials. Their molecular packing is analyzed and the density compared to experimental literature values. These results are presented in section 5.2. In section 5.3 the orientation of molecular fragments is calculated and the total molecular orientation related to refractive index measurements by Salehi et al. [106]. Finally, in section 5.4, the field dependent hole and electron mobility is calculated and compared to experimentally determined curves from literature.

The results presented in this chapter were published in [107].

5.1 Simulation parameters

After choosing GROMOS 54A7 as the force field and $T = 300\,\mathrm{K}$ as the temperature for both simulation approaches, the only open parameters are the

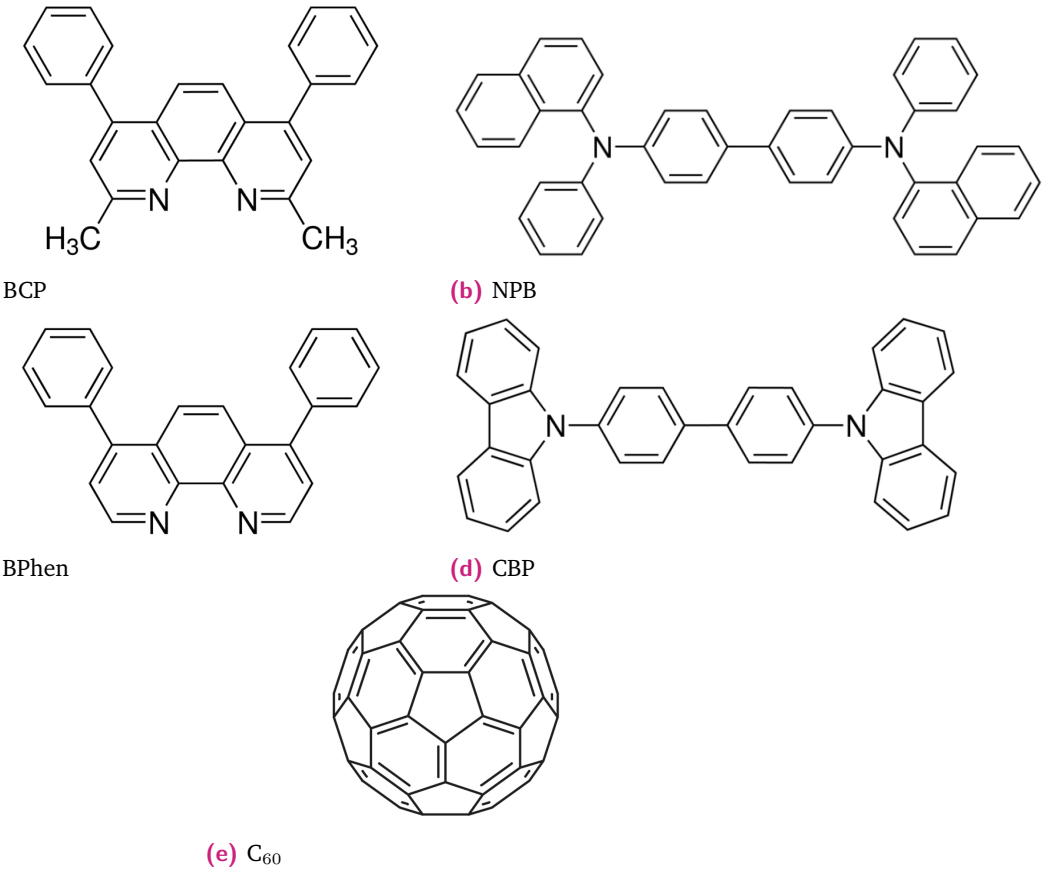

(a) BCP (b) NPB

(c) BPhen (d) CBP

(e) C_{60}

Fig. 5.1.: Chemical structures of 2,9-Dimethyl-4,7-diphenyl-1,10-phenanthroline (BCP), N,N'-Di(1-naphthyl)-N,N'-diphenyl-(1,1'-biphenyl)-4,4'-diamine (NPB), 4,7-Diphenyl-1,10-phenanthroline (BPhen), 4,4'-Bis(N-carbazolyl)-1,1'-biphenyl (CBP) and Buckminsterfulleren (C_{60}).

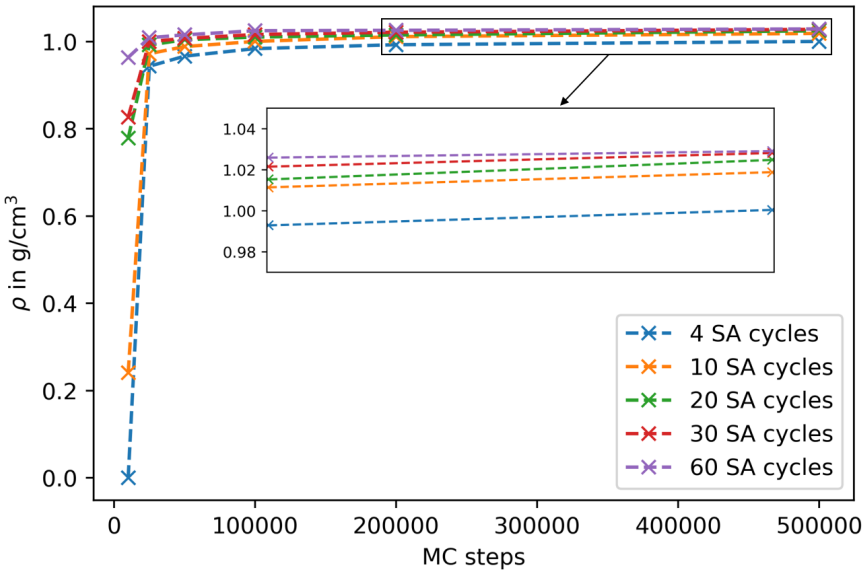

(a) Density of simulated BCP films with the MC approach for different numbers of MC steps and SA cycles per deposition cycle.

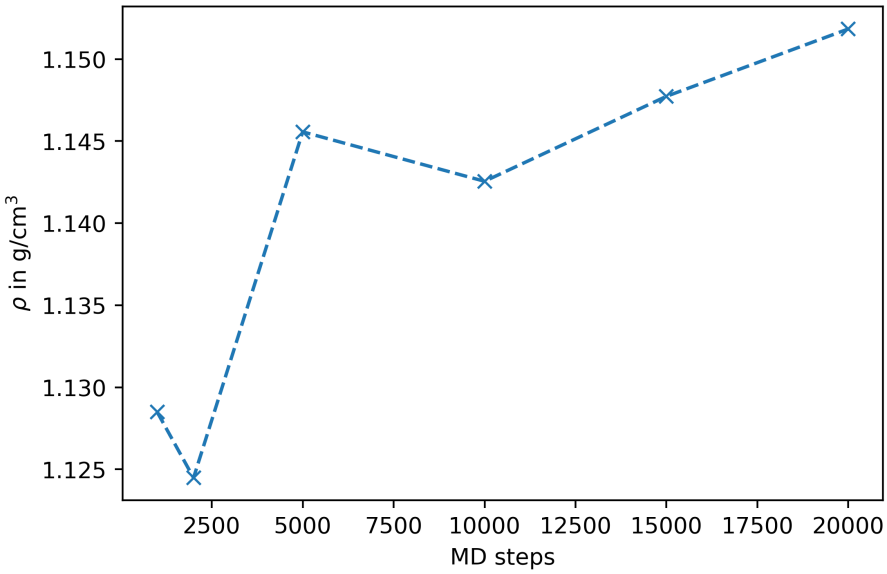

(b) Density of simulated BCP films with the MD approach for different numbers of MD steps per deposition cycle.

Fig. 5.2.: Influence of different simulation parameters on the thin film density.

number of MC steps and simulated annealing cycles for the MC approach and the number of steps per deposition in the MD approach. In this section the influence of both parameters on the final film density is checked for BCP, which served as a test candidate. The results are shown in fig. 5.2. For the MC approach, a combination of 200000 MC steps and 30 SA cycles is chosen, since no significant change in density was seen by increasing either of the two. For the MD approach, the final density was not converged even for the highest setting of 20000 MD steps per deposition cycle. Here 20000 steps was chosen as the default setting for further calculation in order to keep the overall simulation time manageable.

5.2 Molecular packing in organic films

The molecular packing is analyzed by first calculating the average mass density of every film according to the method presented in section 4.2.1. The final value for the material, given by the mean value of the 10 independent films, is then compared to experimental values. Additionally the radial distribution is calculated and compared between both methods.

5.2.1 Density

The results of the density calculations are depicted in fig. 5.3. It is seen that for all materials the density of the films generated by the MC approach is smaller (around approximately 10%) than the density of the MD films. When comparing to experimental results, the MD results are much closer, reaching perfect agreement for CBP aswell as a small underestimation for BPhen and NPB and a small overestimation for BCP. Interestingly the biggest experimentally difference is found between BCP and BPhen, which only differ through the substitution of two hydrogen atoms with two methyl groups. The higher density of BPhen is also found by both simulation approaches but the quantitative difference is underestimated. This could be a sign that there is a collective movement or partial crystallization effect during the formation of the BPhen film, which can not be captured by either of the presented simulations.

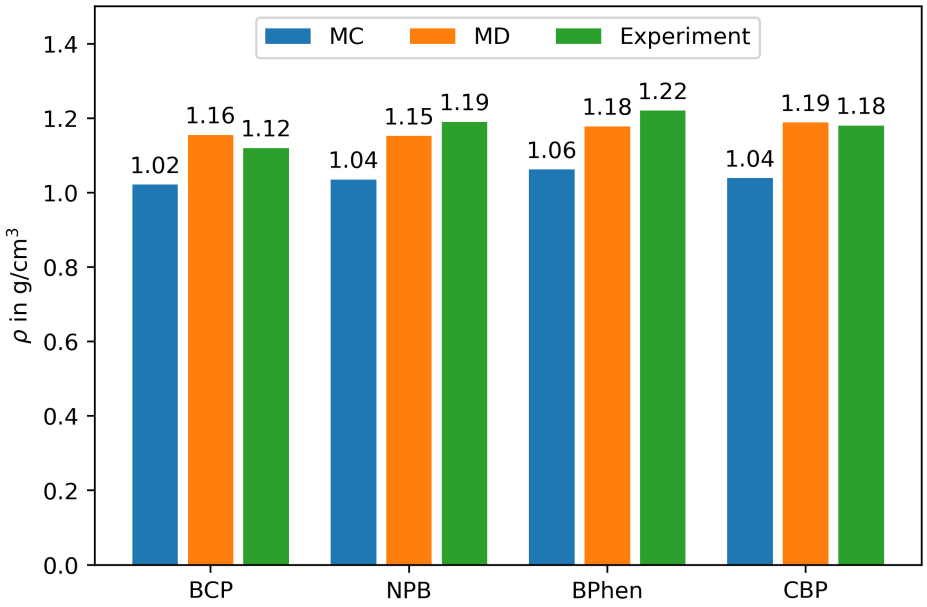

Fig. 5.3.: Densities of BCP, NPB, BPhen and CBP. In green are the measured values by **xiang_method_2007**, in orange the values from the MD approach and in blue the values obtained by the MC protocol. Each simulated value is a mean value of 10 independent simulations, the standard deviation was below 0.003 g/cm^3. The experimental uncertainty is 0.01 g/cm^3. Reprinted with permission from [107]

In general, the total density of a film can be attributed to two main factors: First, the local packing of the molecules and second, long range packing due to reformation processes of the film as new molecules are deposited. The first factor is mainly determined by the molecular shape and flexibility and can be captured by both MC and MD, although in MD the molecules are slightly more flexible due to the freezing of bonds and bondangles in the MC method. In these simulations, this manifests as a smaller minimum distance between the centers of mass of two adjacent molecules for NPB and CBP, where the flexible biphenyl core is able to bend in the MD approach. For BCP and BPhen, these smaller minimum distances are not observed due to the much stiffer phenanthrolin core (see fig. 5.4).

5.2.2 Radial distribution function

The RDF was calculated according to the method described in section 4.2.2, with an inner height $h_{\text{inner}} = 2\,\text{nm}$ and a cutoff radius $r_{\text{cutoff}} = 2.5\,\text{nm}$. The results for all four materials are plotted in fig. 5.5, each curve being averaged over the ten separate simulations. First of all a clear convergence to $g(\mathbf{r}) = 1$ for $r > 2\,\text{nm}$ is observed for all materials, confirming that indeed an amorphous structure was generated. When comparing the MD to the MC curve, the onset is the same for BCP and BPhen while for NPB and CBP the onset of the MD curve is about 1 Å earlier. This can be explained by the better local packing due to bending discussed above (see fig. 5.4). Furthermore a small peak at around 5 Å is observed for the MC structures of BCP, which is much less prominent in the MD structure. This peak could be a first indicator that there is a higher ordering of molecules in the MC structure. For BPhen this peak is slightly smaller but clearly visible in both MC and MD structures. Overall, all curves differ mostly in the region between 6 and 15 Å, which most likely stems from a qualitatively different packing in both methods. This is further investigated in the following two sections.

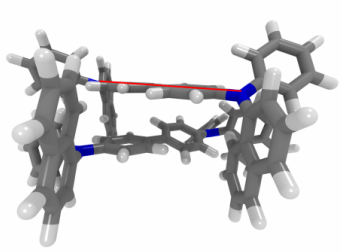

(a) Minimal distance pair of BCP (MC approach)

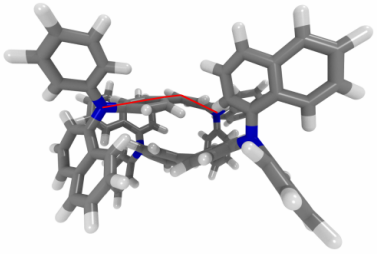

(b) Minimal distance pair of BCP (MD approach)

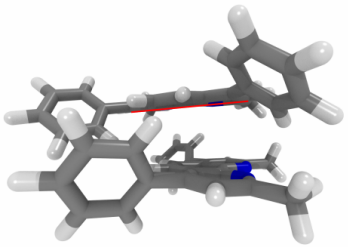

(c) Minimal distance pair of NPB (MC approach)

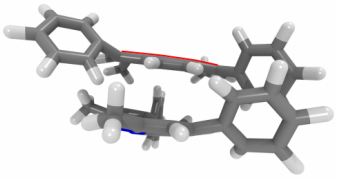

(d) Minimal distance pair of NPB (MD approach)

Fig. 5.4.: Minimal center of mass distance snapshots for NPB (a) and (b) aswell as BCP (c) and (d). The bending of the molecular axis through the biphenyl core of NPB and phenanthrolin core of BCP is highlighted in red. The flexible core of NPB enables a better local packing in the MD approach vs. the MC approach, while for BCP no difference is observed. Reprinted with permission from [107]

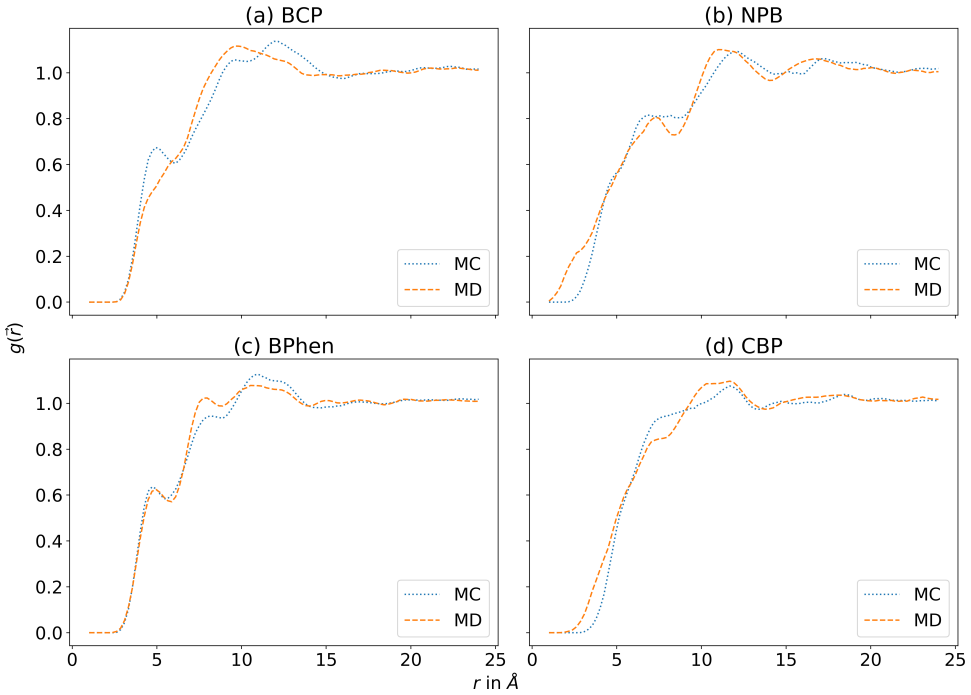

Fig. 5.5.: Radial distribution functions for BCP (a), BPhen (b), CBP(c) and NPB (d). Normal lines correspond to structures generated by the MC protocol, dashed lines to the MD approach. Reprinted with permission from [107]

5.3 Molecular orientation in organic films

In this section the ordering of molecules inside the final films is analyzed. At first the orientation parameter for molecular fragments is calculated according to the method described in section 4.2.3, then the ordinary and extra-ordinary refractive index is compared to experimental literature values.

5.3.1 Dihedral fragments

In fig. 5.6 the orientation histograms for the core fragments of BCP, BPhen, CBP and NPB are plotted. Here, the core fragment of BCP and BPhen is the phenanthrolin fragment highlighted red in the inset picture. For NPB and CBP the core consists of two phenyl ring fragments each, the calculated orientation parameter here is taken as the average of both individual phenyl ring orientations. Similar histograms for all other dihedral fragments can be found in figures A.1-A.4 in the appendix.

Looking at only these two core fragments, a clear qualitative difference between MD and MC structures is seen. The MC structures show an anisotropic distribution for all materials except NPB, where this effect is much smaller and the distribution is closer to the respective distribution in the MD case. The anisotropic distributions have a maximum at $\cos^2(\theta_z) = 1$ meaning that most fragment planes are aligned perpendicular to the deposition axis. For MD the orientation distribution is close to an isotropic distribution for all materials. Only a small deviation, with higher values at $\cos^2(\theta_z) = 1$ and lower values at $\cos^2(\theta_z) = 0$, from the isotropic curve is visible and is strongest for the CBP films. These results clearly show that the different simulation approaches can lead to fundamentally differently packed structures.

5.3.2 Refractive index

To see how the different packing observed in section 5.2.2 and section 5.3.1 influences macroscopic properties of the film, ordinary and extra-ordinary refractive indices are calculated for each structure. The values are furthermore compared to experimental values from [106]. The refractive index is calculated

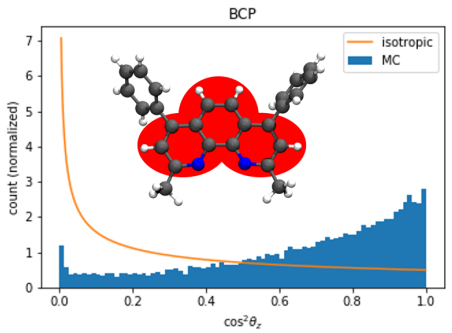

(a) BCP structures with MC

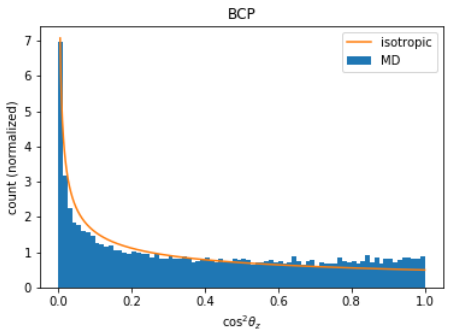

(b) BCP structures with MD

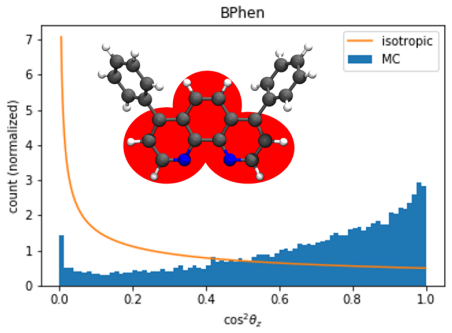

(c) BPhen structures with MC

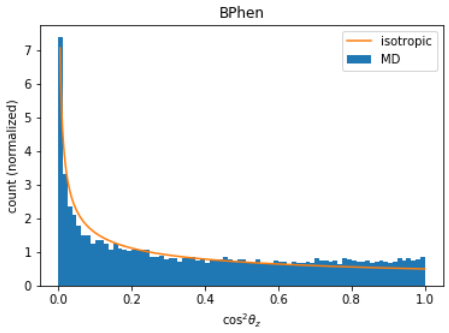

(d) BPhen structures with MD

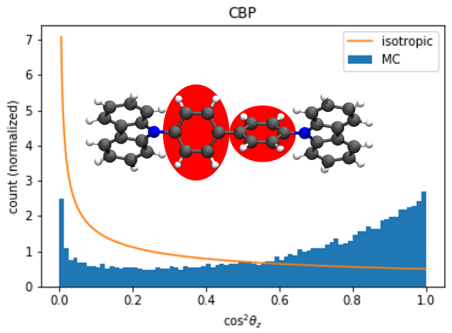

(e) CBP structures with MC

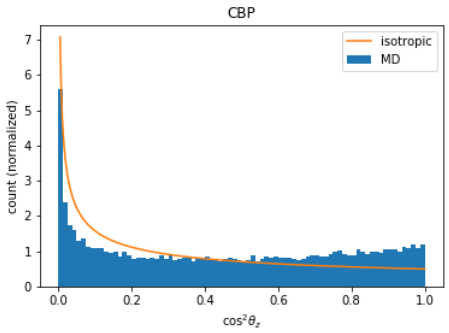

(f) CBP structures with MD

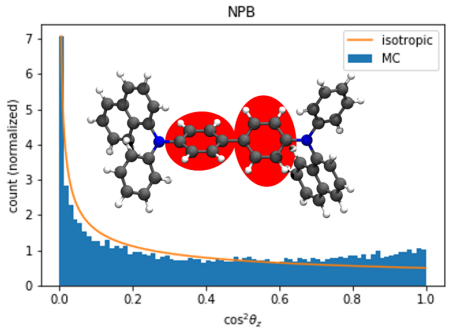

(g) NPB structures with MC

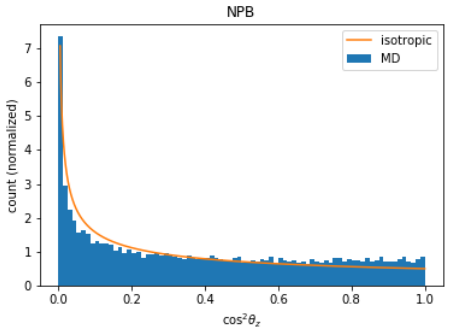

(h) NPB structures with MD

Fig. 5.6.: Histograms of the order parameter $cos^2\theta_z$ for the core fragments of BCP, BPhen, CBP and NPB. The core fragments are highlighted red in the inset. The yellow line corresponds to an ideal isotropic distribution.

Tab. 5.1.: Calculated ordinary n_o and extra-ordinary n_{eo} and their difference $\Delta n = n_o - n_{eo}$. The experimental values were obtained from ellipsometry measurements by [106]. All simulated values are a mean value over the 10 different structures per material and method with a statistical uncertainty of below 0.01.

Molecule	MC			MD			Experiment		
	n_o	n_eo	Δn	n_o	n_eo	Δn	n_o	n_eo	Δn
BCP	1.66	1.56	0.10	1.62	1.60	0.02	1.71	1.71	0.00
NPB	1.70	1.64	0.06	1.68	1.66	0.02	1.87	1.87	0.00
BPhen	1.72	1.60	0.12	1.68	1.66	0.02	1.73	1.73	0.00
CBP	1.72	1.58	0.14	1.68	1.62	0.06	1.80	1.74	0.06

using a *Clausius-Mossotti* type equation (see section 4.3.1), where the cutout radius a was taken as $3\,\mathrm{nm}$. To further remove the influence of the different mass densities on the absolute value of ϵ, the volume a^3 was adjusted by the correction factor $\rho^{\text{Simulation}}/\rho^{\text{Experiment}}$ using the values from section 5.2.1. The values of α_u were calculated using the Thole model (see section 2.3.2) at $\lambda = 550\,\mathrm{nm}$ for all atoms contained in the cutout sphere, effectively treating the whole sphere as one big molecule. From the resulting polarizability tensor α, the ordinary component was defined as $\alpha_o = \frac{\alpha_{xx}+\alpha_{yy}}{2}$ and the extra-ordinary as $\alpha_{eo} = \alpha_{zz}$. Based on $\epsilon = n^2$, the final ordinary and extra-ordinary refractive indices were calculated and are listed in table 5.1. Overall, all films show an anisotropy, which is stronger for the films generated by MC for all materials. Compared to the experimental values, the absolute values are underestimated for all films, which can most likely be attributed to a systematical underestimation of the polarizability tensor in the Thole approach. Furthermore, the anisotropy of the MD films matches the experimental behaviour better than the MC films. While the small Δn of 0.02 for BCP, NPB and BPhen could be due to a false simulation, it could also be a too small anisotropy to resolve in experiment (for example in [106] out of over 30 organic materials, none showed a value of Δn below 0.03). The observed higher anisotropy in the MC films matches with the observed orientation distributions from the previous section. Due to the delocalisation of electrons inside of the conjugated ring fragments, the polarizability inside the plane is higher than perpendicular to the plane, which in turn leads to a higher ordinary refractive index when the majority of conjugated fragments lie parallel to the film plane.

Tab. 5.2.: Results of the QuantumPatch calculations: intrinsic disorder σ_i and total disorder σ. For the electron transport materials BPhen and BCP all values correspond to the LUMO levels, for the hole transport materials NPB and CBP to the HOMO levels.

Molecule	MC		MD	
	σ_i [meV]	σ [meV]	σ_i [meV]	σ [meV]
BCP	40.2 ± 2.4	115 ± 5.0	45.5 ± 2.0	97 ± 5.4
NPB	79.6 ± 3.7	108 ± 5.4	74.9 ± 4.7	110 ± 6.0
BPhen	30.1 ± 1.9	122 ± 8.2	42.6 ± 2.5	108 ± 7.0
CBP	15.1 ± 0.6	90 ± 2.8	26.7 ± 2.3	88 ± 6.4

5.4 Mobility calculations

In this section, the electronic structure and field dependent mobility are calculated and compared to experimental data from literature. First, the on-site energies and electronic couplings J are calculated, which determine the transport properties in bulk organic semiconductors (see eq. (4.16)). For this, the HOMO and LUMO energy levels for 200 core molecules in the center of the film are calculated with the QuantumPatch method using the B3-LYP [36] functional and a def2-SVP [108] basis set (see section 4.3.3). The energy disorder $\sigma_{h/e}$ can then be extracted from the width of the HOMO and LUMO energy distributions. For the electronic couplings, the hopping-matrix elements for dimers of charged-uncharged-pairs of 150 core molecules and their neighbours with an atom-atom-cutoff of 7 Å are calculated. In table 5.2, the calculated values for the intrinsic and total disorder are given, where each value is the mean value of five independent structure samples. To good approximation, the total disorder is given by

$$\sigma^2 = \sigma_i^2 + \sigma_p^2 \tag{5.1}$$

where σ_i^2 is the intrinsic disorder stemming from the distortion of the molecules upon deposition and σ_p^2 is the disorder stemming from the polarization effects. Therefore, the first is a measure of the conformational disorder of the molecules in the film. We see that the results for σ_i as well as σ match for NPB when comparing MC to MD structures, while for BCP, BPhen and CBP a slightly higher intrinsic disorder is found for the MD structures. These higher intrinsic disorders are most likely explained by the initial degrees of freedom available in the MD simulation. When looking at the total disorder of these materials, a

significantly lower value is observed for the MD films of BCP and BPhen. For CBP both approaches produce a similar value. This means that the polarization contribution σ_p^2 of the molecular environment to σ is smaller for the MD films of BCP, BPhen and CBP. When looking at the results of the refractive index calculation, we see that for each of these materials the anisotropy Δn was heavily overestimated, suggesting a correlation between high anisotropy of the refractive index and polarization contribution of the energetic disorder.

Next the charge transport in these structures is simulated with the kinetic Monte-Carlo (kMC) charge transport model Lightforge (see section 4.3.4)). For this, the simulated structures are expanded into $40 \times 40 \times 40$ nm structures with periodic boundary conditions in x-, y- and z-direction according to the stochastic expansion method presented in [109]. Initially 20 charge carriers are placed into each system, which results in a charge density of approx $3.125\mathrm{e}{-3}$ per site. The carrier mobility is then extracted at four different field strengths: $\sqrt{E} = 300, 400, 500$ and $600\ \sqrt{\mathrm{V/cm}}$. Convergence is reached if the current density is constant over two thirds of the simulation. For BCP and BPhen the electron mobilities were calculating based on the LUMO values from table 5.2, and for CBP and NPB the hole mobilities based on the HOMO values respectively. The resulting field dependent mobilities are plotted in fig. 5.7. An one order-of-magnitude agreement of the mobility data is found for all MD films and all MC films except BPhen, where the the error is slightly higher. Interestingly the MC seems to capture the mobility of the BCP film perfectly, while for BPhen the MD film has a perfect agreement. In general the mobility is mostly determined by the total disorder σ of the individual film. The mean value of the electronic coupling elements are given in table 5.3. The average coupling matrix element $\langle J^2 r^2 \rangle$ is twice as high for the MD film of NPB compared to the MC film, this difference however seems to be completely offset by a just 2 meV higher electronic disorder of the MD film. This underlines the importance of correctly capturing this value when producing correct results. This is furthermore supported by the results obtained in [114] where the zero field mobility μ_0 follows the relation:

$$\mu_0 \propto \left\langle J^2 r^2 \right\rangle \exp\left(-0.25\,(\beta\sigma)^2\right) \tag{5.2}$$

where $\beta = k_\mathrm{B}^{-1} T^{-1}$.

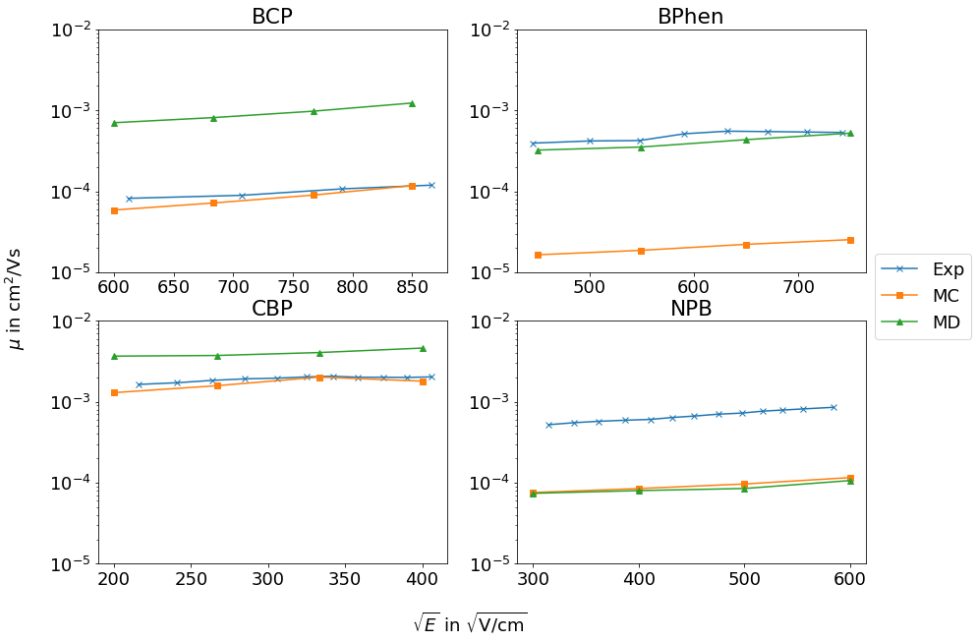

Fig. 5.7.: Field dependent electron mobilities for BCP and BPhen and hole mobilities for CBP and NPB calculated by the kMC model Lightforge [109]. Experimental values taken from [110] (BCP), [111] (BPhen), [112] (CBP) and [113] (NPB). Simulation errors are of the order of the symbol size. Reprinted with permission from [107]

Tab. 5.3.: Intermolecular hopping-matrix elements $\langle J^2 r^2 \rangle$, calculated for dimer pairs with the QuantumPatch approach. For the electron transport materials BPhen and BCP all values correspond to the LUMO levels, for the hole transport materials NPB and CBP to the HOMO levels.

Molecule	MC $\langle J^2 r^2 \rangle$ [eV^{2}Å^2]	MD $\langle J^2 r^2 \rangle$ [eV^{2}Å^2]
BCP	2.16e−3	2.41e−3
NPB	2.09e−3	4.48e−3
BPhen	2.76e−3	3.60e−3
CBP	5.74e−3	6.42e−3

6 Orientation effects in host-guest mixtures

In this chapter the optical and electronic orientation of molecules in host-guest mixtures is investigated. Section 6.1 introduces the studied guest and host materials. In section 6.2 the process of parametrization and structure generation is described. The generated structures are then analyzed with respect to their optical orientation in section 6.3 and their GSP slope in section 6.4.

The results presented in this chapter have been partially published in [115]. All 3-D images of molecules were rendered using the Visual Molecular Dynamics (VMD) [116] software.

6.1 Guest and host materials

The investigated emitter molecules are the N-heterocyclic carbene complex tris(N-dibenzofuranyl-N'-methylimidazole)iridium-(III) ($Ir(dbfmi)_3$) and its derivatives A-1 to A-5 and B-1 to B-3. All derivatives share the same $Ir(dbfmi)_3$ core with additions made to either the shorter (imidazol-) side of the ligand (A-X) or the longer (dibenzofuranyl-) side of the ligand (B-X) (see fig. 6.1). The *mer* isomer of all molecules, aswell as the *fac* isomer of $Ir(dbfmi)_3$, A-1 and A-5, were co-deposited with the host material bis[2-(diphenylphosphino)phenyl]ether oxide (DPEPO) (see fig. 6.2) at a volume ratio of approximately 8%. All experimental data referenced in this chapter is taken from the measurements published in [115].

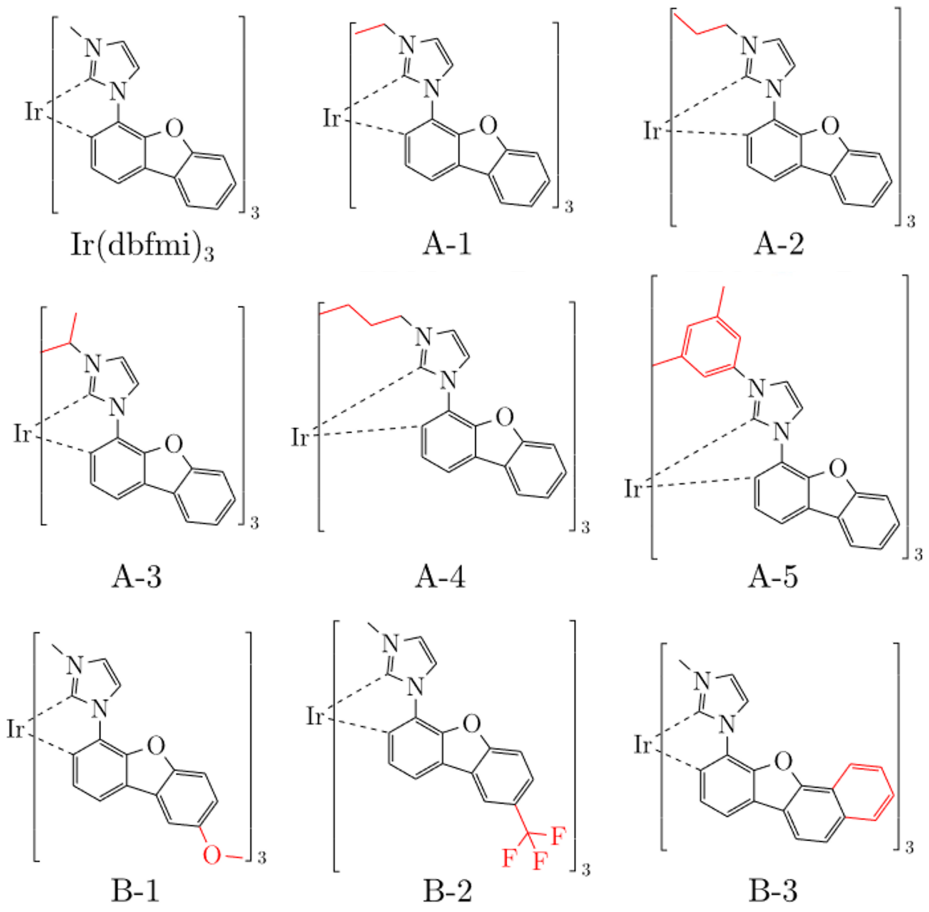

Fig. 6.1.: Chemical structures of the N-heterocyclic carbene complex tris(N-dibenzofuranyl-N'-methylimidazole)iridium-(III) ($Ir(dbfmi)_3$) and its derivatives. Individual additions are highlighted in red.

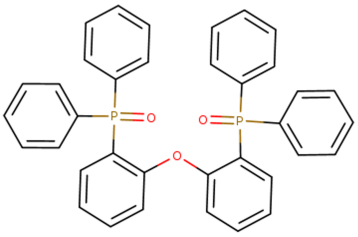

Fig. 6.2.: Chemical structure of bis[2-(diphenylphosphino)phenyl]ether oxide (DPEPO).

6.2 Deposition simulation

As in chapter 5, the atomistic structures were generated using the MC and MD deposition approaches introduced in chapter 4. In contrast to the simulations from the previous chapter, the OPLS [52] force field parameters are used for both simulations. In the OPLS forcefield several atom types can be used to parametrize a molecule, these types were first assigned by hand for every atom and the MD forcefield was built using the Moltemplate[1] tool [117]. Additionally partial charges were calculated using a fit of the eletrostatic potential (as described in [101]) of a DFT calculation with a def2-SVP basis set [108] and B3-LYP [36] as the exchange correlation functional using Turbomole 7.2 [118]. Since iridium is not covered by the OPLS force field, the internal degrees of freedom (bond, angle and dihedral, see fig. 2.2) could not be parameterized by the OPLS forcefield. The emitter molecules were therefore kept completely rigid in the MD simulation using the *fix/rigid/small* command as implemented in LAMMPS [86], which uses the algorithm published by Kamberaj et al. [119] in 2005. For the Lennard Jones interactions of iridium, the parameters from the Universal force field (UFF) derived by Rappé et al. [120] were used. For the MC deposition, the intramolecular dihedral force field was additionally parameterized by turning each dihedral angle in 20 degree steps and evaluating the energy with DFT, again using a def2-SVP basis set combined with the B3-LYP functional in Turbomole. To prevent clashes between the rotated fragments, all other dihedral angles were relaxed after each step using a force field of internal partial charges and internal Lennard Jones parameters, which was fitted iteratively. This was done using the DihedralParametrizer module provided by Nanomatch[2] (a more detailed description can be found in their documentation[3]).

After the parameterization of the forcefields, the simulation was started using the following settings for the MC deposition (see section 4.1.2) simulations:

- Number of deposited molecules: 2000

[1] Moltemplate: A Tool for Coarse-Grained Modeling of Complex Biological Matter and Soft Condensed Matter Physics, available on `https://www.moltemplate.org`

[2] Commercially available on `https://nanomatch.com/`. Last accessed on the 09. October 2021.

[3] `http://docs.nanomatch.de/nanomatch-modules/DihedralParametrizer/DihedralParametrizer.html`. Last accessed on the 09. October 2021.

- Number of MC steps: 300000
- Number of SA cycles: 30

And the following settings for the MD deposition (see section 4.1.1) simulations:

- Number of deposited molecules: 1000
- Number of MD steps per deposition cycle: 20000

For the experimental data published in [115], the emitter-host systems were deposited at a volume fraction of approximately 8 $\%\mathrm{vol}$. This value has to be converted into a molecular fraction ($\chi\,[\%\mathrm{mol}]$) as an input value for the deposition simulations, where every new molecule inserted into the simulation is drawn randomly based on these molecular fractions. To that end, the molar volume V_m of all molecules is estimated by calculating the mass density of pure films. Together with the molar mass M of a molecule, the estimated molar volume is given by:

$$V_m = \frac{M}{\rho} \tag{6.1}$$

With this the molecular concentration of guest G in host H is:

$$\chi\,[\%\mathrm{mol}] = \frac{V_m^{\mathrm{G}}}{V_m^{\mathrm{H}}}\chi\,[\%\mathrm{vol}] \tag{6.2}$$

To estimate the mass density, pure films containing 1000 molecules were generated by the MC deposition approach for each material, using the same set of settings as mentioned above. The densities were extracted using the method described in section 4.2.1. The calculated densities and resulting molecular fractions are listed in table 6.1

6.3 Analysis of the optical orientation parameter

As already mentioned in section 3.2 the optical orientation of emitters is an important factor for the external quantum efficiency (EQE) and therefore plays a large role in the improvement process of modern OLEDs: Besides wasting

Tab. 6.1.: Estimation of molecular deposition fractions in the host material DPEPO corresponding to 8% volume concentration, based on simulated pure film mass densities.

Material	ρ [g/cm^3]	χ^{DPEPO} [%mol]
DPEPO	1.08	-
mer-Ir(dbfmi)$_3$	1.25	5.6
fac-Ir(dbfmi)$_3$	1.22	5.5
mer-A-1	1.22	5.3
mer-A-1-fac	1.20	5.2
mer-A-2	1.19	4.9
mer-A-3	1.16	4.8
mer-A-4	1.16	4.6
mer-A-5	1.11	3.9
mer-A-5-fac	1.10	3.9
mer-B-1	1.18	4.9
mer-B-2	1.26	4.7
mer-B-3	1.15	4.5

less energy, more efficient OLEDs can be operated at lower current densities. This, in turn, reduces the part of device degradation which is due to ohmic losses, ultimately leading to a higher OLED lifetime [121].

It has already been shown, that the general trend of whether emitter molecules show a preferred orientation or not, can be reproduced with the MC based deposition protocol Deposit: In 2017 Friederich et al. investigated the mechanism behind the orientation of iridium based emitters molecules and found a good agreement to experimentally measured orientation parameters for the well known materials Ir(bppo)$_2$(acac), Ir(bppo)$_2$(ppy) and Ir(bppo)(ppy)$_2$ [122]. Based on this work the aim of this sections is to explore the viability of using molecular deposition simulations to predict changes in emitter orientation for a series of 12 similar homoleptic iridium carbene complexes.

6.3.1 Quantum chemical calculations

The order parameter Θ chosen for the following analysis of the optical orientation is defined as

$$\Theta = \frac{\sum_n \vec{\mu}_z^2}{\sum_n |\vec{\mu}|^2} \tag{6.3}$$

Tab. 6.2.: Transition energies of the first 10 excited states calculated with Dalton2018 on the optimized ground state geometry.

Molecule	Excited state transition energy [eV]									
	1	2	3	4	5	6	7	8	9	10
mer-Ir(dbfmi)$_3$	2.96	2.98	2.99	3.5	3.6	3.63	3.64	3.66	3.77	3.83
fac-Ir(dbfmi)$_3$	3.0	3.01	3.01	3.57	3.59	3.59	3.75	3.75	3.78	3.87
mer-A-1	2.96	2.99	3.0	3.49	3.61	3.63	3.64	3.66	3.79	3.82
fac-A-1	3.0	3.01	3.01	3.57	3.59	3.59	3.75	3.75	3.78	3.87
mer-A-2	2.97	2.99	3.0	3.49	3.61	3.62	3.63	3.65	3.79	3.81
mer-A-3	2.96	2.98	2.99	3.48	3.61	3.62	3.63	3.65	3.79	3.82
mer-A-4	2.96	2.99	2.99	3.48	3.61	3.62	3.63	3.65	3.79	3.81
mer-A-5	2.93	2.95	2.96	3.41	3.46	3.54	3.58	3.61	3.61	3.63
fac-A-5	2.99	2.99	2.99	3.5	3.53	3.54	3.65	3.66	3.67	3.67
mer-B-1	2.92	2.94	2.95	3.47	3.57	3.58	3.59	3.62	3.68	3.73
mer-B-2	2.94	2.96	2.97	3.45	3.59	3.61	3.61	3.63	3.69	3.73
mer-B-3	2.59	2.6	2.6	3.12	3.14	3.15	3.3	3.38	3.47	3.52

where the sum is over the n emissive molecules in a film with their corresponding transition dipole moment (TDM) $\vec{\mu}$. It is therefore necessary to calculate the TDMs for every emitter material. This was done by first optimising the structure of the S_0 ground ground state with DFT using the B3-LYP [36] exchange correlation functional combined with the ecp-sdd-DZ [123] basis set for iridium and the 3-21G [124] basis set for all other elements. All structure optimizations were done with Turbomole 7.2 [118]. Afterwards a TDDFT calculation for the first 10 excited triplet states is performed on the optimized ground state geometry using the effective charge approximation [125, 126, 127] for the spin–orbit operator in Dalton2018 [128][4]. The resulting excited state transition energies are printed in table 6.2. A clear separation of at least about $0.5\,\mathrm{eV}$ between the first three states and all higher states is observed. Additionally the first three transitions show only small differences of about $10\,\mathrm{meV}$ to $30\,\mathrm{meV}$, which is of the order of thermal fluctuations at room temperature. Each of the three transitions corresponds to an electron transfer to one of the ligands. To evaluate the quality of these calculations, the phosphorescent

[4]Dalton, a molecular electronic structure program, Release v2018.0 (2018), see http://daltonprogram.org

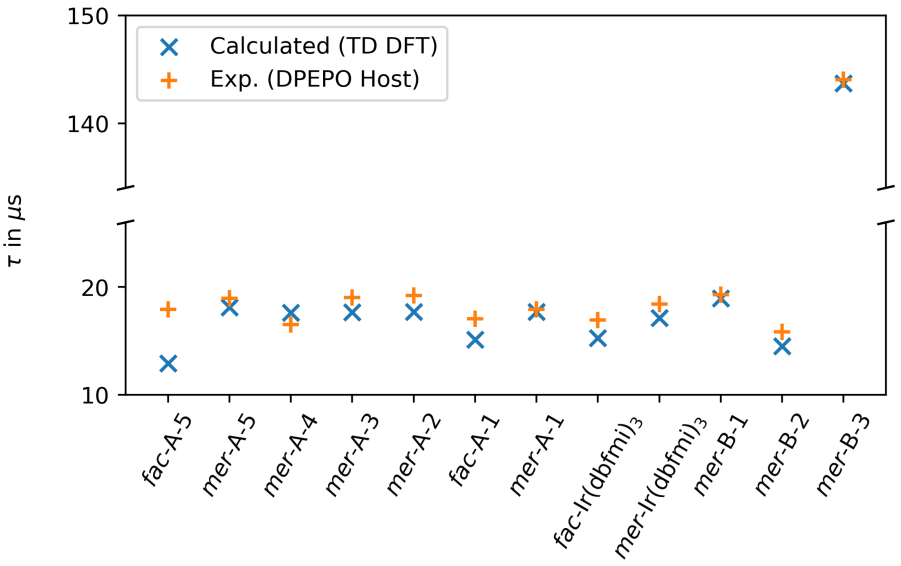

Fig. 6.3.: Calculated phosphorescence lifetime compared against experimental values from Schmid et al. [115]. Adapted and reprinted with permission from [115]. Copyright 2020 American Chemical Society.

lifetimes τ are calculated according to the formula published by Mori et al. [129]:

$$\tau = \frac{\sum_i e^{-\Delta E_i / k_{\mathrm{B}T}}}{\sum_i k_i e^{-\Delta E_i / k_{\mathrm{B}T}}} \tag{6.4}$$

where i sums over all transition substates, in this case a total of 30 substates exist, resulting from the calculated first 10 excited triplet states which each have 3 degenerate microstates. ΔE_i is the energy difference of the i-th substate to the first substate and k_i is the corrected radiative rate of the i-th substate as defined in [129]. The resulting values for τ are plotted together with the experimental values in fig. 6.3. A good agreement between calculated and experimental values can be found, most notably the almost a factor of 10 higher phosphorescence lifetime for *mer*-B-3 compared to the other emitters is also observed in the calculations. Subsequently, all emitter structures were optimized again, this time to the geometry of the first excited triplet state T1. Afterwards, the TDMs for the first excited state were calculated again in this T1 geometry, resulting in three TDM vectors corresponding to one of the three ligands. Under the approximation that also for the *mer* isomers the TDM

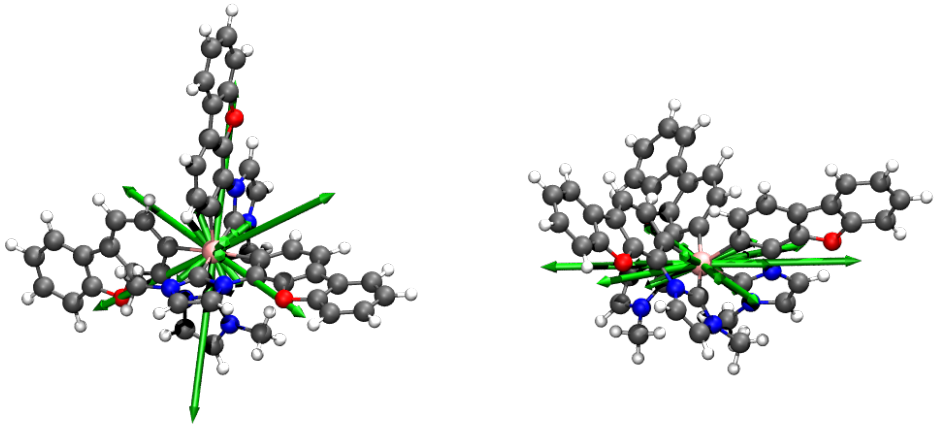

(a) *mer*-Ir(dbfmi)$_3$ **(b)** *fac*-Ir(dbfmi)$_3$

Fig. 6.4.: Visualized structures of (a) *mer*-Ir(dbfmi)$_3$ and (b) *fac*-Ir(dbfmi)$_3$. The calculated and mapped TDM and $-1\cdot$ TDM vectors are printed with the iridium atom as their origin.

sec1

vectors are symmetric with respect to the ligand orientation, all three vectors are mapped onto the remaining two ligands. This mapping is done by shifting the molecule so that the position of the iridium atom coincides with the origin and afterwards calculating the rotation matrix, which rotates the two Ir-N vectors of one ligand to the corresponding Ir-N vectors of another ligand. The TDM vectors are then rotated by the same rotation matrix, finally resulting in 9 separate TDMs per emitter molecule. The emitter molecules *mer*-Ir(dbfmi)$_3$ and *fac*-Ir(dbfmi)$_3$ with their calculated TDMs are visualized in fig. 6.4, similar pictures for the remaining emitter molecules can be found in the appendix (see fig. A.5).

6.3.2 Calculation of the orientation parameter

To calculate the orientation parameter of mixtures of the emitter materials with DPEPO as a host material, 5 structures were generated using the MC approach and 10 structures using the MD approach. Using the simulation settings provided in section 6.2 this yielded 10000 deposited molecules per emitter/host combination. The number of sampling points per emitter molecule however is only around 500, due to the low molecular deposition fractions

(see table 6.1). Since the emitter molecules are kept rigid (except the dihedral rotations of small groups added to the ligands in some derivatives), the TDMs calculated in the previous chapter can be mapped onto the simulated emitter geometries by a simple rotation. The orientation parameter for each of the 9 TDMs found is then calculated by averaging over all sampling points as shown in eq. (6.3). This would then results in a set of 9 different orientation parameters. However, not every transition is equally likely but rather depends on the square of the magnitude of the TDM (Fermi's golden rule) and also on the excitation energy itself. To account for both a weighted average of all the 9 orientation parameters was calculated using the following weights:

$$w_i = e^{-\Delta E_i / k_\mathrm{B} T} \, |\vec{\mu}_i|^2 \tag{6.5}$$

where ΔE_i is the energy difference between the transition energy of the $i-$th TDM $\vec{\mu}_i$ and the lowest transition energy. The so calculated weighted orientation parameters are plotted against the experimentally available results from [115] in fig. 6.5. Overall, a good agreement between experiment and both types of simulations can be found: both approaches clearly reproduce the better orientation of the *mer*-B-X derivates compared to the *fac*-A-5 and *mer*-A-5 isomers. Comparing each simulation method separately with the experimental data R^2-scores (coefficient of determination) of 0.76 (MC) and 0.69 (MD) were found, suggesting that the MC approach is slightly better suited for the prediction of emitter orientations. One possible explanation for this result could be that the MC protocoll better samples the orientation of the individual emitter molecules during deposition, while in the MD approach much computation time is used for the simulation of the substrate and possible collective movements. This hypothesis is supported by the findings in [115], where almost no change of the orientation parameter is measured when switching the host material from DPEPO to 3,6-bis(diphenylphosphoryl)-9-phenylcarbazole (PO9), which is another indicator that the emitter orientation depends more on the emitter material than on the host material.

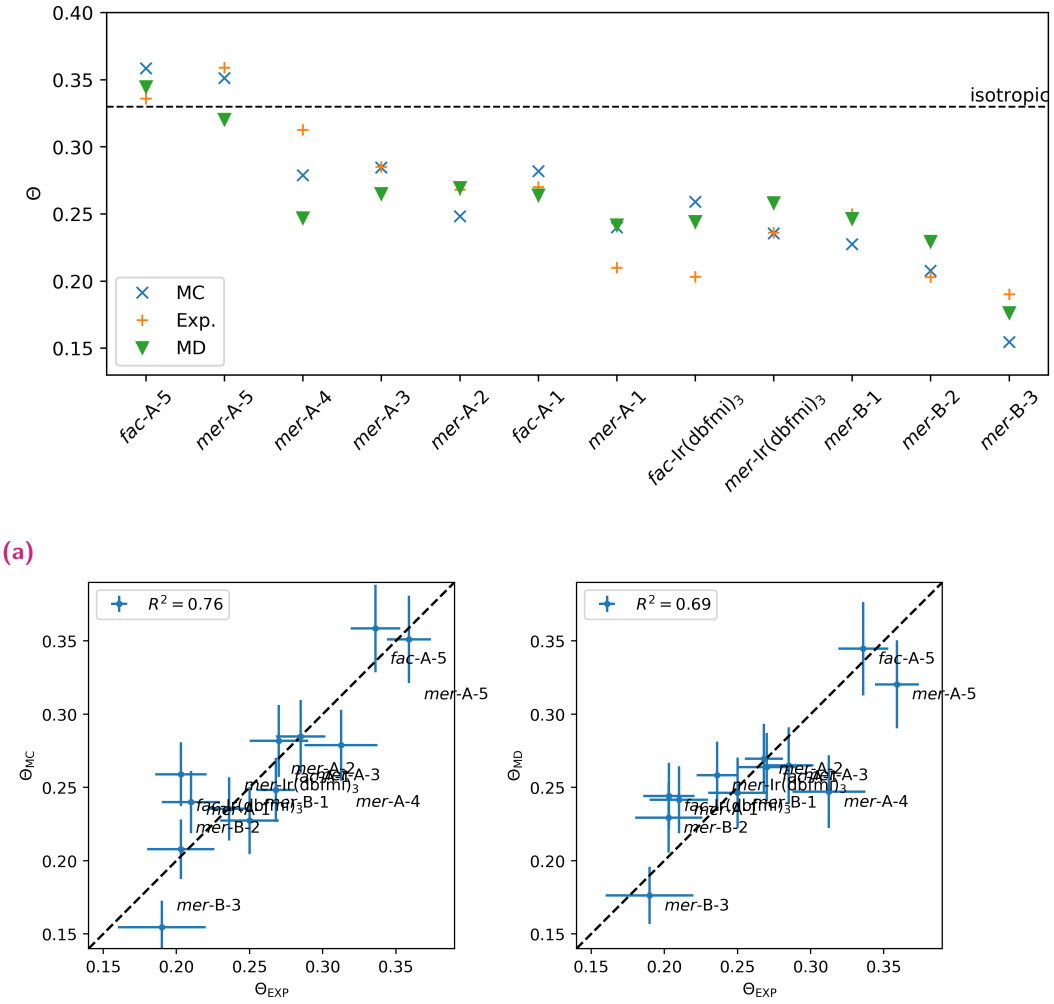

Fig. 6.5.: (a) Simulated and experimental orientation parameters of the N-heterocyclic carbene complex tris(N-dibenzofuranyl-N'-methylimidazole)iridium-(III) ($Ir(dbfmi)_3$) and several derivatives with DPEPO as host material. (b)/(c): Correlation between simulated orientation with MC/MD and experimental data.

6.4 Analysis of the GSP slope

As shown in eq. (4.15) the GSP of a thin film can be related to its average molecular dipole density $\frac{\langle p \rangle}{V}$, which is equal to the surface charge density σ_{if} accumilating at the film/vacuum and film/substrate interfaces. These surface charge densities have also been measured in [115] for pure DPEPO films as well as for mixtures of DPEPO with the emitter materials *mer*-Ir(dbfmi)$_3$, *fac*-Ir(dbfmi)$_3$, *fac*-A-5 and *mer*-B-2. In these measurements, a strong decrease of the surface charge density could be measured for the *fac*-Ir(dbfmi)$_3$ and *mer*-B-2 mixtures compared to the pure DPEPO films, while the *mer*-Ir(dbfmi)$_3$ mixtures showed only a slight decrease and the *fac*-A-5 mixtures an increase. In the publication, the non-zero GSP for the neat DPEPO film is explained by a small fraction of uncompensated permanent dipole moments (PDMs) in a film of mostly antiparallel oriented PDMs, leading to a net average dipole moment of the film. In the mixtures, this net dipole moment is either compensated by oppositely oriented dipole moments of the guest molecules leading to a decrease of the GSP or diluted by guest molecules leading to a higher fraction of uncompensated host dipole moments and therefore to an increase of the GSP. The aim of this section is to: (a) estimate again how well these experimental results are captured by simulated morphologies and (b) analyse the reason for a possibly higher or lower GSP on the molecular level in the simulation.

For the pure DPEPO films, the molcular volume V can be estimated by dividing the mass of one DPEPO molecule m_{DPEPO} by the density of the simulated film (see section 4.2.1). For the mixed films, an average mass of the molecules m_{mixed} is calculated by dividing the total mass of the film by the number of deposited molecules. The so calculated molecular volumes are then averaged over all simulated films and are listed in table 6.3.

6.4.1 Quantum chemical calculations

To calculate the molecular dipole moment for every molecule taking into account the polarization, the QuantumPatch method is used (see section 4.3.3). To remove the unphysical vacuum interface in x and y direction, the final structures were periodically extended by adding 8 copies in the xy-plane. This is possible due to the use of periodic boundary conditions along these axes

Tab. 6.3.: Calculated molecular volumes V based on the morphologies simulated by the MC and MD approach.

Material	$V^{\mathrm{MC}}\,[\mathrm{nm}^3]$	$V^{\mathrm{MD}}\,[\mathrm{nm}^3]$
DPEPO	0.90	0.79
mer-Ir(dbfmi)$_3$	0.91	0.81
fac-Ir(dbfmi)$_3$	0.92	0.81
fac-A-5	0.93	0.82
mer-B-2	0.92	0.81

during all deposition simulations. The molecular dipole moments are then calculated only for the inner molecules belonging to the initially deposited film, while the rest of the molecules are only used for the polarization part. A total of 7 iterations were used with Turbomole 7.2 [118] (def-SV(P) and B3-LYP) as the DFT engine in QuantumPatch.

6.4.2 Results

Combining the results from QuantumPatch with the molecular volumes from above, the surface charge density σ_{if} was calculated for every morphology and plotted together with the experimental data in fig. 6.6. Histograms of the calculated dipole moments are printed in the appendix (see fig. A.6 – fig. A.10). It is clearly visible that almost no GSP slope is found in the MD generated morphologies. For the MC structures, however, the absolute value of the GSP is close to the experimental values and more importantly the trend of an increase for the *fac*-A-5 mixtures and a decrease for the *mer*-B-2 and *fac*-Ir(dbfmi)$_3$ is reproduced. Since the emitter orientation results are much closer between MD and MC, the large deviation here most likely stems from the MD forcefield parametrisation used for the host material DPEPO, which is the main contributor to the total GSP of the film. To understand the reason behind increase or decrease of the GSP, it is helpful to look at the orientation of host and emitter molecules separately. Histograms of $\cos\theta$ (with θ being the angle between dipole moment and z-axis) are shown for the host material DPEPO in fig. 6.7 and for the emitter materials in fig. 6.8. A clear difference between MC and MD structures is seen for the orientation of DPEPO: all MC structures show a higher amount of dipole moments orientated towards the

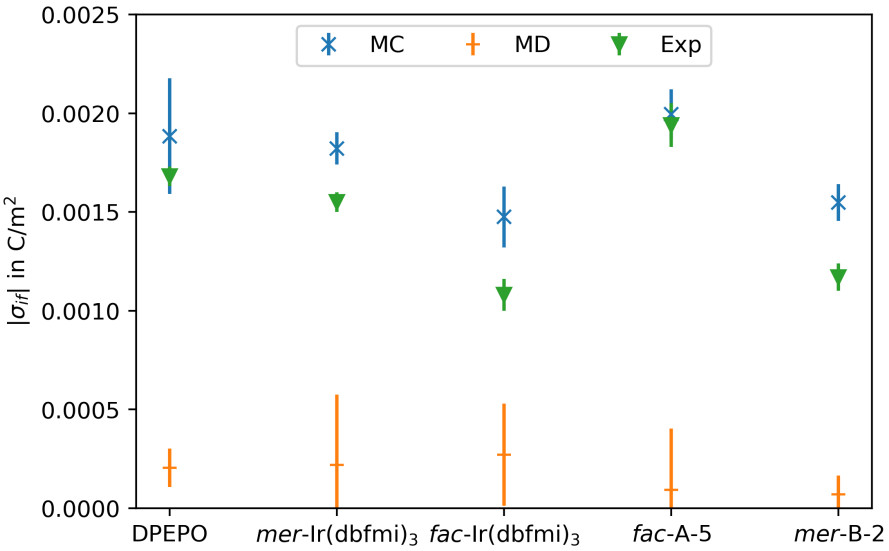

Fig. 6.6.: Surface charge densities of DPEPO, *mer*-Ir(dbfmi)$_3$, *fac*-Ir(dbfmi)$_3$, *fac*-A-5 and *mer*-B-2. In green are the measured values taken from [115], in orange the values from the MD approach and in blue the values obtained by the MC protocol. Each simulated value is a mean value of 5 (MC) or 10 (MD) independent films, the standard deviations are taken as the errorbars. Each film contained 2000 (MC) or 1000 (MD) molecules.

positive z-direction leading to a GSP. For the MD films such a trend is not seen, resulting in the almost zero GSP values calculated above. Furthermore, the increase or decrease of the GSP in mixture can cleary be attributed to the orientation of the respective emitter molecule. Looking at the MC structures, *fac*-Ir(dbfmi)$_3$ shows a strong tendency to orient its dipole moment towards the surface lowering the GSP, the same is true for *mer*-B-2 but to a lesser extent. *mer*-Ir(dbfmi)$_3$ and *fac*-A-5 show a more isotropic distribution, where *mer*-Ir(dbfmi)$_3$ leans to a slightly stronger ordering towards the surface and *fac*-A-5 to a stronger ordering away from the surface. For MD a similar behaviour can be observed with the biggest deviation being *fac*-Ir(dbfmi)$_3$, which shows a peak at both $\cos\theta = 1$ and -1. To understand why especially *fac*-Ir(dbfmi)$_3$ shows such a different distribution then the *fac*-A-5 derivative, a look at the orientation of the permanent dipole moment within the molecule is helpful (see plots in fig. A.11). For both of the *fac* isomers the dipole moment is parallel to the C_3 rotational axis of the molecule and points towards the methylimidazole side of the ligands. Upon deposition each molecule increases the surface area shared with the substrate, effectively maximizing the attractive part of the Lennard-Jones potential. Looking at the MD results, there seem to be two favorable positions for *fac*-Ir(dbfmi)$_3$: one with the methylimidazole side facing upward ($\cos\theta = 1$) and one with the methylimidazole side facing downward ($\cos\theta = -1$). In the MC results only the latter is visible. One explanation for this could be that the transition from an upward facing orientation to a downward facing one has to overcome a potential energy barrier, which is supported by the low number of sample points found at perpendicular orientation in both approaches. In general such barriers are more likely to be overcome in the Basin-hopping approch used in the MC simulations. For *fac*-A-5, the shape of the molecule gets more spherical through the addition of the xylene groups, leading to a lowering of this barrier and a more isotropic distribution in general. The dipole moment of the *mer* isomers is pointing towards the nitrogen atom of the ligand which is perpendicular to both other ligands. Due to its overall more flat geometric shape the *mer* isomers tend to lie down on two of their three ligands with the third one slightly tilting upward. This leads to an expected maximum of the orientation closer to $\cos\theta = 0$. In the simulations this is seen both for *mer*-Ir(dbfmi)$_3$ and *mer*-B-2, where the maximum of the histogram is at around $\cos\theta \approx -0.25$ in both methods. The tendency towards a downward facing dipole moment is higher for *mer*-B-2

than for *mer*-Ir(dbfmi)$_3$. This can be explained by considering the situation where both parallel ligands (meaning both dibenofuranyl sides of the ligands are on the same axis) are laying on the surface. In this case, it is easier to find a spot on the surface where the shorter methylimidazole side of the third ligand is pointing towards the surface instead of the longer dibenzofuranyl group. This asymmetry is then amplified by making this side even longer through the addition of the trifluoromethyl group in the *mer*-B-2 derivate. Combined with the results from the previous section and the overall similar orientation of the emitter molecules is predicted by both methods, where the MC approach shows a better agreement with experiment. Additionally, judging from the wrong prediction of the DPEPO dipole moments in both pure films and mixtures generated with the MD approach, DPEPO does not seem to be accurately described by the MD forcefield. This does however not influence the orientation of the emitter molecules, where the main driving force is the Lennard-Jones interaction and not the electrostatic interaction.

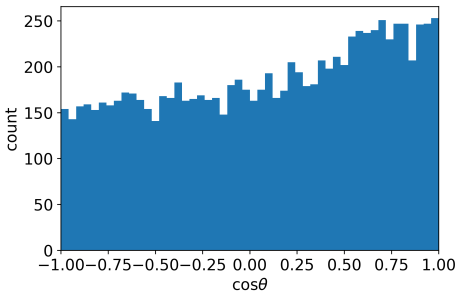

(a) Pure films simulated with MC.

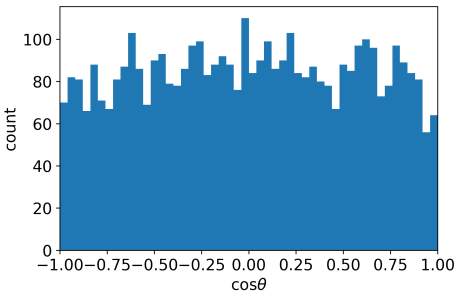

(b) Pure films simulated with MD.

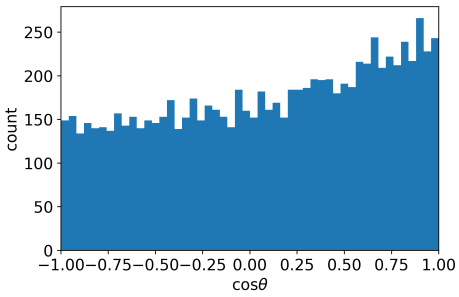

(c) *mer*-Ir(dbfmi)$_3$ mixtures simulated with MC.

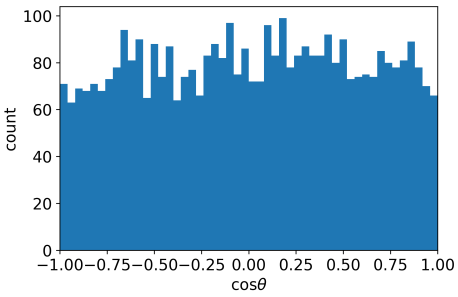

(d) *mer*-Ir(dbfmi)$_3$ mixtures simulated with MD.

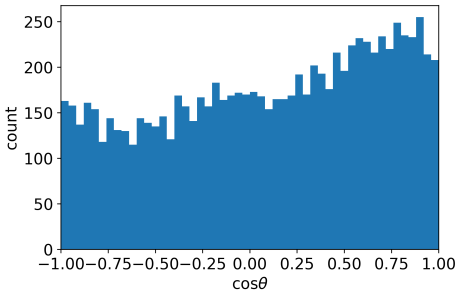

(e) *fac*-Ir(dbfmi)$_3$ mixtures simulated with MC.

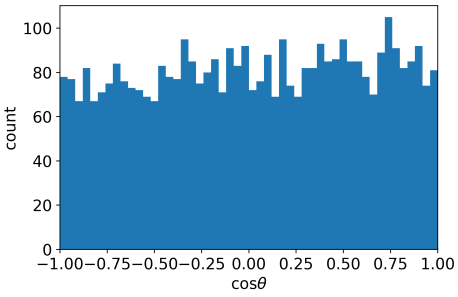

(f) *fac*-Ir(dbfmi)$_3$ mixtures simulated with MD.

Fig. 6.7.: Histograms of $\cos\theta$ (with θ being the angle between dipole moment and z-axis) of all DPEPO molecules deposited either in pure films or mixtures with the emitters *mer*-Ir(dbfmi)$_3$, *fac*-Ir(dbfmi)$_3$, *fac*-A-5 and *mer*-B-2.

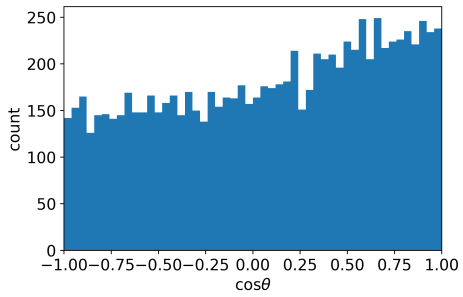

(g) A-5-*fac* mixtures simulated with MC.

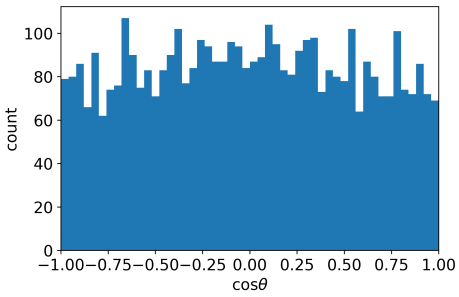

(h) A-5-*fac* mixtures simulated with MD.

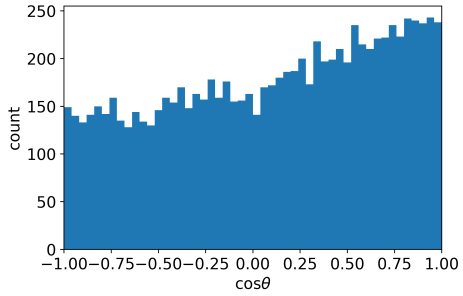

(i) B-2 mixtures simulated with MC.

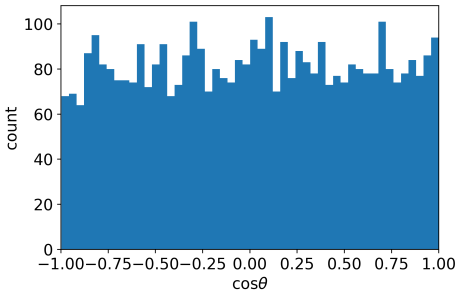

(j) B-2 mixtures simulated with MD.

Fig. 6.7.: Histograms of $\cos\theta$ (with θ being the angle between dipole moment and z-axis) of all DPEPO molecules deposited either in pure films or mixtures with the emitters *mer*-Ir(dbfmi)$_3$, *fac*-Ir(dbfmi)$_3$, *fac*-A-5 and *mer*-B-2.

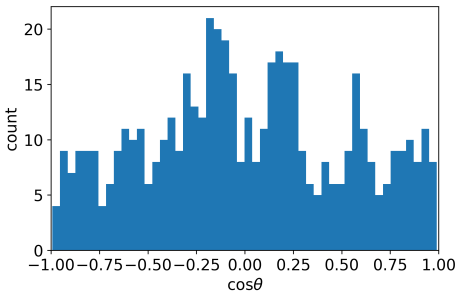

(a) *mer*-Ir(dbfmi)$_3$ mixtures simulated with MC.

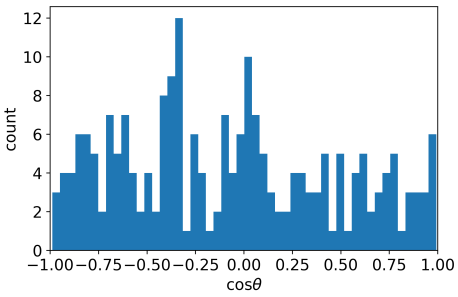

(b) *mer*-Ir(dbfmi)$_3$ mixtures simulated with MD.

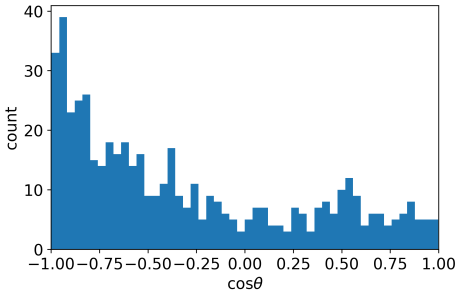

(c) *fac*-Ir(dbfmi)$_3$ mixtures simulated with MC.

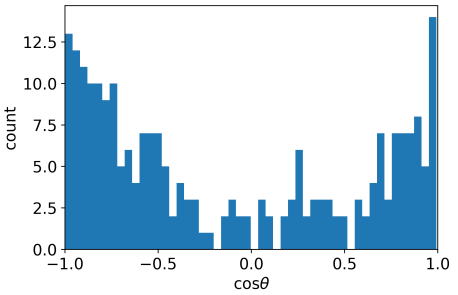

(d) *fac*-Ir(dbfmi)$_3$ mixtures simulated with MD.

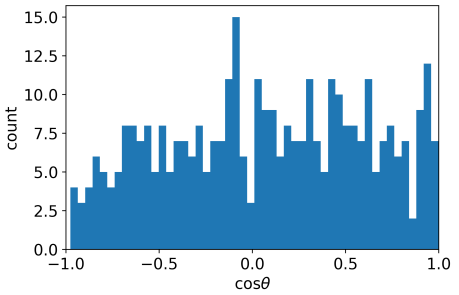

(e) *fac*-A-5 mixtures simulated with MC.

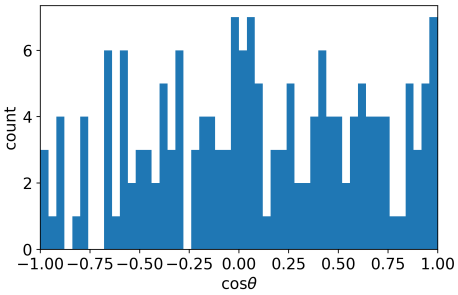

(f) *fac*-A-5 mixtures simulated with MD.

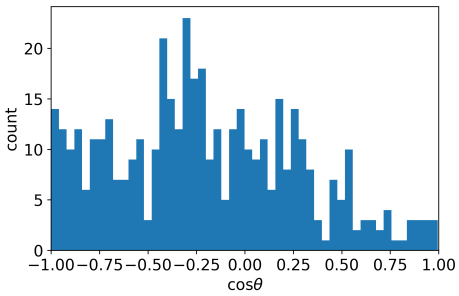

(g) *mer*-B-2 mixtures simulated with MC.

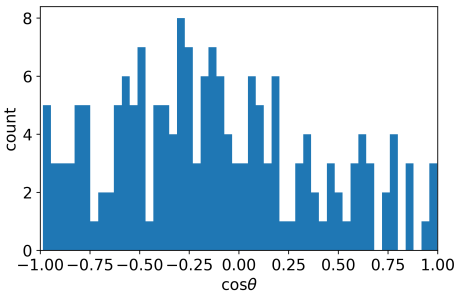

(h) *mer*-B-2 mixtures simulated with MD.

Fig. 6.8.: Histograms of $\cos\theta$ (with θ being the angle between dipole moment and z-axis) of all emitter molecules deposited in mixture with DPEPO.

7 Improving the forcefield

In the previous chapters, two different deposition approaches have been used to simulate the PVD process of pure (chapter 5) and mixed (chapter 6) organic film structures. Several film properties have been compared to available experimental data. It has been shown that while the MD deposition method seems to capture the anisotropy of the refractive index and the overall mass density better, the MC approach predicts the emitter orientation better, while also being the computationally cheaper method due to its linear scaling with system size. This chapter aims to improve the existing intra- and intermolecular forcefields by a neural network approach based on the initial work of Friederich et al. [130]. In their work they showed, that given a large enough set of sample data, the changes in intramolecular energy contributions due to dihedral rotations can in principle be learned by a artificial neural network (ANN). In this thesis, the same ANN model is used to learn the dihedral energy contributions aswell as changes in partial charges due to dihdral rotations. The ANN is furthermore embedded in an iterative workflow to efficiently create new sample data points, automatically stopping when a desired accuracy is reached. The hole transport material NPB is then used as a test candidate to generate ANN forcefields for dihedral energies and charges. Finally, the created force fields were implemented and used in the MC deposition approach.

7.1 Accuracy of GROMOS 54A7 force field

To describe changes in internal energy of a given molecule induced by the rotation of its dihedral fragments, a conventional MD force field is typically using a set of analytic functions (for example eq. (2.23) and eq. (2.24)), which are parametrized either empirically or fitted to quantum chemical calculations for each individual dihedral degree of freedom. Additionally, partial charges are fitted to the quantum chemical calculation of a reference geometry (usually

the ground state) and kept fixed throughout the whole simulation. To assess how accurate such a conventional force field is, a set of 1000 conformations of NPB is taken from one of the structures generated by the MC approach in chapter 5. On this set, the changes in total energy are calculated with the GROMOS 54A7 forcefield [51] (which was used during the deposition simulations) as well as with DFT on two levels of accuracy: (a) B-P functional and def-SV(P) basis and (b) B3-LYP functional and def2-SV(P) basis [36, 108]. After each DFT calculations also a new set of partial charges is extracted using a fit of the electrostatic potential as described in [101]. The results of the energy calculations are plotted in fig. 7.1, where $\Delta E = E^n - E^0$ and E^n corresponds to the total energy of the n-th conformer of the testset. It is shown that while the order of magnitude of ΔE is in agreement between both methods, the coefficient of determination R^2 is negative in both comparisons between GROMOS and DFT, showing that the GROMOS force field is unable to correctly model the changes in internal energy. Looking at the comparison between both DFT levels, a good agreement with $R^2 = 0.94$ is found, suggesting that the computationally cheaper method can be used to calculate ΔE with a similar accuracy. Furthermore the error of using the fixed set of partial charges was quantified by calculating the root mean squared error (RMSE):

$$\mathrm{RMSE}^{(\mathrm{def-SV(P)/B-P)/GROMOS}} = 0.113e \tag{7.1}$$

$$\mathrm{RMSE}^{(\mathrm{def2-SVP/B3-LYP)/GROMOS}} = 0.122e \tag{7.2}$$

$$\mathrm{RMSE}^{(\mathrm{def2-SVP/B3-LYP)/def-SV(P)/B-P)}} = 0.017e \tag{7.3}$$

where e is the elementary charge. Again only a small deviation was found between both DFT methods, which is why the computationally cheapter method (def-SV(P) / B-P) was chosen during the data sampling workflow of the test molecule in section 7.4.

7.2 Structure of neural network

In their work from 2018, Friederich et al. [130] showed, that the dihedral energies of several different organic materials (including NPB) could be predicted by a molecule specific artificial neural network (ANN), if it was trained on a large enough set of datapoints. The same type of ANN was used in this work

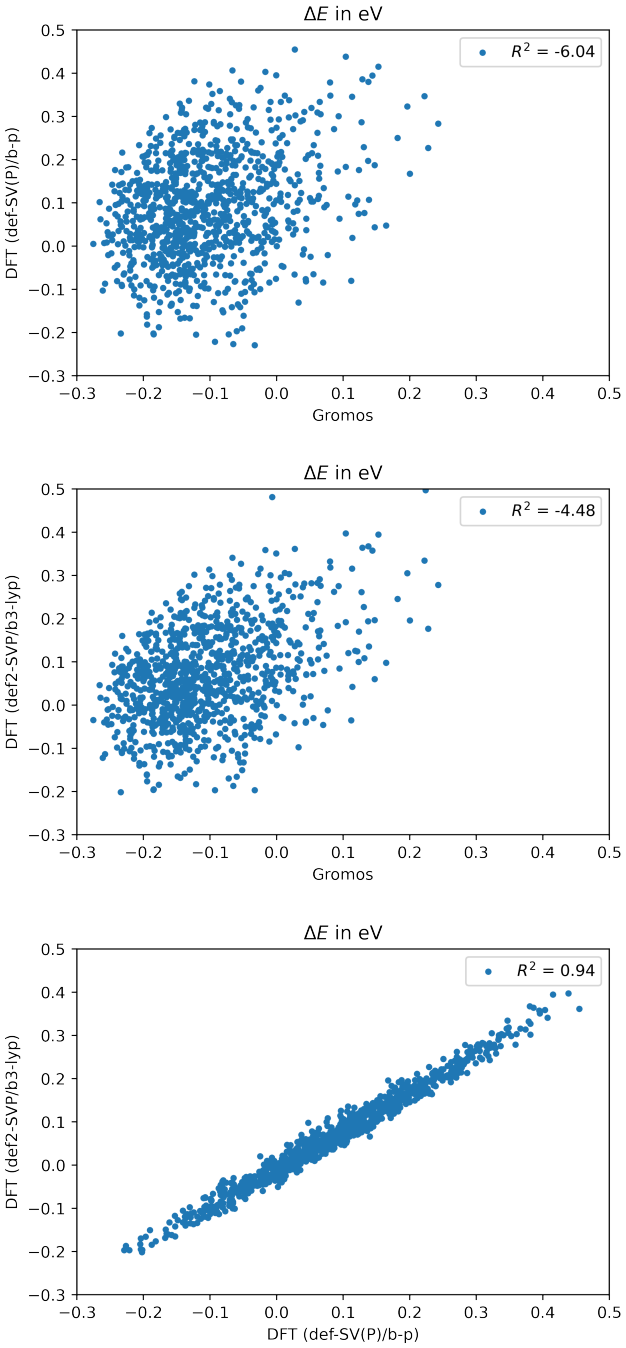

Fig. 7.1.: Comparison of the changes in total energy ΔE as calculated by either the GROMOS 54A7 forcefield or DFT based on two levels of accuracy: (a) B-P functional and def-SV(P) basis and (b) B3-LYP functional and def2-SV(P) basis. (c) shows a comparison between both DFT models.

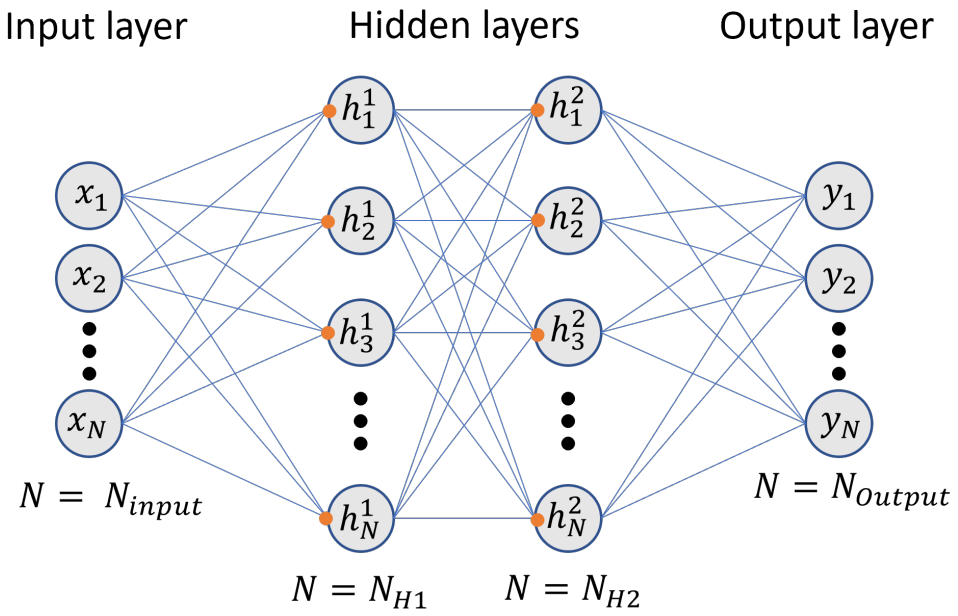

Fig. 7.2.: Structure of the ANN used in this work. Each neuron (circles) contains a number and is connected to all neurons of the following layer by a set of weights and biases (blue lines). Furthermore, each neuron in the hidden layer is activated by a sigmoid activation function (orange dot). The size of the input layer N_{input} depends on the number of dihedral angles in the molecule (see eq. (7.4)), the size of the hidden layers N_{H1} and H_{H2} can be adjusted and the size of the output layer is either 1 (for the dihedral energy) or the number of atoms (= number of partial charges) of the molecule.

for the prediction of dihedral energies or partial charges and its structure is shown in fig. 7.2. It consists of an input layer, two hidden layers and an output layer (see fig. 7.2). The values of the input layer are the $N_{\text{dihedrals}}$ dihedral angles ϕ_n of the molecule aswell as sine and cosine values of these angles with 11 different periodicities k:

$$\text{InputLayer}: \begin{cases} \phi_n \\ \vdots \\ \cos\left(k\phi_n\right) \\ \vdots \\ \sin\left(k\phi_n\right) \\ \vdots \end{cases}$$

with $n \in \{1, 2, \ldots, N_{\text{dihedrals}}\}$ and $k \in \{0.5, 1, 2, \ldots, 10\}$, leading to a total of N_{input}

$$N_{\text{input}} = N_{\text{dihedrals}} + 2 \times 11 \times N_{\text{dihedrals}} \tag{7.4}$$

input values. The numbers of the first hidden layer $\mathbf{h}^1$ are calculated using the sigmoid activation function:

$$h_i^1 = \frac{1}{1 + e^{-v_i}} \tag{7.5}$$

where the activations v_i are calculating from the input layer $\mathbf{x}$ as follows:

$$v_i = \sum_{j=1}^{N_{input}} x_j w_{ji} + b_i \tag{7.6}$$

with the weights w_{ji} and biases b_i. The values of the following layers are calculated in a similar fashion with their own respective weights and biases. For the calculation of the output layer, no activation function is used. Its size is either 1 in the case of energy prediction or equal to the number of atoms in the molecule in the case of partial charge prediction.

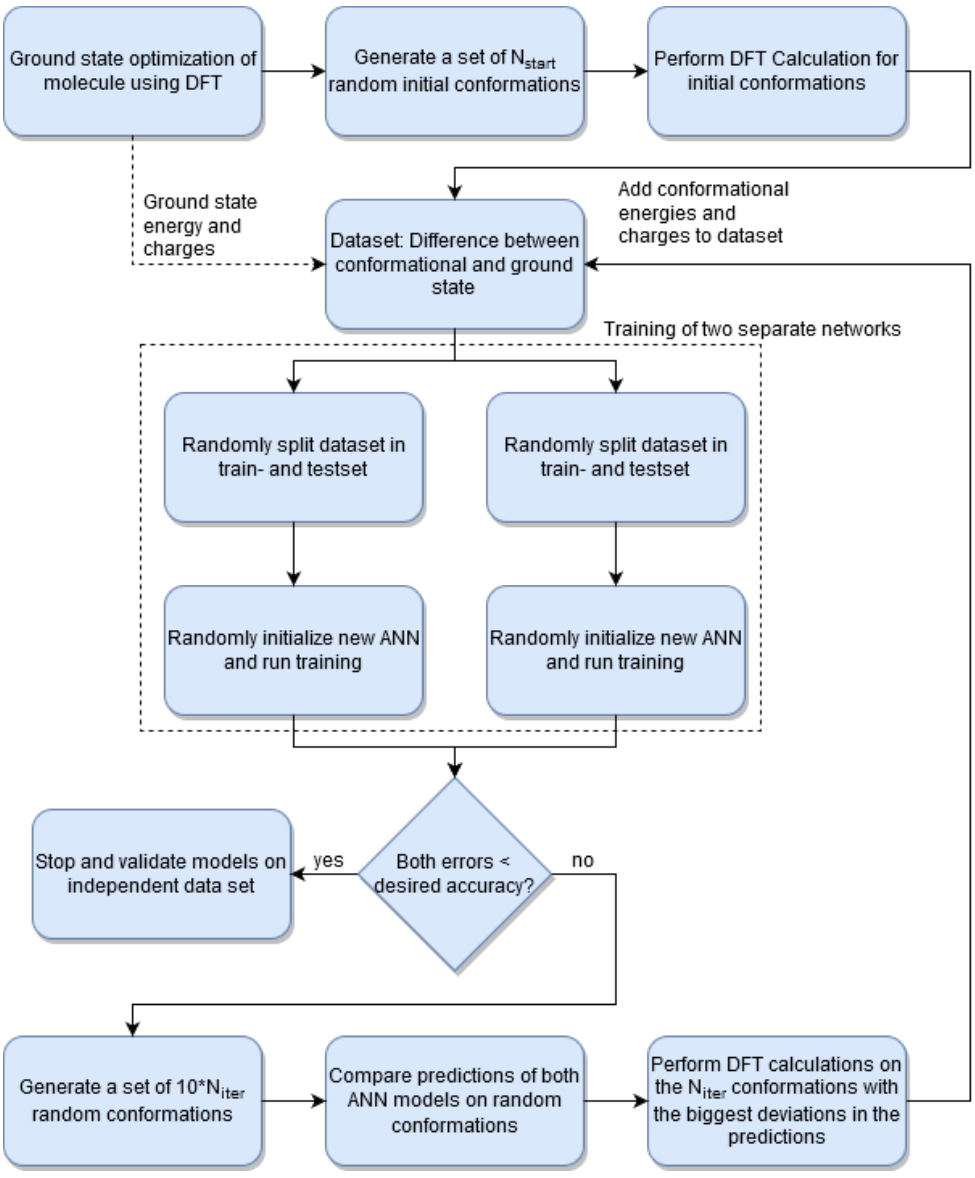

Fig. 7.3.: Workflow diagram for the iterative NN data set generation.

7.3 Sampling of input data

Two big challenges of using the ANN approach explained above, are the large amount of datapoints needed (and with that a high demand of computational power) and the uncertainty of knowing how many and which data points are needed. Therefore, in this thesis a workflow to iteratively generate new data points using DFT calculations was developed and is explained in this section (see fig. 7.3).

The workflow starts by performing a ground state optimization of the molecular geometry and a subsequent single point calculation using DFT. The resulting ground state energy and charges are then saved and used as a reference in the training of the ANN. Afterwards a set of N_{Start} random conformations is generated. This is done by suggesting a new set of dihedral angles and performing a sanity check on the resulting geometry: if two atoms of the different dihedral fragments come closer than $1.8\,\text{Å}$ towards each other, the set of dihedral angles is discarded. On each of the so generated conformations a single point DFT calculation is performed and the resulting energies and charges are added to the dataset. Next the workflow is split in two independent branches. In each branch the dataset is split randomly in 80% train- and 20% testdata and an ANN is initialized with random weights and biases. The inputs for the ANN are calculated as mentioned in the previous section and the target output values are taken as the difference between the single point energy (or charge) of the conformer and the previously calculated reference ground state value. At the start of every training epoch the order of conformations in the trainingset is randomized. Afterwards a batch of N_{Batch} conformations are put in the ANN and the predicted output values are calculated. Using the root mean squared deviation (RMSD) as a loss function, the weights and biases of the ANN are updated using the Adam opimization method [131] after each batch. Next the updated ANN is used on the trainings- and testset and the RMSD error of both sets is calculated and saved. This procedure is stopped if the error of the test set is not decreasing for 50 epochs in a row, furthermore the learning rate of the Adam method is halfed after every 25 epochs without decreasing the error of the test set. The final error is taken as the lowest error of the test set during the training and the error and its corresponding model is returned to the data point sampling workflow. The workflow then checks if

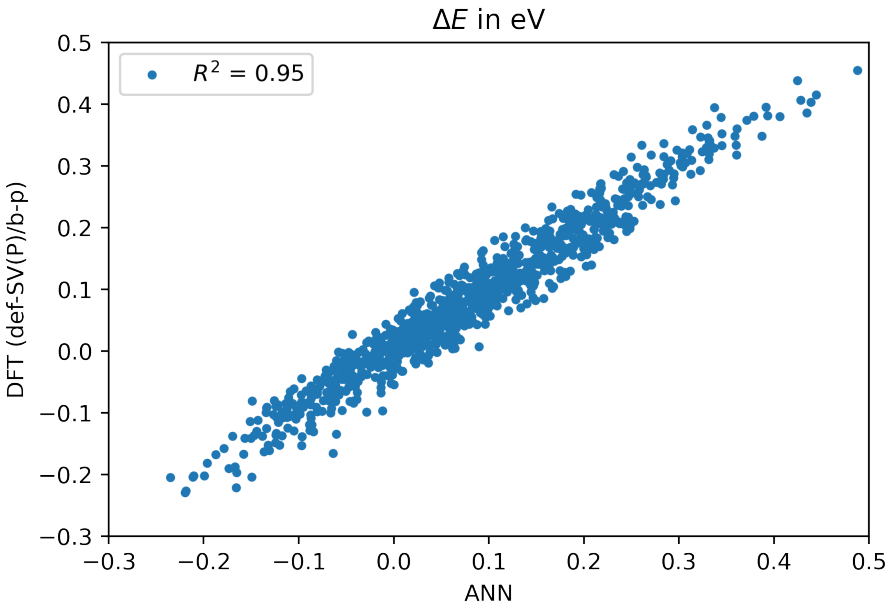

Fig. 7.4.: Comparison of the changes in total energy ΔE as calculated by the ANN and the DFT method against which the ANN was trained (B-P functional and def-SV(P) basis).

both test errors are below a certain threshold, if so the workflow is stopped. If this is not the case, a larger set of $10 \cdot N_{\mathrm{Iter}}$ new random conformations is generated. All of these datapoints are then put through both models again and their predictions are compared. The N_{Iter} conformations with the biggest deviations in the prediction between both models are calculated with DFT and added to the dataset. This procedure is then repeated until the desired accuracy is reached or a predefined maximum number of datapoints has been created.

7.4 Results for NPB

To test the described sampling method aswell as the prediction of energy and charges with an ANN, NPB is used in this section as a test candidate using the following parameters:

- DFT method: B-P functional and def-SV(P) basis set

Tab. 7.1.: Comparison of the structure generated using the ANN compared to the structures solely using the GROMOS 54A7 forcefield from chapter 5. All properties were extracted in the same fashion as described in chapter 5.

Method	ρ [g/cm^3]	n_o	n_eo	σ_i [meV]	σ [meV]
GROMOS 54A7	1.040 ± 0.003	1.70 ± 0.01	1.64 ± 0.01	79.6 ± 3.7	108 ± 5.4
ANN	1.038 ± 0.003	1.69 ± 0.01	1.64 ± 0.01	89.8 ± 2.8	106 ± 4.3

- $N_\mathrm{Start} = 1000$
- $N_\mathrm{Batch} = 200$
- Learning rate $= 0.0001$
- Desired accuracy: $\Delta E = 50\,\mathrm{meV}$ and $\Delta q = 0.01e$
- Number of neurons in hidden layers: 100/10 for energy prediction and 100/100 for charge prediction

The sampling workflow ended after 44 iterations creating a total of 45000 sample points, which is over a factor 3 smaller than the number of sample points used in the initial publication [130]. As a validation data set the conformations from section 7.1 were used. The results are plotted in fig. 7.4. A good agreement with $R^2 = 0.95$ is achieved for the prediction of ΔE, for the partial charges the RMSE was $0.009e$.

Finally, the MC deposition protocol was modified to use the trained ANNs to calculate the dihedral energy and partial charges of the deposited molecule in every MC step. This modified protocol was then used to create 5 new films of NPB each containing 1000 molecules. These films were then analyzed in the same way as the pure GROMOS structures from chapter 5. The resulting values for density, refractive index and electronic disorders are given in table 7.1. The only property showing a difference which is outside the range of the statistical error is the intrinsic electronic disorder, which is around $10\,\mathrm{meV}$ higher in the ANN structures. Because the total disorder is the same this also means that the polarisation part is smaller for the ANN structures. These rather small differences in the final film structure compared to the shown differences in accuracy between the underlying GROMOS or ANN based force field are due to the fact that the Lennard-Jones energy is the main energy contribution during

the deposition process and therefore the relevant factor influencing the film morphology, which is especially true for the almost unpolar material NPB.

8 Summary and outlook

8.1 Summary

Most of the already established theoretical models describing inorganic semiconductors are based on the periodic arrangement of the constituent atoms and therefore can not be applied to the amorphous structures of organic semiconductors. Therefore, a new set of methods and tools needs to be developed to better understand the relationship between the properties of single molecules and the thin film used in the final organic light emitting (OLED) device. One way of closing this gap is through the simulation of the electronic structure and charge transport on a molecular level. The starting point for such a bottom-up approach is to predict the correct arrangement and packing of organic semiconductors in the amorphous bulk morphology.

In this thesis, two different methods aimed at simulating the physical vapor deposition of small organic molecules are presented. Both methods use molecular mechanical forcefields to describe the inter- and intramolecular interactions. The first method is an already established Monte-Carlo (MC) based deposition protocol, which only allows the rotation of dihedral fragments as intramolecular degrees of freedom. Furthermore all molecules are deposited one at a time and frozen in place after the deposition. In this approximation, the substrate is effectively frozen, since collective motions are assumed to be negligible. This allows the use of a Lennard-Jones and a Coulomb grid for the intermolecular interactions, which can be updated after each deposition, enabling a linear scaling of the simulation time with system size. This enables the computational effort to be completely focused on scanning the available phase space during deposition. For the second method, a molecular dynamics approach was developed and implemented in this dissertation. Here each molecule is modelled as a fully flexible bonded unit, allowing for bond and bond angle changes. Each deposition process is simulated by a separate molecular dynamics (MD) run of the system, where new molecules with a velocity vector pointing towards the

substrate are inserted at the start of the run. Since all molecules are allowed to move, collective movements and adjustements of the substrate towards new molecules are possible but limited by the total simulation time. However these additions come at the cost of a higher computational effort, which leads to a deposition rate that is several orders of magnitude below realistic values.

In chapter 5 both deposition approaches were used to create sample films for four literature known semiconductor materials. It is shown that the structures generated by the MD approach show a higher mass density, indicating that a different packing in both films has to exist. The packing is then further analysed by calculating radial distribution functions for all films and looking at the orientation of individual dihedral fragments. It is found that the distribution of core fragments in the MD approach is much closer to an isotropic distribution, while the MC approach shows a significant anisotropy for three of the four materials. These anisotropies are further explored by investigating the ordinary and extra-ordinary refractive index values. Again the values of the MD films are much closer to the experimental findings, which is linked to the overall more isotropic orientation observed before. To see how the qualitatively different packings influence the charge carrier mobilities, electronic structure calculations were performed using the QuantumPatch method [24]. From these the intrinsic and total energy disorders as well as average intermolecular hopping-matrix elements were extracted. The intrinsic disorder is shown to be slightly higher for the MD films, which is expected because the more flexible molecules in the MD lead to a larger space of available conformations. Even though this higher intrinsic disorder, the total disorder is lower or comparable to the values for the MC films, meaning that the contribution through the polarization of the surrounding environment is higher in the MD films. Finally the deposited films, together with the results of the electronic structure calculations, were put in a kinetic Monte-Carlo simulation to calculate field dependent charge carrier mobilities. The disorder proves to be the main factor influencing the mobility.

In chapter 6, a set of 12 different emitter molecules co-deposited with the host material DPEPO have been investigated. All of the 12 emitters contain a $Ir(dbfmi)_3$ core where different additions have been made to the ligands. To analyse the orientation, the optical orientation parameter, which is relevant for the outcoupling of light from the OLED device, has been calculated by

mapping transition dipole moments from TD-DFT onto the emitters in the thin film structures. Overall, both methods predict the trend correctly with the MC deposit achieving better results, which can be explained by the better sampling of each individual molecule during the deposition process, which is the determining factor for these emitter complexes, which are mostly rigid. Secondly, the giant surface potential (GSP) was calculated for pure host films as well as four different host emitter mixtures. The GSP is built up by a net orientation of molecular dipole moments in the thin film, therefore the dipole moments were calculated for all molecules in the film using the QuantumPatch method. A very good agreement is found between MC films and experiment. The results for the MD films, however, are completely wrong due to a wrong prediction of the host dipole moments which make up the dominating part of the GSP. The most likely explanation for this is that the MD force field used does not describe the host material with sufficient accuracy.

In chapter 7 an artificial neural network (ANN) approach for predicting changes in the total energy upon rotation of dihedral fragments from Friederich *et al.* [130] was implemented in a parametrization workflow. The main drawback of the ANN approach is the costly generation of training data, which requires a density functional theory (DFT) calculation for every data point. Furthermore the number of required data points heavily depends on the size, symmetry and number of dihedral angles, ranging from 3000 to 150000 in the original publication. To reduce the computational effort and find a sufficient number of datapoints, a workflow which iteratively identifies new datapoints was developed and implemented in this thesis. The workflow was then used with NPB serving as a realistic candidate molecule. Subsequently, the generated training data was used to train an ANN for the prediction of the dihedral energy contributions as well as an ANN for the prediciction of changes in the partial charges. Both ANNs were then implemented to work in conjunction with the MC based deposition protocol.

8.2 Outlook

As shown in this work, important device parameters like field dependant charge carrier mobility and emitter orientation can already be calculated with good

accuracy using *in silico* generated film morphologies. However, the methods presented in this paper also provide several areas for potential improvement. For the MC based deposition, a more accurate description of the underlying intramolecular forcefield could be achieved for example by a parametrization of relevant bond angles, which allow the molecule to be more flexible during the deposition. For the MD based approach the biggest challenge is the short deposition time and bad scaling with system size, which is both strongly limited by the available computational power. Since only the final structure is of relevance for the presented methods in this work, most of the simulation time is wasted on the fastest vibrations in the molecule. A possible improvement could be the implementation of coarse grained models specifically aimed at organic semiconductor materials, which was already shown to be successful for NPB by Ricci et al. [132] in 2019.

Appendix

A

Derivation of the GSP slope Assuming that the dipole moments $\mathbf{p}_i$ can be approximated by a constant dipole density $\mathbf{P} = \frac{\langle p \rangle \mathbf{e}_z}{V} = \frac{\mathbf{p}_i}{\Delta V_i}$, the sum in eq. (4.14) can be converted into an integral by putting a small volume element ΔV_i around each dipole moment:

$$\Phi(\mathbf{r}) = \sum_i^N \frac{1}{4\pi\epsilon_0\epsilon} \frac{\mathbf{p}_i/\Delta V_i \cdot (\mathbf{r} - \mathbf{R}_i)}{|\mathbf{r} - \mathbf{R}_i|^3} \Delta V_i$$

$$\Phi(\mathbf{r}) = \int \frac{1}{4\pi\epsilon_0\epsilon} \frac{\mathbf{P} \cdot (\mathbf{r} - \mathbf{R}_i)}{|\mathbf{r} - \mathbf{R}_i|^3} dV'$$

$$\Phi(\mathbf{r}) = \frac{1}{4\pi\epsilon_0\epsilon} \frac{\langle p \rangle}{V} \int_{-\infty}^{\infty} \int_{-\infty}^{\infty} \int_0^t \frac{\mathbf{e}_z \cdot (\mathbf{r} - \mathbf{R}_i)}{|\mathbf{r} - \mathbf{R}_i|^3} dx' dy' dz'$$

To calculate V^{GSP} only the values of the electrostatic potential at $z = t$ and $z = 0$ are of interest, we can therefor set $x = y = 0$ for simplicity in the following steps:

$$\Phi(\mathbf{r} = z\mathbf{e}_z) = \frac{1}{4\pi\epsilon_0\epsilon} \frac{\langle p \rangle}{V} \int_{-\infty}^{\infty} \int_{-\infty}^{\infty} \int_0^t \frac{(z - z')}{\left(x'^2 + y'^2 + (z - z')^2\right)^{3/2}} dx' dy' dz'$$

$$\Phi(\mathbf{r} = z\mathbf{e}_z) = \frac{1}{4\pi\epsilon_0\epsilon} \frac{\langle p \rangle}{V} \int_{-\infty}^{\infty} \int_0^t \frac{2(z - z')}{y'^2 + (z - z')^2} dy' dz'$$

$$\Phi(\mathbf{r} = z\mathbf{e}_z) = \frac{1}{2\pi\epsilon_0\epsilon} \frac{\langle p \rangle}{V} \int_0^t \frac{\pi(z - z')}{\sqrt{(z - z')^2}} dz'$$

$$\Phi(z = t) = \frac{1}{2\epsilon_0\epsilon} \frac{\langle p \rangle}{V} \int_0^t \frac{(t - z')}{\sqrt{(t - z')^2}} dz' = \frac{1}{2\epsilon_0\epsilon} \frac{\langle p \rangle}{V} \int_0^t dz' = \frac{t}{2\epsilon_0\epsilon} \frac{\langle p \rangle}{V}$$

$$\Phi(z = 0) = \frac{1}{2\epsilon_0\epsilon} \frac{\langle p \rangle}{V} \int_0^t \frac{(0 - z')}{\sqrt{(0 - z')^2}} dz' = \frac{1}{2\epsilon_0\epsilon} \frac{\langle p \rangle}{V} \int_0^t -1 dz' = -\frac{t}{2\epsilon_0\epsilon} \frac{\langle p \rangle}{V}$$

$$\Rightarrow V^{\mathrm{GSP}} = \Phi(z = t) - \Phi(z = 0) = \frac{\langle p \rangle t}{V\epsilon_0\epsilon}$$

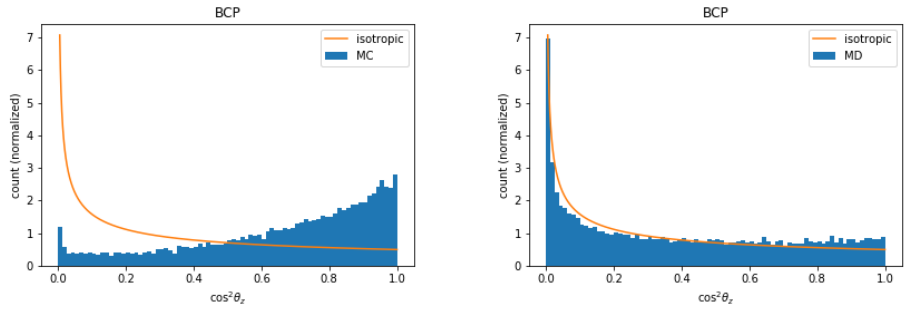

(a) Phenanthrolin core fragment in MC

(b) Phenanthrolin core fragment in MD

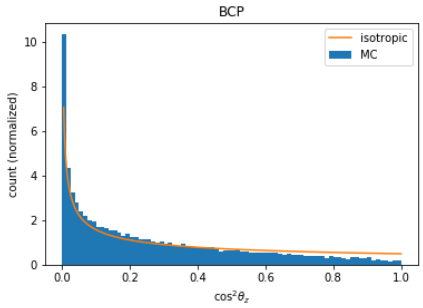

(c) Phenyl ring fragment in MC

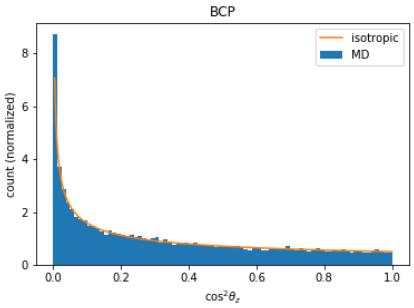

(d) Phenyl ring fragment in MD

Fig. A.1.: Histograms of the order parameter $cos^2\theta_z$ for the dihedral fragments of BCP.

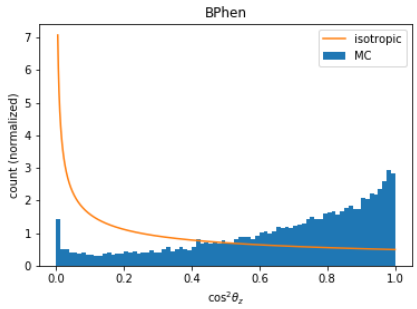

(a) Phenanthrolin core fragment in MC

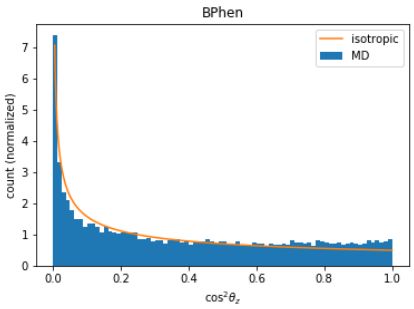

(b) Phenanthrolin core fragment in MD

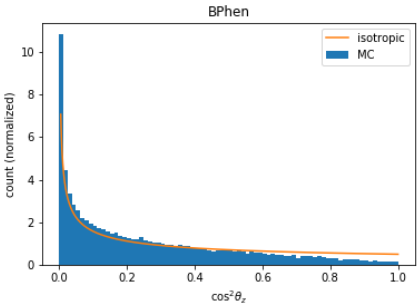

(c) Phenyl ring fragment in MC

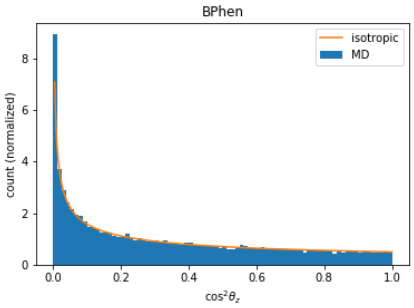

(d) Phenyl ring fragment in MD

Fig. A.2.: Histograms of the order parameter $cos^2\theta_z$ for the dihedral fragments of BPhen.

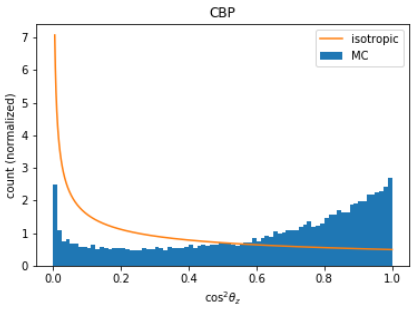

(a) Center phenyl ring fragment in MC

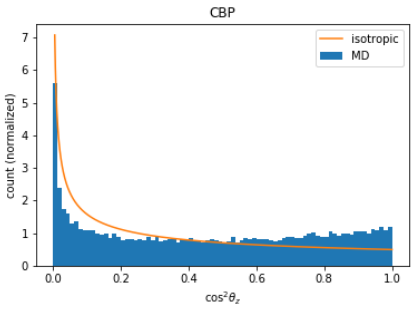

(b) Center phenyl ring fragment in MD

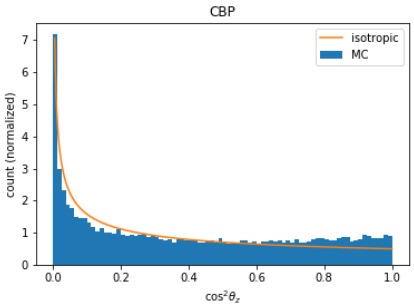

(c) Carbazol fragment in MC

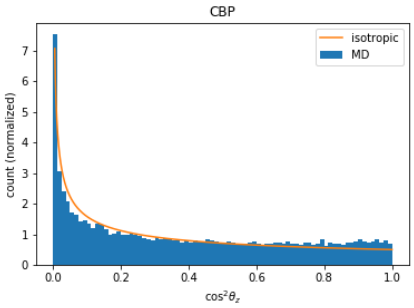

(d) Carbazol fragment in MD

Fig. A.3.: Histograms of the order parameter $cos^2\theta_z$ for the dihedral fragments of CBP.

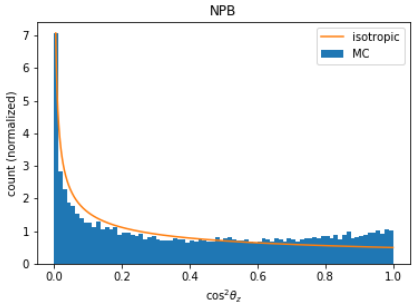

(a) Center phenyl ring fragment in MC

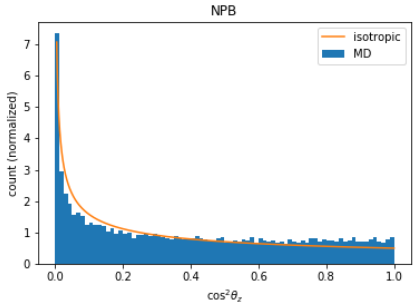

(b) Center phenyl ring fragment in MD

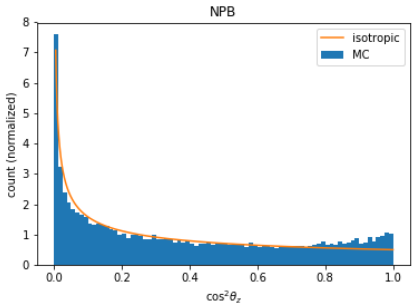

(c) Naphthyl fragment in MC

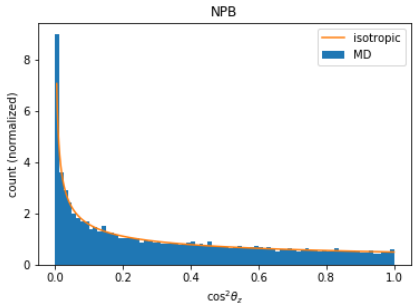

(d) Naphthyl fragment in MD

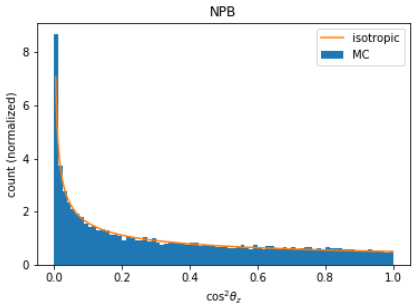

(e) Outer phenyl ring fragment in MC

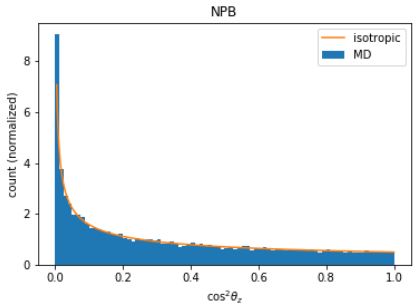

(f) Outer phenyl ring fragment in MD

Fig. A.4.: Histograms of the order parameter $cos^2\theta_z$ for the dihedral fragments of NPB.

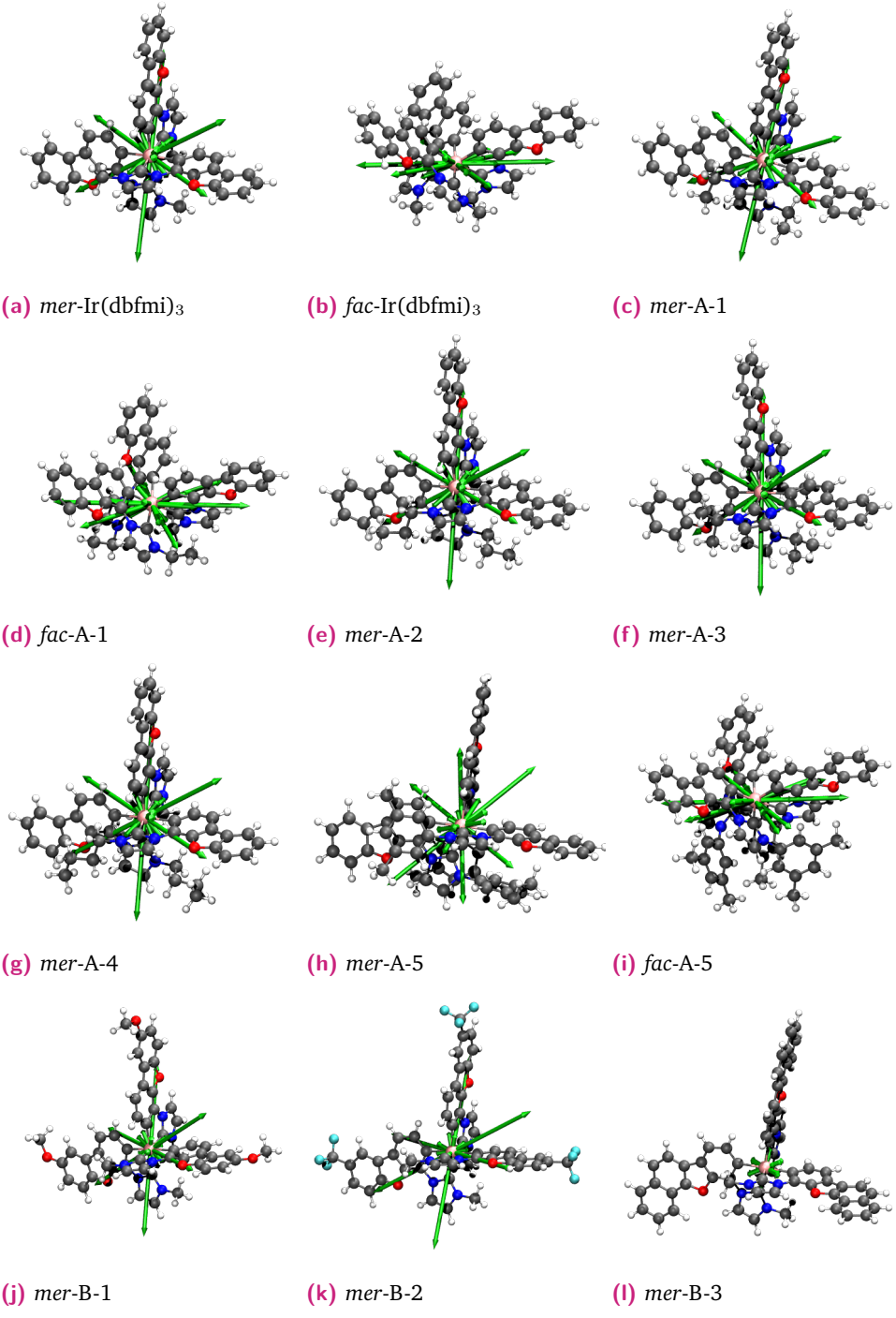

(a) *mer*-Ir(dbfmi)$_3$ (b) *fac*-Ir(dbfmi)$_3$ (c) *mer*-A-1

(d) *fac*-A-1 (e) *mer*-A-2 (f) *mer*-A-3

(g) *mer*-A-4 (h) *mer*-A-5 (i) *fac*-A-5

(j) *mer*-B-1 (k) *mer*-B-2 (l) *mer*-B-3

Fig. A.5.: Visualized structures of all homoleptic iridium carbene complexes studied in chapter 6. The calculated and mapped TDM and -1× TDM vectors are printed with the Iridium atom as their origin.

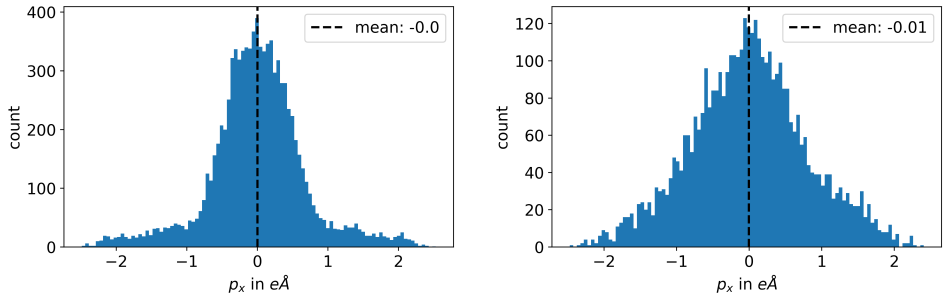

(a) p_x-component in MC structures

(b) p_x-component in MD structures

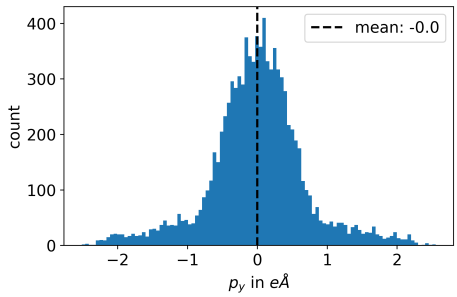

(c) p_y-component in MC structures

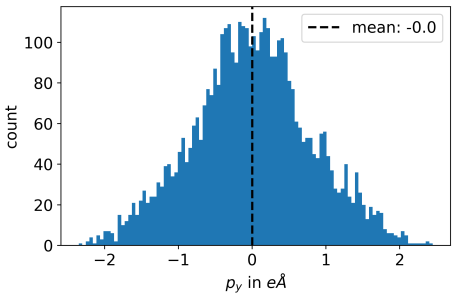

(d) p_y-component in MD structures

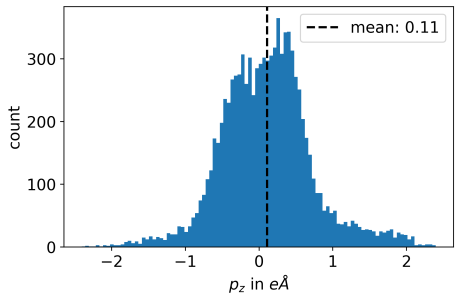

(e) p_z-component in MC structures

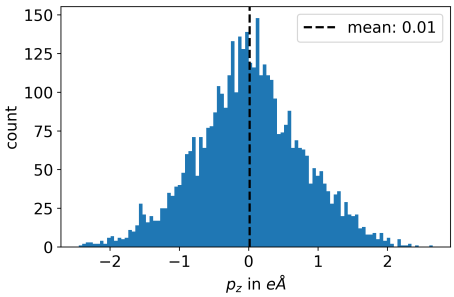

(f) p_z-component in MD structures

Fig. A.6.: Histograms of the calculated dipole moment components of the pure DPEPO films.

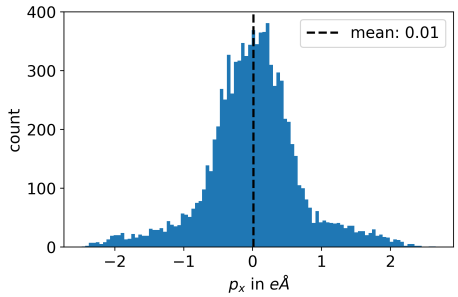

(a) p_x-component in MC structures

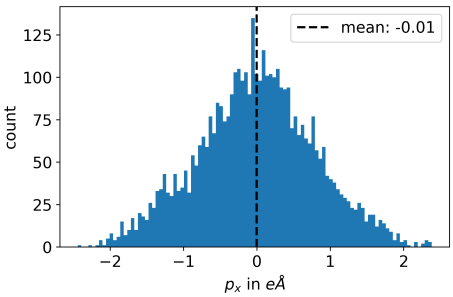

(b) p_x-component in MD structures

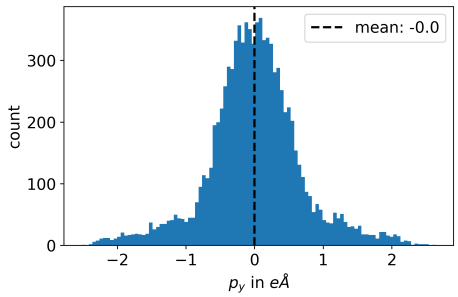

(c) p_y-component in MC structures

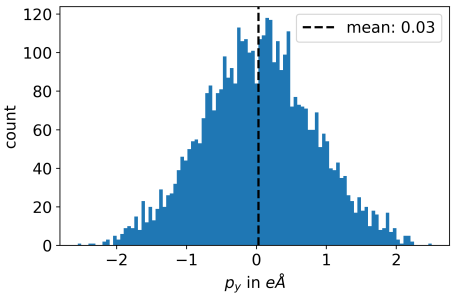

(d) p_y-component in MD structures

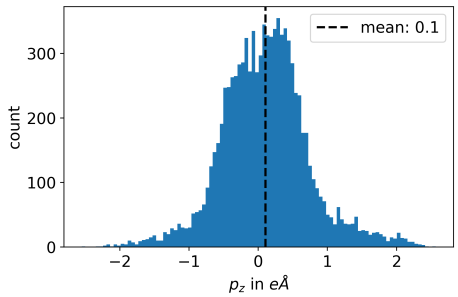

(e) p_z-component in MC structures

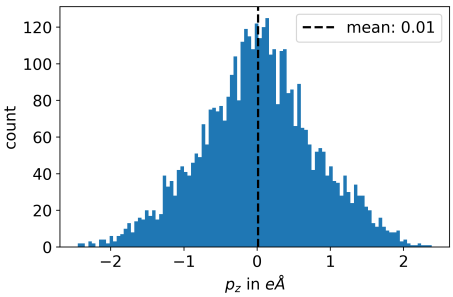

(f) p_z-component in MD structures

Fig. A.7.: Histograms of the calculated dipole moment components of the *mer*-Ir(dbfmi)$_3$/DPEPO mixtures.

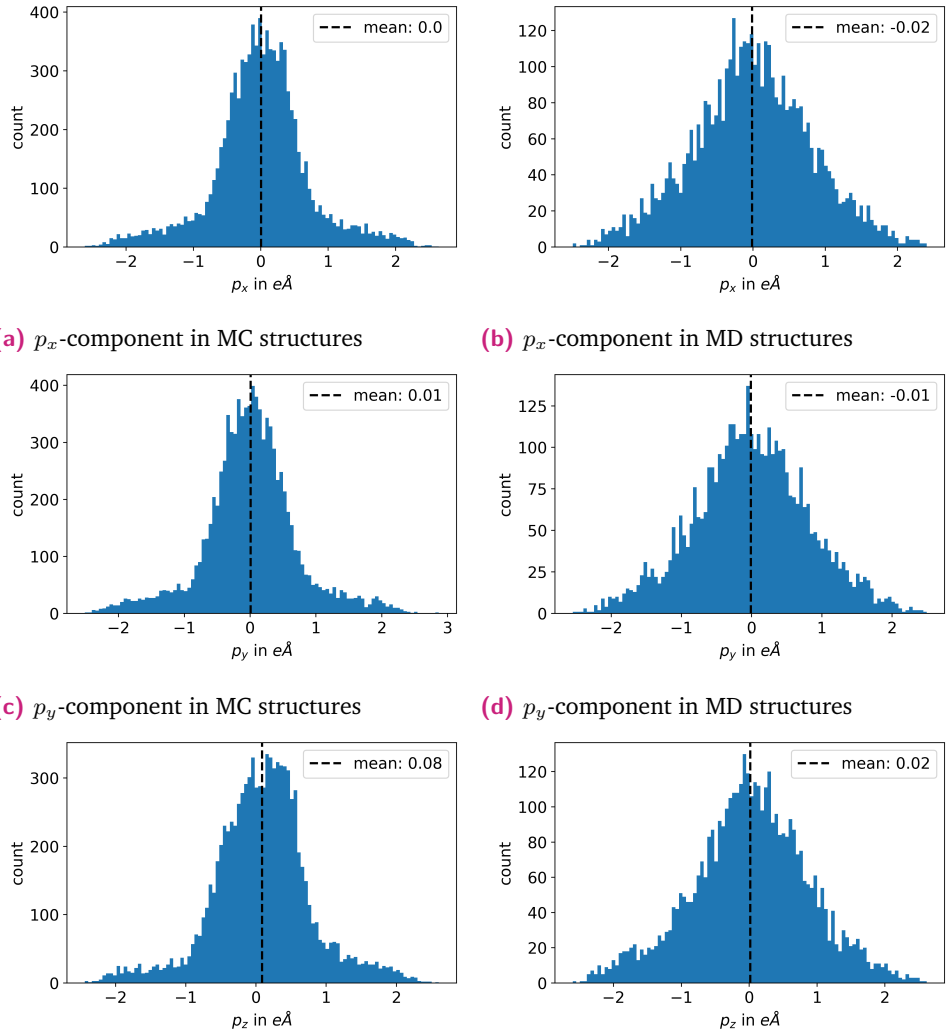

(a) p_x-component in MC structures

(b) p_x-component in MD structures

(c) p_y-component in MC structures

(d) p_y-component in MD structures

(e) p_z-component in MC structures

(f) p_z-component in MD structures

Fig. A.8.: Histograms of the calculated dipole moment components of the *fac*-Ir(dbfmi)$_3$/DPEPO mixtures.

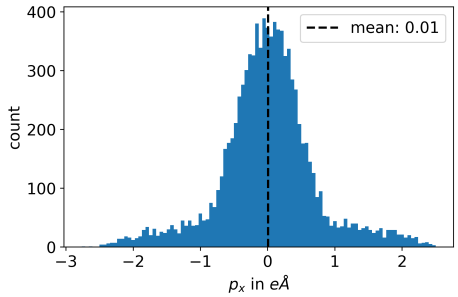

(a) p_x-component in MC structures

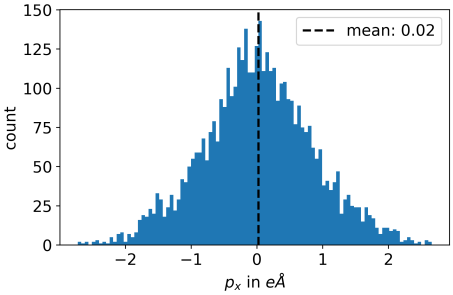

(b) p_x-component in MD structures

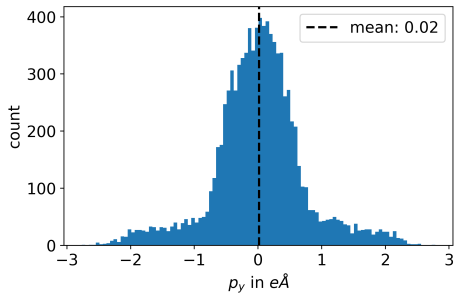

(c) p_y-component in MC structures

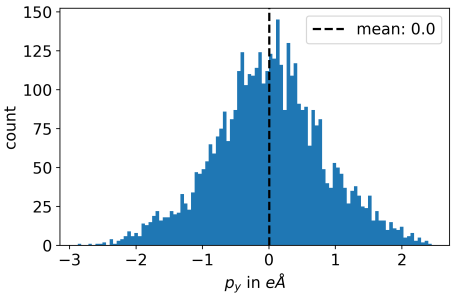

(d) p_y-component in MD structures

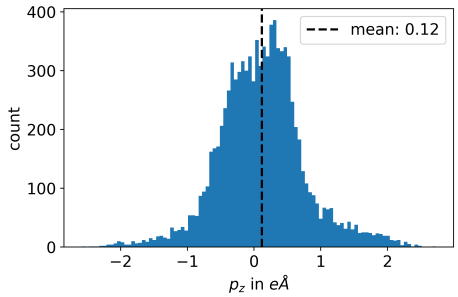

(e) p_z-component in MC structures

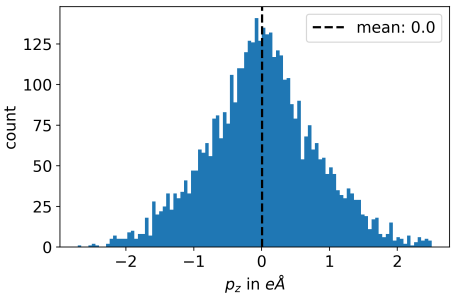

(f) p_z-component in MD structures

Fig. A.9.: Histograms of the calculated dipole moment components of the pure *fac*-A-5/DPEPO mixtures.

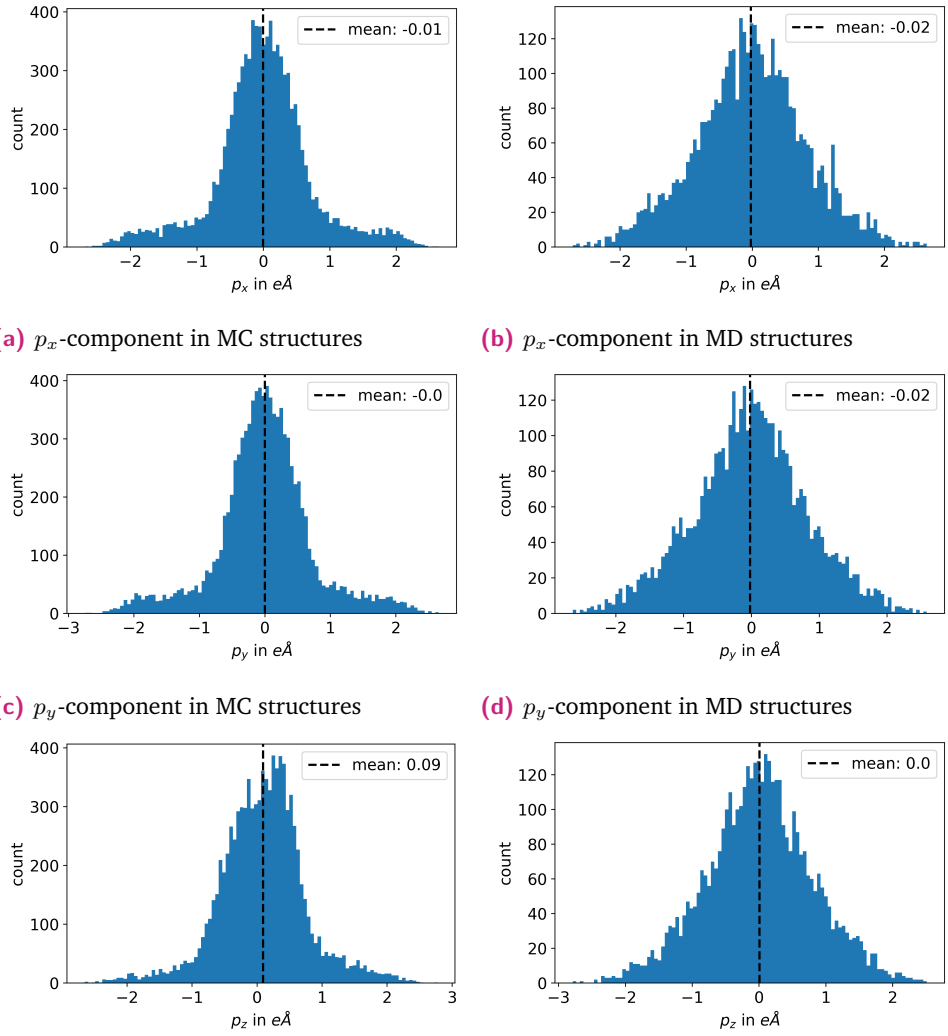

(a) p_x-component in MC structures

(b) p_x-component in MD structures

(c) p_y-component in MC structures

(d) p_y-component in MD structures

(e) p_z-component in MC structures

(f) p_z-component in MD structures

Fig. A.10.: Histograms of the calculated dipole moment components of the pure *mer*-B-2/DPEPO mixtures.

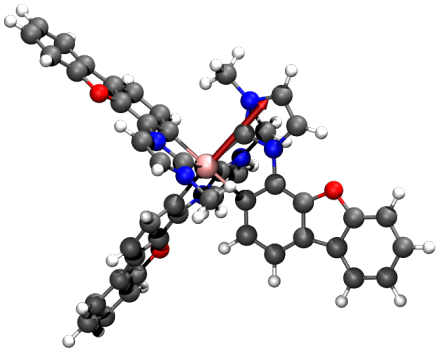

(a) *mer*-Ir(dbfmi)$_3$:

$\langle p \rangle^{MC} = 6.79\,\mathrm{D}$

$\langle p \rangle^{MD} = 7.19\,\mathrm{D}$

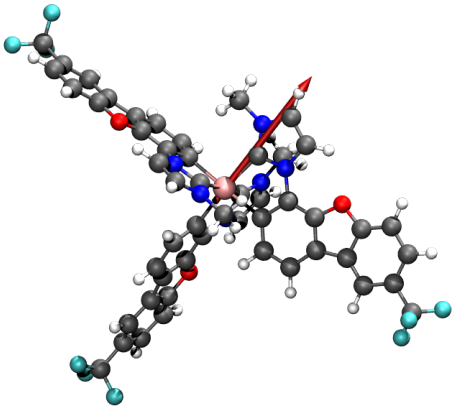

(b) *mer*-B-2:

$\langle p \rangle^{MC} = 11.25\,\mathrm{D}$

$\langle p \rangle^{MD} = 11.70\,\mathrm{D}$

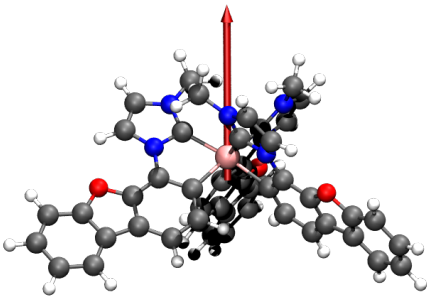

(c) *fac*-Ir(dbfmi)$_3$:

$\langle p \rangle^{MC} = 10.48\,\mathrm{D}$

$\langle p \rangle^{MD} = 11.32\,\mathrm{D}$

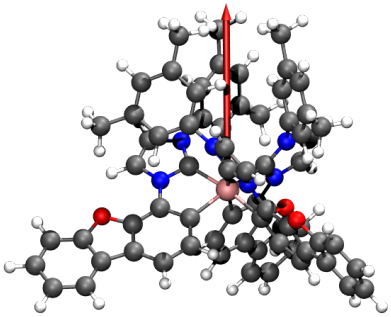

(d) *fac*-A-5:

$\langle p \rangle^{MC} = 11.10\,\mathrm{D}$

$\langle p \rangle^{MD} = 12.02\,\mathrm{D}$

Fig. A.11.: Visualized structures of all homoleptic iridium carbene complexes studied in section 6.4. The calculated permanent dipole moments are printed in red with the center of mass as their origin. $\langle p \rangle^{MC/MD}$ is the average of the absolute dipole moments calculated by the **QuantumPatch** method (see section 6.4) based on the MC or MD morphologies.

Bibliography

[1] *Macworld Expo Keynote Live Update: Introducing the iPhone*. https://www.macworld.com/article/183052/liveupdate-15.html. Accessed: 2022-02-25 (cit. on p. 1).

[2] Ching W Tang and Steven A VanSlyke. "Organic electroluminescent diodes". In: *Applied physics letters* 51.12 (1987), pp. 913–915 (cit. on pp. 1, 2, 29).

[3] Maria Ebling and Mark Corner. "Implantable insulin pump, the first OLED TV, measuring without a ruler..." In: *IEEE Pervasive Computing* 7.1 (2008), pp. 8–9 (cit. on p. 1).

[4] Paul Semenza. "OLEDs in transition". In: *Information Display* 27.10 (2011), pp. 14–16 (cit. on p. 1).

[5] Seunghyup Yoo, Taehyun Kim, Hyeonwoo Lee, et al. "22-4: Invited Paper: OLEDs for Wearables: From Form Factor Engineering to Healthcare Applications". In: *SID Symposium Digest of Technical Papers*. Vol. 52. 1. Wiley Online Library. 2021, pp. 274–277 (cit. on p. 1).

[6] *This is why the iPhone X is Apple's first handset with an OLED display*. https://www.techradar.com/news/this-is-why-the-iphone-x-is-apples-first-handset-with-an-oled-display. Accessed: 2022-02-25 (cit. on p. 1).

[7] *Samsung's foldable phone is real and opens into a tablet*. https://www.cnet.com/tech/mobile/samsung-foldable-phone-is-real-and-opens-extends-into-a-tablet-display-specs-galaxy-x-f/. Accessed: 2022-02-25 (cit. on p. 1).

[8] Bernard Kippelen and Jean-Luc Brédas. "Organic photovoltaics". In: *Energy & Environmental Science* 2.3 (2009), pp. 251–261 (cit. on p. 1).

[9] Jason D Myers and Jiangeng Xue. "Organic semiconductors and their applications in photovoltaic devices". In: *Polymer Reviews* 52.1 (2012), pp. 1–37 (cit. on p. 1).

[10] Christopher R Newman, C Daniel Frisbie, Demetrio A da Silva Filho, et al. "Introduction to organic thin film transistors and design of n-channel organic semiconductors". In: *Chemistry of materials* 16.23 (2004), pp. 4436–4451 (cit. on p. 1).

[11]Christos D Dimitrakopoulos and Patrick RL Malenfant. “Organic thin film transistors for large area electronics”. In: *Advanced materials* 14.2 (2002), pp. 99–117 (cit. on p. 1).

[12]Mitsuhiro Koden. “OLED Fabrication Process”. In: (2017) (cit. on p. 1).

[13]Jeffrey P Spindler, John W Hamer, and Marina E Kondakova. “OLED manufacturing equipment and methods”. In: *Handbook of advanced lighting technology* (2017), pp. 417–441 (cit. on p. 1).

[14]Tae-Woo Lee, Taeyong Noh, Hee-Won Shin, et al. “Characteristics of solution-processed small-molecule organic films and light-emitting diodes compared with their vacuum-deposited counterparts”. In: *Advanced Functional Materials* 19.10 (2009), pp. 1625–1630 (cit. on p. 1).

[15]Gloria Hong, Xuemin Gan, Céline Leonhardt, et al. “A Brief History of OLEDs—Emitter Development and Industry Milestones”. In: *Advanced Materials* 33.9 (2021), p. 2005630 (cit. on pp. 2, 30).

[16]MA Baldo, Ml E ThompSOn, and SR Forrest. “High-efficiency fluorescent organic light-emitting devices using a phosphorescent sensitizer”. In: *Nature* 403.6771 (2000), pp. 750–753 (cit. on p. 2).

[17]Andrew Monkman. “Why Do We Still Need a Stable Long Lifetime Deep Blue OLED Emitter?” In: *ACS Applied Materials & Interfaces* (2021) (cit. on p. 2).

[18]Wenfeng Song, Juanjuan You, Chang-Yen Wu, et al. “5-3: 3-Stacked Top-Emitting White OLEDs with Super-Wide Color Gamut and High Efficiency”. In: *SID Symposium Digest of Technical Papers*. Vol. 50. 1. Wiley Online Library. 2019, pp. 46–49 (cit. on p. 2).

[19]Ayataka Endo, Mai Ogasawara, Atsushi Takahashi, et al. “Thermally activated delayed fluorescence from Sn4+–porphyrin complexes and their application to organic light emitting diodes—A novel mechanism for electroluminescence”. In: *Advanced Materials* 21.47 (2009), pp. 4802–4806 (cit. on p. 2).

[20]Ayataka Endo, Keigo Sato, Kazuaki Yoshimura, et al. “Efficient up-conversion of triplet excitons into a singlet state and its application for organic light emitting diodes”. In: *Applied Physics Letters* 98.8 (2011), p. 42 (cit. on p. 2).

[21]Hiroki Uoyama, Kenichi Goushi, Katsuyuki Shizu, Hiroko Nomura, and Chihaya Adachi. “Highly efficient organic light-emitting diodes from delayed fluorescence”. In: *Nature* 492.7428 (2012), pp. 234–238 (cit. on p. 2).

[22]Chi Y Cheng, Josh E Campbell, and Graeme M Day. “Evolutionary chemical space exploration for functional materials: computational organic semiconductor discovery”. In: *Chemical science* 11.19 (2020), pp. 4922–4933 (cit. on p. 2).

[23] Pascal Friederich, Artem Fediai, Simon Kaiser, et al. “Toward design of novel materials for organic electronics”. In: *Advanced Materials* 31.26 (2019), p. 1808256 (cit. on p. 2).

[24] Pascal Friederich, Franz Symalla, Velimir Meded, Tobias Neumann, and Wolfgang Wenzel. “Ab initio treatment of disorder effects in amorphous organic materials: Toward parameter free materials simulation”. In: *Journal of chemical theory and computation* 10.9 (2014), pp. 3720–3725 (cit. on pp. 2, 47, 48, 94).

[25] Pascal Friederich, Velimir Meded, Franz Symalla, Marcus Elstner, and Wolfgang Wenzel. “QM/QM approach to model energy disorder in amorphous organic semiconductors”. In: *Journal of chemical theory and computation* 11.2 (2015), pp. 560–567 (cit. on p. 2).

[26] Pascal Friederich, Velimir Meded, Angela Poschlad, et al. “Molecular origin of the charge carrier mobility in small molecule organic semiconductors”. In: *Advanced Functional Materials* 26.31 (2016), pp. 5757–5763 (cit. on p. 2).

[27] Simon Kaiser, Naresh B Kotadiya, Roland Rohloff, et al. “De Novo Simulation of Charge Transport through Organic Single-Carrier Devices”. In: *Journal of Chemical Theory and Computation* 17.10 (2021), pp. 6416–6422 (cit. on p. 2).

[28] Simon Kaiser, Tobias Neumann, Franz Symalla, et al. “De novo calculation of the charge carrier mobility in amorphous small molecule organic semiconductors”. In: *Frontiers in chemistry* 9 (2021) (cit. on p. 2).

[29] Tobias Neumann, Denis Danilov, Christian Lennartz, and Wolfgang Wenzel. “Modeling disordered morphologies in organic semiconductors”. In: *Journal of computational chemistry* 34.31 (2013), pp. 2716–2725 (cit. on pp. 2, 18, 39).

[30] AG Fluxim. “Semiconducting emissive thin film optics simulator SETFOS”. In: *Winterthur: Zürich, Switzerland* (2018) (cit. on p. 3).

[31] Max Born and Robert Oppenheimer. “Zur quantentheorie der molekeln”. In: *Annalen der physik* 389.20 (1927), pp. 457–484 (cit. on p. 5).

[32] Pierre Hohenberg and Walter Kohn. “Inhomogeneous electron gas”. In: *Physical review* 136.3B (1964), B864 (cit. on p. 7).

[33] Walter Kohn and Lu Jeu Sham. “Self-consistent equations including exchange and correlation effects”. In: *Physical review* 140.4A (1965), A1133 (cit. on p. 7).

[34] F Bechstedt, F Fuchs, and G Kresse. *Ab-initio theory of semiconductor band structures: New developments and progress*. 2009 (cit. on p. 9).

[35]C Stampfl, W Mannstadt, R Asahi, and Arthur J Freeman. “Electronic structure and physical properties of early transition metal mononitrides: Density-functional theory LDA, GGA, and screened-exchange LDA FLAPW calculations”. In: *Physical Review B* 63.15 (2001), p. 155106 (cit. on p. 9).

[36]Axel D Becke. “Density-functional thermochemistry. I. The effect of the exchange-only gradient correction”. In: *The Journal of chemical physics* 96.3 (1992), pp. 2155–2160 (cit. on pp. 10, 62, 67, 70, 84).

[37]Julian Tirado-Rives and William L Jorgensen. “Performance of B3LYP density functional methods for a large set of organic molecules”. In: *Journal of Chemical Theory and Computation* 4.2 (2008), pp. 297–306 (cit. on p. 10).

[38]Philip J Stephens, Frank J Devlin, Cary F Chabalowski, and Michael J Frisch. “Ab initio calculation of vibrational absorption and circular dichroism spectra using density functional force fields”. In: *The Journal of physical chemistry* 98.45 (1994), pp. 11623–11627 (cit. on p. 10).

[39]GL Oliver and JP Perdew. “Spin-density gradient expansion for the kinetic energy”. In: *Physical Review A* 20.2 (1979), p. 397 (cit. on p. 10).

[40]Axel D Becke. “Density-functional exchange-energy approximation with correct asymptotic behavior”. In: *Physical review A* 38.6 (1988), p. 3098 (cit. on p. 10).

[41]Chengteh Lee, Weitao Yang, and Robert G Parr. “Development of the Colle-Salvetti correlation-energy formula into a functional of the electron density”. In: *Physical review B* 37.2 (1988), p. 785 (cit. on p. 10).

[42]Seymour H Vosko, Leslie Wilk, and Marwan Nusair. “Accurate spin-dependent electron liquid correlation energies for local spin density calculations: a critical analysis”. In: *Canadian Journal of physics* 58.8 (1980), pp. 1200–1211 (cit. on p. 10).

[43]Erich Runge and Eberhard KU Gross. “Density-functional theory for time-dependent systems”. In: *Physical Review Letters* 52.12 (1984), p. 997 (cit. on p. 10).

[44]Robert van Leeuwen. “Mapping from densities to potentials in time-dependent density-functional theory”. In: *Physical review letters* 82.19 (1999), p. 3863 (cit. on p. 10).

[45]Carsten A Ullrich. *Time-dependent density-functional theory : concepts and applications*. Online-Ausg. Oxford Graduate TextsOxford graduate texts. Oxford: Oxford University Press, 2012 (cit. on p. 11).

[46]Paul Adrien Maurice Dirac. “The quantum theory of the emission and absorption of radiation”. In: *Proceedings of the Royal Society of London. Series A, Containing Papers of a Mathematical and Physical Character* 114.767 (1927), pp. 243–265 (cit. on p. 12).

[47] Wolfgang [VerfasserIn] Demtröder. *Atoms, Molecules and Photons : An Introduction to Atomic-, Molecular- and Quantum Physics*. Third edition. Graduate Texts in PhysicsSpringerLinkSpringer eBook Collection. Berlin: Springer, 2018 (cit. on p. 12).

[48] Stefan Seritan, Christoph Bannwarth, Bryan S Fales, et al. "TeraChem: A graphical processing unit-accelerated electronic structure package for large-scale ab initio molecular dynamics". In: *Wiley Interdisciplinary Reviews: Computational Molecular Science* (2020), e1494 (cit. on p. 12).

[49] Loup Verlet. "Computer" experiments" on classical fluids. I. Thermodynamical properties of Lennard-Jones molecules". In: *Physical review* 159.1 (1967), p. 98 (cit. on p. 13).

[50] William C Swope, Hans C Andersen, Peter H Berens, and Kent R Wilson. "A computer simulation method for the calculation of equilibrium constants for the formation of physical clusters of molecules: Application to small water clusters". In: *The Journal of chemical physics* 76.1 (1982), pp. 637–649 (cit. on p. 13).

[51] N Schmid, AP Eichenberger, A Choutko, et al. "Definition and testing of the GROMOS force-field versions 54A7 and 54B7." In: *Biophys. J* 40 (2011), pp. 843–856 (cit. on pp. 13, 36, 84).

[52] William L Jorgensen and Julian Tirado-Rives. "The OPLS [optimized potentials for liquid simulations] potential functions for proteins, energy minimizations for crystals of cyclic peptides and crambin". In: *Journal of the American Chemical Society* 110.6 (1988), pp. 1657–1666 (cit. on pp. 13, 67).

[53] P. P. Ewald. *Die Berechnung optischer und elektrostatischer Gitterpotentiale*. Jan. 1921 (cit. on p. 15).

[54] Abdulnour Y Toukmaji and John A Board Jr. "Ewald summation techniques in perspective: a survey". In: *Computer physics communications* 95.2-3 (1996), pp. 73–92 (cit. on p. 16).

[55] Roger W Hockney and James W Eastwood. *Computer simulation using particles*. crc Press, 1988 (cit. on p. 16).

[56] Brad A Wells and Alan L Chaffee. "Ewald summation for molecular simulations". In: *Journal of chemical theory and computation* 11.8 (2015), pp. 3684–3695 (cit. on p. 16).

[57] EL Pollock and Jim Glosli. "Comments on P3M, FMM, and the Ewald method for large periodic Coulombic systems". In: *Computer Physics Communications* 95.2-3 (1996), pp. 93–110 (cit. on p. 16).

[58] Denis J Evans and Brad Lee Holian. "The nose–hoover thermostat". In: *The Journal of chemical physics* 83.8 (1985), pp. 4069–4074 (cit. on p. 17).

[59]Herman JC Berendsen, JPM van Postma, Wilfred F van Gunsteren, ARHJ DiNola, and Jan R Haak. “Molecular dynamics with coupling to an external bath”. In: *The Journal of chemical physics* 81.8 (1984), pp. 3684–3690 (cit. on p. 17).

[60]Hiqmet Kamberaj. *Molecular Dynamics Simulations in Statistical Physics: Theory and Applications*. Springer, 2020 (cit. on p. 17).

[61]Nicholas Metropolis, Arianna W Rosenbluth, Marshall N Rosenbluth, Augusta H Teller, and Edward Teller. “Equation of state calculations by fast computing machines”. In: *The journal of chemical physics* 21.6 (1953), pp. 1087–1092 (cit. on p. 18).

[62]W Keith Hastings. “Monte Carlo sampling methods using Markov chains and their applications”. In: (1970) (cit. on p. 18).

[63]Dieter Meschede. *Gerthsen Physik*. Vol. 24. Springer, 2010 (cit. on pp. 20, 21, 24).

[64]B Th Thole. “Molecular polarizabilities calculated with a modified dipole interaction”. In: *Chemical Physics* 59.3 (1981), pp. 341–350 (cit. on p. 22).

[65]Jon Applequist, James R Carl, and Kwok-Kueng Fung. “Atom dipole interaction model for molecular polarizability. Application to polyatomic molecules and determination of atom polarizabilities”. In: *Journal of the American Chemical Society* 94.9 (1972), pp. 2952–2960 (cit. on p. 22).

[66]Lasse Jensen, Per-Olof Åstrand, Anders Osted, Jacob Kongsted, and Kurt V Mikkelsen. “Polarizability of molecular clusters as calculated by a dipole interaction model”. In: *The Journal of chemical physics* 116.10 (2002), pp. 4001–4010 (cit. on p. 22).

[67]O Ostroverkhova, DG Cooke, S Shcherbyna, et al. “Bandlike transport in pentacene and functionalized pentacene thin films revealed by subpicosecond transient photoconductivity measurements”. In: *Physical Review B* 71.3 (2005), p. 035204 (cit. on p. 27).

[68]Daniel J Gaspar and Evgueni Polikarpov. *OLED fundamentals: materials, devices, and processing of organic light-emitting diodes*. CRC press, 2015 (cit. on pp. 27, 29–31).

[69]Andre Bernanose, Marcel Comte, and Paul Vouaux. “Sur un nouveau mode d’émission lumineuse chez certains composés organiques”. In: *Journal de Chimie Physique* 50 (1953), pp. 64–68 (cit. on p. 29).

[70]Slawomir Braun, William R Salaneck, and Mats Fahlman. “Energy-level alignment at organic/metal and organic/organic interfaces”. In: *Advanced materials* 21.14-15 (2009), pp. 1450–1472 (cit. on p. 29).

[71] Yongsup Park, V Choong, Yongli Gao, Bing R Hsieh, and Ching Wan Tang. "Work function of indium tin oxide transparent conductor measured by photoelectron spectroscopy". In: *Applied physics letters* 68.19 (1996), pp. 2699–2701 (cit. on p. 29).

[72] Chihaya Adachi, Reiji Hattori, Hironori Kaji, and Tsujimura, eds. *Handbook of Organic Light-Emitting Diodes*. Springer Nature Living ReferenceSpringer eBook Collection. Tokyo: Springer, 2020 (cit. on p. 29).

[73] Wolfgang Brütting. "Introduction to the physics of organic semiconductors". In: *Physics of organic semiconductors* (2005), pp. 1–14 (cit. on p. 29).

[74] Paul-Anton Will and Sebastian Reineke. "21 - Organic light-emitting diodes". In: *Handbook of Organic Materials for Electronic and Photonic Devices (Second Edition)*. Ed. by Oksana Ostroverkhova. Second Edition. Woodhead Publishing Series in Electronic and Optical Materials. Woodhead Publishing, 2019, pp. 695–726 (cit. on p. 30).

[75] Sangyeob Lee, Hyun Koo, Ohyun Kwon, et al. "The role of charge balance and excited state levels on device performance of exciplex-based phosphorescent organic light emitting diodes". In: *Scientific reports* 7.1 (2017), pp. 1–9 (cit. on p. 30).

[76] H Gorter, MJJ Coenen, MWL Slaats, et al. "Toward inkjet printing of small molecule organic light emitting diodes". In: *Thin Solid Films* 532 (2013), pp. 11–15 (cit. on p. 32).

[77] Maki Shibata, Yoshiya Sakai, and Daisuke Yokoyama. "Advantages and disadvantages of vacuum-deposited and spin-coated amorphous organic semiconductor films for organic light-emitting diodes". In: *Journal of Materials Chemistry C* 3.42 (2015), pp. 11178–11191 (cit. on p. 32).

[78] Priyanka Tyagi, Ritu Srivastava, Lalat Indu Giri, Suneet Tuli, and Changhee Lee. "Degradation of organic light emitting diode: Heat related issues and solutions". In: *Synthetic Metals* 216 (2016), pp. 40–50 (cit. on p. 32).

[79] Dan Wang, Cong Cheng, Taiju Tsuboi, and Qisheng Zhang. "Degradation Mechanisms in Blue Organic Light-Emitting Diodes". In: *CCS Chemistry* 2.4 (2020), pp. 1278–1296 (cit. on p. 32).

[80] Masahiro Hiramoto. "ENERGETIC AND NANOSTRUCTURAL DESIGN OF SMALL-MOLECULAR-TYPE ORGANIC SOLAR CELLS". In: *Advances in Chemical Physics, John Wiley & Sons, USA* (2017), pp. 137–204 (cit. on p. 33).

[81] Barry P Rand and Henning Richter. *Organic Solar Cells: fundamentals, devices, and upscaling*. CRC Press, 2014 (cit. on p. 34).

[82] Giulia Casula, Stefano Lai, Laura Matino, et al. "Printed, Low-Voltage, All-Organic Transistors and Complementary Circuits on Paper Substrate". In: *Advanced Electronic Materials* 6.5 (2020), p. 1901027 (cit. on p. 34).

[83]Shakeel S. Dalal, Diane M. Walters, Ivan Lyubimov, Juan J. de Pablo, and M. D. Ediger. “Tunable molecular orientation and elevated thermal stability of vapor-deposited organic semiconductors”. In: *Proceedings of the National Academy of Sciences* 112.14 (Apr. 7, 2015), pp. 4227–4232 (cit. on p. 35).

[84]RW Hockney and JW Eastwood. “The particle-mesh force calculation”. In: *Computer Simulation Using Particles, Adam Hilger, Bristol and New York, NY, USA* (1989), pp. 120–165 (cit. on p. 36).

[85]In-Chul Yeh and Max L Berkowitz. “Ewald summation for systems with slab geometry”. In: *The Journal of chemical physics* 111.7 (1999), pp. 3155–3162 (cit. on p. 36).

[86]Steve Plimpton. “Fast parallel algorithms for short-range molecular dynamics”. In: *Journal of computational physics* 117.1 (1995), pp. 1–19 (cit. on pp. 36, 67).

[87]Nathan Schmid, Andreas P Eichenberger, Alexandra Choutko, et al. “Definition and testing of the GROMOS force-field versions 54A7 and 54B7”. In: *European biophysics journal* 40.7 (2011), pp. 843–856 (cit. on p. 36).

[88]W. F. Van Gunsteren and H. J. C. Berendsen. “Groningen molecular simulation (GROMOS) library manual, Biomos BV, Nijenborgh 16, 9747”. In: *AG Groningen, The Netherlands* (1987) (cit. on p. 36).

[89]Wei Huang, Zhixiong Lin, and Wilfred F. van Gunsteren. “Validation of the GROMOS 54A7 force field with respect to β-peptide folding”. In: *Journal of chemical theory and computation* 7.5 (2011). Publisher: ACS Publications, pp. 1237–1243 (cit. on p. 36).

[90]Alpeshkumar K Malde, Le Zuo, Matthew Breeze, et al. “An automated force field topology builder (ATB) and repository: version 1.0”. In: *Journal of chemical theory and computation* 7.12 (2011), pp. 4026–4037 (cit. on p. 36).

[91]Martin Stroet, Bertrand Caron, Koen M Visscher, et al. “Automated topology builder version 3.0: prediction of solvation free enthalpies in water and hexane”. In: *Journal of chemical theory and computation* 14.11 (2018), pp. 5834–5845 (cit. on p. 36).

[92]Jean-Paul Ryckaert, Giovanni Ciccotti, and Herman JC Berendsen. “Numerical integration of the cartesian equations of motion of a system with constraints: molecular dynamics of n-alkanes”. In: *Journal of computational physics* 23.3 (1977), pp. 327–341 (cit. on p. 39).

[93]H Späth. “Orthogonal least squares fitting with linear manifolds”. In: *Numerische Mathematik* 48.4 (1986), pp. 441–445 (cit. on p. 45).

[94]Walter Gander and Jiri Hrebicek. *Solving problems in scientific computing using Maple and Matlab®*. Springer Science & Business Media, 2011 (cit. on p. 45).

[95] Amin Salehi, Xiangyu Fu, Dong-Hun Shin, and Franky So. “Recent advances in OLED optical design”. In: *Advanced Functional Materials* 29.15 (2019), p. 1808803 (cit. on p. 46).

[96] Daisuke Yokoyama. “Molecular orientation in small-molecule organic light-emitting diodes”. In: *Journal of Materials Chemistry* 21.48 (2011), pp. 19187–19202 (cit. on p. 46).

[97] Kaoru Urano and Masayoshi Inoue. “Clausius–Mossotti formula for anisotropic dielectrics”. In: *The Journal of Chemical Physics* 66.2 (1977), pp. 791–794 (cit. on p. 46).

[98] Eisuke Ito, Yuuki Washizu, Naoki Hayashi, et al. “Spontaneous buildup of giant surface potential by vacuum deposition of Alq 3 and its removal by visible light irradiation”. In: *Journal of applied physics* 92.12 (2002), pp. 7306–7310 (cit. on p. 46).

[99] Lars Jäger, Tobias D Schmidt, and Wolfgang Brütting. “Manipulation and control of the interfacial polarization in organic light-emitting diodes by dipolar doping”. In: *AIP Advances* 6.9 (2016), p. 095220 (cit. on p. 47).

[100] Pascal Friederich, Vadim Rodin, Florian Von Wrochem, and Wolfgang Wenzel. “Built-in potentials induced by molecular order in amorphous organic thin films”. In: *ACS applied materials & interfaces* 10.2 (2018), pp. 1881–1887 (cit. on p. 47).

[101] U Chandra Singh and Peter A Kollman. “An approach to computing electrostatic charges for molecules”. In: *Journal of computational chemistry* 5.2 (1984), pp. 129–145 (cit. on pp. 49, 67, 84).

[102] Rudolph A Marcus. “On the theory of oxidation-reduction reactions involving electron transfer. I”. In: *The Journal of chemical physics* 24.5 (1956), pp. 966–978 (cit. on p. 49).

[103] Rudolph A Marcus. “Electrostatic free energy and other properties of states having nonequilibrium polarization. I”. In: *The journal of chemical physics* 24.5 (1956), pp. 979–989 (cit. on p. 49).

[104] V Stehr, J Pfister, RF Fink, B Engels, and C Deibel. “First-principles calculations of anisotropic charge-carrier mobilities in organic semiconductor crystals”. In: *Physical Review B* 83.15 (2011), p. 155208 (cit. on pp. 49, 50).

[105] Hong Li, Jean-Luc Brédas, and Christian Lennartz. “First-principles theoretical investigation of the electronic couplings in single crystals of phenanthroline-based organic semiconductors”. In: *The Journal of chemical physics* 126.16 (2007), p. 164704 (cit. on p. 50).

[106] Amin Salehi, Ying Chen, Xiangyu Fu, Cheng Peng, and Franky So. “Manipulating refractive index in organic light-emitting diodes”. In: *ACS applied materials & interfaces* 10.11 (2018), pp. 9595–9601 (cit. on pp. 51, 59, 61).

[107]Carl Degitz, Manuel Konrad, Simon Kaiser, and Wolfgang Wenzel. “Simulating the growth of amorphous organic thin films”. In: *Organic Electronics* (2022), p. 106439 (cit. on pp. 51, 55, 57, 58, 64).

[108]Florian Weigend and Reinhart Ahlrichs. “Balanced basis sets of split valence, triple zeta valence and quadruple zeta valence quality for H to Rn: Design and assessment of accuracy”. In: *Physical Chemistry Chemical Physics* 7.18 (2005), pp. 3297–3305 (cit. on pp. 62, 67, 84).

[109]Franz Symalla, Pascal Friederich, Andrea Massé, et al. “Charge transport by superexchange in molecular host-guest systems”. In: *Physical review letters* 117.27 (2016), p. 276803 (cit. on pp. 63, 64).

[110]Shun-Wei Liu, Chih-Chien Lee, Chi-Feng Lin, et al. “4-Hydroxy-8-methyl-1, 5-naphthyridine aluminium chelate: a morphologically stable and efficient exciton-blocking material for organic photovoltaics with prolonged lifetime”. In: *Journal of Materials Chemistry* 20.36 (2010), pp. 7800–7806 (cit. on p. 64).

[111]Shigeki Naka, Hiroyuki Okada, Hiroyoshi Onnagawa, and Tetsuo Tsutsui. “High electron mobility in bathophenanthroline”. In: *Applied Physics Letters* 76.2 (2000), pp. 197–199 (cit. on p. 64).

[112]Heume-Il Baek, Changhee Lee, and Byung Doo Chin. “Comparison of the carrier mobility, unipolar conduction, and light emitting characteristics of phosphorescent host–dopant system”. In: *Synthetic Metals* 162.24 (2012), pp. 2355–2360 (cit. on p. 64).

[113]Shigeki Naka, Hiroyuki Okada, Hiroyoshi Onnagawa, Yoshihisa Yamaguchi, and Tetsuo Tsutsui. “Carrier transport properties of organic materials for EL device operation”. In: *Synthetic metals* 111 (2000), pp. 331–333 (cit. on p. 64).

[114]Vadim Rodin, Franz Symalla, Velimir Meded, et al. “Generalized effective-medium model for the carrier mobility in amorphous organic semiconductors”. In: *Physical Review B* 91.15 (2015), p. 155203 (cit. on p. 63).

[115]Markus Schmid, Kristoffer Harms, Carl Degitz, et al. “Optical and Electrical Measurements Reveal the Orientation Mechanism of Homoleptic Iridium-Carbene Complexes”. In: *ACS Applied Materials & Interfaces* 12.46 (2020). PMID: 33164497, pp. 51709–51718. eprint: `https://doi.org/10.1021/acsami.0c14613` (cit. on pp. 65, 68, 71, 73, 75, 77).

[116]William Humphrey, Andrew Dalke, and Klaus Schulten. “VMD – Visual Molecular Dynamics”. In: *Journal of Molecular Graphics* 14 (1996), pp. 33–38 (cit. on p. 65).

[117] Andrew I Jewett, David Stelter, Jason Lambert, et al. “Moltemplate: A Tool for Coarse-Grained Modeling of Complex Biological Matter and Soft Condensed Matter Physics”. In: *Journal of molecular biology* 433.11 (2021), p. 166841 (cit. on p. 67).

[118] *TURBOMOLE V7.2 2017, a development of University of Karlsruhe and Forschungszentrum Karlsruhe GmbH, 1989-2007, TURBOMOLE GmbH, since 2007* (cit. on pp. 67, 70, 76).

[119] H Kamberaj, RJ Low, and MP Neal. “Time reversible and symplectic integrators for molecular dynamics simulations of rigid molecules”. In: *The Journal of chemical physics* 122.22 (2005), p. 224114 (cit. on p. 67).

[120] Anthony K Rappé, Carla J Casewit, KS Colwell, William A Goddard III, and W Mason Skiff. “UFF, a full periodic table force field for molecular mechanics and molecular dynamics simulations”. In: *Journal of the American chemical society* 114.25 (1992), pp. 10024–10035 (cit. on p. 67).

[121] Farah Salameh, Andrea Al Haddad, Antoine Picot, et al. “Modeling the luminance degradation of OLEDs using Design of Experiments”. In: *IEEE Transactions on Industry Applications* 55.6 (2019), pp. 6548–6558 (cit. on p. 69).

[122] Pascal Friederich, Reinder Coehoorn, and Wolfgang Wenzel. “Molecular origin of the anisotropic dye orientation in emissive layers of organic light emitting diodes”. In: *Chemistry of Materials* 29.21 (2017), pp. 9528–9535 (cit. on p. 69).

[123] D Andrae, U Haeussermann, M Dolg, H Stoll, and H Preuss. “Energy-adjusted ab initio pseudopotentials for the second and third row transition elements”. In: *Theoretica chimica acta* 77.2 (1990), pp. 123–141 (cit. on p. 70).

[124] J Stephen Binkley, John A Pople, and Warren J Hehre. “Self-consistent molecular orbital methods. 21. Small split-valence basis sets for first-row elements”. In: *Journal of the American Chemical Society* 102.3 (1980), pp. 939–947 (cit. on p. 70).

[125] Shiro Koseki, Michael W Schmidt, and Mark S Gordon. “MCSCF/6-31G (d, p) calculations of one-electron spin-orbit coupling constants in diatomic molecules”. In: *The Journal of physical chemistry* 96.26 (1992), pp. 10768–10772 (cit. on p. 70).

[126] Shiro Koseki, Mark S Gordon, Michael W Schmidt, and Nikita Matsunaga. “Main group effective nuclear charges for spin-orbit calculations”. In: *The Journal of Physical Chemistry* 99.34 (1995), pp. 12764–12772 (cit. on p. 70).

[127] Shiro Koseki, Michael W Schmidt, and Mark S Gordon. “Effective nuclear charges for the first-through third-row transition metal elements in spin-orbit calculations”. In: *The Journal of Physical Chemistry A* 102.50 (1998), pp. 10430–10435 (cit. on p. 70).

[128]Kęstutis Aidas, Celestino Angeli, Keld L. Bak, et al. “The Dalton quantum chemistry program system”. In: *WIREs Comput. Mol. Sci.* 4.3 (2014), pp. 269–284 (cit. on p. 70).

[129]K Mori, TPM Goumans, E Van Lenthe, and F Wang. “Predicting phosphorescent lifetimes and zero-field splitting of organometallic complexes with time-dependent density functional theory including spin–orbit coupling”. In: *Physical Chemistry Chemical Physics* 16.28 (2014), pp. 14523–14530 (cit. on p. 71).

[130]Pascal Friederich, Manuel Konrad, Timo Strunk, and Wolfgang Wenzel. “Machine learning of correlated dihedral potentials for atomistic molecular force fields”. In: *Scientific reports* 8.1 (2018), pp. 1–8 (cit. on pp. 83, 84, 91, 95).

[131]Diederik P Kingma and Jimmy Ba. “Adam: A method for stochastic optimization”. In: *arXiv preprint arXiv:1412.6980* (2014) (cit. on p. 89).

[132]Matteo Ricci, Otello Maria Roscioni, Lara Querciagrossa, and Claudio Zannoni. “MOLC. A reversible coarse grained approach using anisotropic beads for the modelling of organic functional materials”. In: *Physical Chemistry Chemical Physics* 21.47 (2019), pp. 26195–26211 (cit. on p. 96).

List of Publications

B

Articles

- Markus Schmid, Kristoffer Harms, Carl Degitz, Thomas Morgenstern, Alexander Hofmann, Pascal Friederich, Hans-Hermann Johannes, Wolfgang Wenzel, Wolfgang Kowalsky, Wolfgang Brütting
  Optical and electrical measurements reveal the orientation mechanism of homoleptic iridium-carbene complexes
  ACS applied materials & interfaces, 2020, 12 (46), 51709-51718

- Marius Jakoby, Shahriar Heidrich, Lorenz Graf von Reventlow, Carl Degitz, Subeesh Madayanad Suresh, Eli Zysman-Colman, Wolfgang Wenzel, Bryce S Richards, Ian A Howard
  Method for accurate experimental determination of singlet and triplet exciton diffusion between thermally activated delayed fluorescence molecules
  Chemical Science, 2021, 12 (3), 1121-1125

- Montserrat Penaloza-Amion, Elaheh Sedghamiz, Mariana Kozlowska, Carl Degitz, Clemens Possel, Wolfgang Wenzel
  Monte-Carlo Simulations of Soft Matter using SIMONA: A review of recent applications
  Frontiers in Physics, 2021, 9, 83

- Carl Degitz, Manuel Konrad, Simon Kaiser, Wolfgang Wenzel
  Simulating the growth of amorphous organic thin films
  Organic Electronics, 2022, 106439

- Carl Degitz, Markus Schmid, Falk May, Charlotte Walter, Wolfgang Brütting, Wolfgang Wenzel
  From molecule to device: Prediction and validation of the optical orientation of Iridium phosphors in OLEDs
  Submitted

Danksagung

Mein erster Dank gilt Prof. Wolfgang Wenzel, welcher bereits meine Masterarbeit betreute und nun auch die Betreung dieser Dissertation übernahm. Danke, Wolfgang, dass du mir die Gelegenheit und das Vertrauen gegeben hast, diese Promotion in Zusammenarbeit mit Merck durchzuführen. Außerdem danke ich Prof. Jörg Schmalian für die Übernahme der Rolle des Korreferentens.

Ich danke weiterhin allen meinen Kolleg*innen bei der Merck KGaA in Darmstadt für ein stets freundliches und angenehmes Arbeitsklima. Im Speziellen gilt mein Dank dort Dr. Christof Pflumm und Dr. Falk May für die tolle Betreuung während meiner Zeit bei Merck.

Weiterer Dank gilt meinen zwei Bürokollegen Manuel Konrad und Simon Kaiser für eine tolle Zeit mit unvergesslichen Comics, tollen Tagen in Paris und stets pünktlichen Kaffeepausen. Desweiteren danke ich allen jetzigen und ehemaligen Kolleg*innen aus der AG Wenzel, im Speziellen: Manuel Rommel, Pascal Friederich, Timo Strunk, Tobias Neumann, Franz Symalla, Velimir Meded, Modan Liu, Jorge Olivares Pena, Shahriar Heidrich, Tobias Schlöder, Montserrat Penaloza-Amion, Jörg Schaarschmidt, Yohanes Pramudya, Mariana Kozlowska, Artem Fediai, Deniz Özdemir and Praneeth Chilakalapudi.

Ein großes Dankeschön gilt weiterhin allen Freunden und Bekannten, welche mich in den letzten Jahren begleitet haben.

Mein letzter und größter Dank gilt meinen Eltern und meiner Schwester, ohne deren stetige und bedingungslose Unterstützung der Abschluss dieser Arbeit nicht möglich gewesen wäre.